8-2011

Structural Identification and Damage Identification using Output-Only Vibration Measurements

Shutao Xing
Utah State University

STRUCTURAL IDENTIFICATION AND DAMAGE IDENTIFICATION USING OUTPUT-ONLY VIBRATION MEASUREMENTS

by

Shutao Xing

A dissertation submitted in partial fulfillment
of the requirements for the degree

of

DOCTOR OF PHILOSOPHY

in

Civil Engineering

Approved:

_____	_____
Dr. Marvin W. Halling Major Professor	Dr. James A. Bay Committee Member
_____	_____
Dr. Paul J. Barr Committee Member	Dr. Wenbin Yu Committee Member
_____	_____
Dr. Kevin C. Womack Committee Member	Dr. Mark R. McLellan Vice President for Research and Dean of the School of Graduate Studies

UTAH STATE UNIVERSITY
Logan, Utah

2011

ABSTRACT

This dissertation studied the structural identification and damage detection of civil engineering structures. Several issues regarding structural health monitoring were addressed.

The data-driven subspace identification algorithm was investigated for modal identification of bridges using output-only data. This algorithm was tested through a numerical truss bridge with abrupt damage as well as a real concrete highway bridge with actual measurements. Stabilization diagrams were used to analyze the identified results and determine the modal characteristics. The identification results showed that this identification method is quite effective and accurate.

The influence of temperature fluctuation on the frequencies of a highway concrete bridge was investigated using ambient vibration data over a one-year period of a highway bridge under health monitoring. The data were fitted by nonlinear and linear regression models, which were then analyzed.

The substructure identification by using an adaptive Kalman filter was investigated by applying numerical studies of a shear building, a frame structure, and a truss structure. The stiffness and damping were identified successfully from limited acceleration responses, while the abrupt damages were identified as well. Wavelet analysis was also proposed for damage detection of substructures, and was shown to be able to approximately locate such damages.

Delamination detection of concrete slabs by modal identification from the output-only data was proposed and carried out through numerical studies and experimental modal testing. It was concluded that the changes in modal characteristics can indicate the

presence and severity of delamination. Finite element models of concrete decks with different delamination sizes and locations were established and proven to be reasonable.

Pounding identification can provide useful early warning information regarding the potential damage of structures. This thesis proposed to use wavelet scalograms of dynamic response to identify the occurrence of pounding. Its applications in a numerical example as well as shaking table tests of a bridge showed that the scalograms can detect the occurrence of pounding very well.

These studies are very useful for vibration-based structural health monitoring.

(213 pages)

PUBLIC ABSTRACT

This dissertation addressed damage detection of civil engineering structure, such as, buildings and bridges, by using the measurements of vibration sensors that were instrumented on these structures. The damage detection and health monitoring of the infrastructures are essential to keep them working safely, thus to avoid loss of lives and wealth due to the disastrous damage. Several issues regarding the damage detection of civil engineering structures were addressed as follows.

A subspace-based method successfully obtained damage information of a truss bridge from simulated measurements as well as of a highway concrete girder bridge from actual vibration measurements. This method is recommended to be one choice of the methods to process vibration data.

The influence of temperature fluctuation on the natural frequencies of a highway concrete bridge was investigated using vibration data over a one-year period of a highway bridge under health monitoring. The data were analyzed through statistical method and the relationship between natural frequencies and temperatures were correlated. These correlations are useful for discriminating damage from normal changes.

In reality, it is not possible to install sufficient sensors on the structures and it is also difficult to analyze for a large system due to numerical difficulty. A substructural approach with a filtering algorithm was used to address this issue and examined by their applications. It was proved to be quite effective and can obtain damage information accurately.

Delamination is of great concern for bridges and routine inspection is necessary. This dissertation proposed to detect delamination of concrete plates by modal

identification using measurements of vibration sensors. This new approach can reduce the costs significantly and could obtain real-time delamination information.

When subjected to earthquake, the pounding can occur between different structures, for example, the adjacent buildings, or the different parts of a structure, for example, two spans of a bridge, and can cause considerable damage or degradation to the structures. Therefore, the monitoring of the pounding is useful and can provide useful early warning. This dissertation proposed and investigated a wavelet-based approach to detect the occurrence of pounding through simulated as well as large shake table tests to a bridge model. The approach was proved to be effective.

These studies are very useful for the health monitoring and safe operation of bridges, buildings, and other engineering structures.

ACKNOWLEDGMENTS

First and foremost, I wish to sincerely express my gratitude to my major professor, Dr. Marvin W. Halling, for his continuous support and guidance. I would like to thank all the committee members listed in the title page and former member for their suggestions and help. I also want to thank Dr. Xun Guo and Dr. Qingli Meng (Institute of Engineering Mechanics, China Earthquake Administration) for their cooperation and help. I appreciate the valuable comments and assistances given by the researchers, teachers, and friends during the research portion of my thesis, there is a long list of those for whom I am grateful. I want to thank Dr. James Bay for his help on experiments and advices on dissertation. I also want to thank David Marchant for his assistance on maintenance of the real-time bridge health monitoring system, and wish to thank the staff and graduate students at USU who have provided assistance and help. Last, but not least, I want to express my deep appreciation to my parents, brother and other family members for their unwavering support and love.

Shutao Xing

CONTENTS

Page

LIST OF TABLES

LIST OF FIGURES

CHAPTER I

INTRODUCTION

This chapter gives a general introduction on vibration-based structural health monitoring, which is the subject of this thesis. The structural identification and damage identification methods are discussed. The research topics and organization of this thesis are demonstrated.

1. Structural Health Monitoring Based on Vibration Measurements

Structural health monitoring (SHM) is the process to implement a damage identification system for civil, mechanical, and aerospace engineering structures, which can reliably monitor the health and performance of the structures. SHM can be classified as local or global [1]. Local methods detect damages of the structural components using non-destructive examination methods, such as, acoustics, eddy current, emission spectroscopy, magnetic methods, radiography, ultrasonic, X-ray, and visual inspection.

Global methods are used to detect damage to the entire structure. Much research has been conducted on global methods based on the sensor system and vibration analysis. The vibration-based damage detection has been the routine method for mechanical and aerospace engineering structures. With the upgrading of instrumentation and better understanding of the dynamics of civil structures, the vibration-based SHM has received increased attention and has gone through rapid development in the past two decades. Doebling et al. [2-3] did a comprehensive technical literature review of vibration-based damage identification of structures. Sohn et al. [4] updated the literature review [2-3] with more recent advancement. Chang et al. [5] presented a review of research work on

health monitoring of civil infrastructures.

Among civil structures, the bridge is one of the most important infrastructures. In the U.S.A., around 50% of bridges were built before the 1940's and the Federal highway administration (FHWA) [6] stated that 24% bridges were structurally deficient in 2010, making it necessary to monitor their health for public safety and property protection. Long-term structural health monitoring systems for large-scale bridges has been implemented successfully worldwide; a list of them can be found in [7]. The long-term bridge performance assessment of representative highway bridges has been initiated by FHWA.

It is expected that the SHM systems can provide useful information to determine the damage extent of structures. As described by Rytter [8], damage identification can be characterized at four levels: 1. determining if the structure has any damage, 2. deciding the location of the damages, 3. quantifying the degree of the damage, 4. predicting the remaining service life of the structure.

This thesis contains research work related to Levels 1-3, that is damage detection in Level 1 and the inverse problems typically found in Levels 2 and 3 are studied in this dissertation. Belonging to the fields of fracture mechanics and structural design evaluation, level 4 is not included in this study.

2. System Identification and Damage Identification Methods

The SHM system generates copious amounts of data; therefore, how to process these data and interpret the results becomes an important and challenging problem. The system identification algorithms are used to process the data while the vibration theories

are used to extract features of the structures.

System identification is the process of building and improving mathematical models of a dynamic system from experimental data which can be input-output data or output only data. The general theories and applied techniques can be found in [9-10]. The system identification in structures can be called structural identification. The basic routes for vibration analysis and structural identification are shown in Figure 1 and Figure 2.

Many system identification algorithms are available, such as, the least-square estimation (LSE), the extended Kalman filter (EKF), the subspace identification, the natural excitation technique combined with the eigensystem realization algorithm (NExT-ERA), the neural networks, the genetic, and the wavelet based methods. All these methods have been used in system identification and damage identification of many types of civil engineering structures.

The application of system identification to vibrating objects is called modal analysis or experimental modal analysis. The experimental testing is referred to as modal testing in Ewins [11]. Modal analysis has two stages: 1) to choose the appropriate type of model and 2) to figure the appropriate parameters of the chosen model. Generally there are three models/phases in the typical progress of vibration analysis, which include the following: a) a description of the structure's physical characteristics, in terms of mass, stiffness and damping properties, which is referred to as the spatial model; b) description of the structure's behavior by modal frequencies, modal damping, and mode shapes of a set of vibration modes, which is referred to as the modal model; c) description of the structure's response under given excitation, which is referred to as the response model. These models are used extensively in modal testing and analysis.

The modal analysis from the measurements of modal testing can be used for updating the numerical (finite element) model. This is referred to as finite element model updating in Friswell and Mottershead [12]. The finite element model updating has been studied extensively in much of the literature.

To briefly summarize, in order to get correct judgment of the structure's health status or structural integrity from the SHM systems, it is essential to have an understanding of damage identification algorithms and vibration theories, as well as to gain insight into its structural behavior.

3. Focus of the Research

This thesis focuses on the identification of damage to structures using output-only data. The stochastic subspace identification, frequency domain decomposition, traditional peak-picking, extended Kalman filter, and wavelet transform methods were used in this study. Numerical studies involving finite element modeling, and experimental studies including experimental modal testing, real-time monitoring measurements, and shake table tests, were carried out. The main contributions are specified as follows.

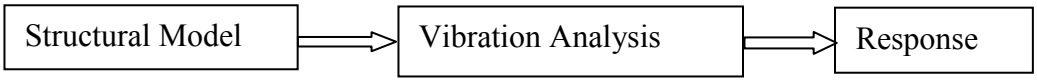

Figure 1. Vibration analysis

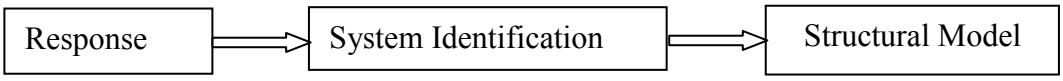

Figure 2. Structural identification

Data-driven stochastic subspace algorithms were applied in modal identification of a numerical bridge with abrupt damage and a real highway bridge from their acceleration responses. The stabilization diagrams combined with the subspace identification algorithms were used to keep physical modes and eliminate spurious modes. A subspace identification algorithm N4SID was also examined through its application to modal identification of the highway bridge.

The adaptive Kalman filter was proposed for use in identifying spatial models of substructures with abrupt damage. This use is to solve an inverse problem by identifying and tracking the stiffness and damping through the substructural approach. This approach was investigated by numerical studies on three types of structures. Wavelet transform was also proposed to be used for substructural damage identification and was examined more closely in later sections.

This thesis proposes to detect the delamination of concrete structures by modal identification from output-only vibration measurements. The method was investigated through numerical as well as experimental studies. Finite element models for the experimental models with various delamination scenarios were developed and validated. Some parameters of the finite element model (the contact model) were manually updated to match the modal characteristics from the experimental testing.

Statistical analysis was used to correlate the frequencies and temperature based on one-year monitoring data by nonlinear as well as linear curve fitting.

Identification of the occurrence of pounding was suggested and the wavelet scalogram was proposed to fulfill this objective. This method was examined through a numerical model and the experimental data from shake table tests.

4. Organization of the Main Text

This dissertation has been made up of multiple papers. Chapters II-V cover one or two topics and are self-contained, consisting of the abstract, introduction, main contents, and the conclusion. All of these topics focus on vibration-based system identification and damage detection. Chapters II, III, and V mainly investigate the applicability and effectiveness of the structural identification algorithms. The goal of chapter IV is to solve practical problems by using the vibration-based method from the response measurements by sensors in the structures that are under normal operation. The chapter-by-chapter overview is given as follows:

Chapter I introduces the research background and the issues to be addressed. It provides the organization of the main topics and provides context for this thesis.

Chapter II investigates the effectiveness of stochastic subspace identification algorithms and stabilization diagrams in the modal identification of bridges using output-only data. The simulated accelerations from a numerical truss bridge and recorded accelerations from a real concrete bridge are explored as the output data. It also deals with the relationship between temperature and frequencies based on one-year monitoring data of a highway bridge.

Chapter III identifies damage in substructures with the extended Kalman filter from the measurements in the substructures only. This method was investigated by numerical studies of shear building, frame, and truss structures. The stiffness and damping were clearly identified. This chapter also used wavelet transform to detect damages that were presented in substructures.

Chapter IV presents the delamination detection of concrete structures by modal

identification from output-only data, which are, acceleration or velocity measurements. The applicability was first studied through simulations by finite element modeling. Then the experimental studies were carried out to test the proposed method of delamination detection and useful results were found.

Chapter V proposes to detect the occurrence of structural pounding by using wavelet scalograms of acceleration responses. The methods were examined by their applications in a numerical example as well as in shake table tests of a scale model of a steel bridge subjected to earthquake ground motion.

Chapter VI integrates the conclusions of the main work. Additionally, it gives suggestions for further studies.

REFERENCES

[1] G. Housner, L. Bergman, T. Caughey, A. Chassiakos, R. Claus, S. Masri, R. Skelton, T. Soong, B. Spencer, J. Yao, Structural control: past, present, and future, ASCE Journal of Engineering Mechanics 123 (1997) 897-971.

[2] S.W. Doebling, C.R. Farrar, M.B. Prime, D.W. Shevitz, Damage identification and health monitoring of structural and mechanical systems from changes in their vibration characteristics: a literature review, Los Alamos National Laboratory Report LA-13070-MS, NM, 1996.

[3] S.W. Doebling, C.R. Farrar, M.B. Prime, A summary review of vibration-based damage identification methods, Shock and Vibration Digest 30 (1998) 91-105.

[4] H. Sohn, C. Farrar, F. Hemez, D. Shunk, D. Stinemates, B. Nadler, J.J. Czarnecki, A review of structural health monitoring literature: 1996-2001, Los Alamos National

Laboratory Report No. LA-13976-MS, Los Alamos, NM, 2004.

[5] P.C. Chang, A. Flatau, S.C. Liu, Review paper: health monitoring of civil infrastructure, Structural Health Monitoring 2 (2003) 257-267.

[6] FHWA, FHWA Bridge Programs NBI Data: Deficient Bridges by State and Highway System, 2010.

[7] J.M. Ko, Y.Q. Ni, Technology developments in structural health monitoring of large-scale bridges, Engineering Structures 27 (2005) 1715-1725.

[8] A. Rytter, Vibration based inspection of civil engineering structures, Department of Buidling Technology and Structural Engineering, Aalborg University, Denmark, 1993.

[9] L. Ljung, System Identification: Theory for the User, second ed., Prentice Hall PTR, Upper Saddle River, New Jersey, 1999.

[10] J.-N. Juang, Applied System Identification, PTR Prentice-Hall, Englewood Cliffts, NJ, 1994.

[11] D.J. Ewins, Modal Testing: Theory, Practice and Application, second ed., Research Studies Press LTD., Baldock, Hertfordshire, England, 2000.

[12] M.I. Friswell, J.E. Mottershead, Finite Element Model Updating in Structural Dynamics, Kluwer Academic Publishers, Dordrecht, the Netherlands, 1995.

CHAPTER II

APPLICATION OF STOCHASTIC SUBSPACE IDENTIFICATION IN BRIDGE HEALTH MONITORING, AND STATISTICAL ANALYSIS OF INFLUENCES OF TEMPERATURE FLUCTUATIONS ON FREQUENCIES

ABSTRACT

Forced vibration tests of civil engineering structures is not economical, and in many cases impractical or even impossible. As an alternative, ambient vibration tests and real-time monitoring have become more accepted. Both time and frequency domain system identification algorithms can be used for these output-only systems. This study used the data-driven subspace identification algorithms, which directly use the output time histories and don't need to compute the covariances. The purpose was to investigate the effectiveness and applicability of this type of algorithm in modal analysis of bridges by using output-only measurements.

The stochastic subspace identification (SSI) algorithm was examined through a numerical truss bridge as well as a real concrete girder bridge. In the modal identifications, the simulated dynamic responses of the truss bridge with abrupt damages during the excitation and the actual acceleration measurements by the real-time health monitoring system were used as the output data for the numerical truss bridge and the real highway bridge respectively. Stabilization diagrams with a range of model orders were used to determine the modal frequencies, damping ratios, and mode shapes.

As one of the environmental conditions, temperature fluctuations can have a great effect on the dynamic characteristics of a bridge. It is useful to learn the pattern of changes in frequencies due to temperature fluctuations. The variation of frequencies with

respect to temperature was investigated using one-year ambient vibration data of a highway bridge. The data were sufficient for statistical analysis with a large range of temperatures. The modal frequencies and temperatures were correlated, which shows that such correlations for most modes can be represented by single or bilinear lines, which are summarized later in the document.

1. Introduction

For structural health monitoring, the system identification methods are vital as well as challenging and are still in the development stage. Both frequency-domain and time-domain methods are used in this dissertation. Frequency-domain methods use either frequency response functions (FRFs) or output spectra as primary data. Time-domain methods use the input/output data directly or indirectly. Some time-domain methods use impulse response functions (IRFs) or directly input and output time histories as primary data. Output-only time-domain methods use output covariances or directly output time histories as primary data [1].

Brincker et al. [2] introduced the frequency domain decomposition method (FDD), which is user friendly as simple peak-picking method but is also capable of identifying even the closed modes using strong noise contaminated signals. This method has been used frequently as shown in literature, as we will see as we examine case studies in later sections.

Among time-domain methods, the subspace based identification method originally proposed in [3] has emerged and gained much attention over the past twenty years where, it has been applied effectively for various types of civil and mechanical structures. These algorithms are based on the concepts of system theory, linear algebra,

and statistics. The subspace methods can obtain linear models from column and row spaces of the matrices calculated from the input-output data. Normally, the column and row spaces contain the model information and Kalman filter (state sequence) information [4]. Subspace identification can be used to compute state space models for either deterministic system from input-output data or stochastic system from output only data. The deterministic and stochastic subspace identification can be treated as special cases and unified as a combined deterministic-stochastic identification to compute state space models from given input-output data. For the theorems and derivations of these algorithms, refer to Van Overschee and De Moor [4]. In this study, stochastic subspace identification (SSI) is used and investigated.

Peeters and Ventura [1] reviewed the benchmark work on evaluating the dynamic characteristics of a three-span reinforced concrete bridge in Switzerland, the Z240 bridge from forced, free and ambient vibration tests data. Both time and frequency domain modal analysis techniques were applied and compared. The frequency domain methods used were the peak-picking, the complex mode indication function and rational fraction polynomial. The time domain methods used were two-stage least squares, Ibrahim time-domain, IRF-driven/covariance-driven subspace identification, and data-driven stochastic identification methods. It concluded that the subspace methods applied to all data sets produced the most complete and consistent modal parameter estimations.

The advantages of the subspace based identification algorithms are that the user has simple and few design variables, and that the methods are numerically robust and computationally simple [5]. Van Overschee and De Moor [6] derived two N4SID algorithms for identifying mixed deterministic-stochastic systems. These algorithms

determine state sequences using the projection of input and output data. These state sequences were outputs of non-steady state Kalman filter banks. Therefore it was easy to determine the state space system matrices. The authors found that because N4SID only use QR decomposition and singular value decomposition (SVD), they were convergent and numerically stable. Abdelghani et al. [7] compared three of the following subspace identification methods: the eigensystem realization algorithm with observer/Kalman filter Markov parameters (ERA/OM), the numerical algorithms for subspace state space system identification (N4SID) that has been implemented in MATLAB, and a refined multiple-output error state space (MOESP) family of algorithms and concluded that N4SID/MOESP obtained better results than ERA/OM.

This study examined the applicability and effectiveness of stochastic subspace identification in modal identification of a numerical truss bridge, and a real bridge in section 3. The simulated acceleration response and actual acceleration measurements were used as output-only data for the identification of numerical model truss bridge and the real bridge respectively. The SSI identified frequencies of the real bridge from the measurements were compared with those by FDD algorithm. The effectiveness of the N4SID was investigated as a specific subspace algorithm in obtaining modal characteristics for the bridge under health monitoring.

This chapter also studies the environmental effects on the modal parameters based on one-year monitoring data of a highway bridge. The background and results are discussed in section 4. This section may be a stand-alone paper after further extensive work.

2. Introduction of Subspace Based Identification

This section briefly summarizes the computational steps of using SSI algorithm to extract the modal characteristics of structures.

2.1 State-space models of the vibrating structures

The equation of motion of the structure can be written as

$$M\ddot{U}(t)+C_2\dot{U}(t)+KU(t)=F(U,t)=\eta u(t) \tag{1}$$

where M, C_2, $K \in \mathbb{R}^{n_1 \times n_1}$ are the mass, damping, and stiffness matrices respectively, $U(t) \in \mathbb{R}^{n_1 \times 1}$ is the displacement vector at time t, the superscript dot denotes the derivative with respect to time, $F(U,t) \in \mathbb{R}^{n_1 \times 1}$ is the external force applied at time t, which can be expressed as a multiplication of an influence matrix $\eta \in \mathbb{R}^{n_1 \times m}$ and a vector $u(t) \in \mathbb{R}^{m \times 1}$ denoting the time series of input data.

The state-space equations are a set of algebraic equations that describe the linear system internally [8]. They originate from control theory, and are also used in structural identification of civil/mechanical structures. Most of the state-space equations in this chapter are classical and extensive descriptions of them can be found in [9].

The Eq. (1) can be written as

$$\begin{bmatrix}\dot{U}(t)\\ \ddot{U}(t)\end{bmatrix}=\begin{bmatrix}0_{n_1,n_1} & I_{n_1}\\ -M^{-1}K & -M^{-1}C_2\end{bmatrix}\begin{bmatrix}U(t)\\ \dot{U}(t)\end{bmatrix}+\begin{bmatrix}0_{n_1,n_1}\\ M^{-1}\eta\end{bmatrix}u(t) \tag{2}$$

let

$$x(t)=\begin{bmatrix}U(t)\\ \dot{U}(t)\end{bmatrix},\ A_c=\begin{bmatrix}0_{n_1,n_1} & I_{n_1}\\ -M^{-1}K & -M^{-1}C_2\end{bmatrix},\ B_c=\begin{bmatrix}0_{n_1,n_1}\\ M^{-1}\eta\end{bmatrix} \tag{3}$$

where $x(t) \in \mathbb{R}^{n \times 1}$ (n = $2n_1$) is the state vector, $A_c \in \mathbb{R}^{n \times n}$ is the state matrix, $B_c \in \mathbb{R}^{n \times m}$ is

the input matrix.

Eq. (1) thus can simplified as

$$\dot{x}(t) = A_c x(t) + B_c u(t) \tag{4}$$

Assume the output vector $y(t) \in \mathbb{R}^{l\times 1}$ composed of accelerations, velocities, and displacements, it can be expressed as

$$y(t) = C_a \ddot{U}(t) + C_v \dot{U}(t) + C_d U(t) \tag{5}$$

Combing Eq. (5) and Eq. (1), it gives

$$y(t) = C_a M^{-1}\left[\eta u(t) - C_2 \dot{U}(t) - KU(t)\right] + C_v \dot{U}(t) + C_d U(t) \tag{6}$$

or in a simplified form

$$y(t) = C_c x(t) + D_c u(t) \tag{7}$$

where $C_c = \left[C_d - C_a M^{-1} K \quad C_v - C_a M^{-1} C_2\right]$, $D_c = C_a M^{-1}\eta$, the $C_c \in \mathbb{R}^{l\times n}$ is the output influence matrix, $D_c \in \mathbb{R}^{l\times m}$ is the direct transmission matrix.

Equations (4) and (7) are the state-space equations of the dynamic system, which constitute the continuous-time state-space model. The order of the system is the dimension of the state matrix A_c. In most studies including this one, the accelerations are the only measurements, thus, output vector y(t) can be changed accordingly in the computation.

In reality, the vibration measurements are in discrete fashion. Suppose the constant time interval is Δt, the discrete-time model can be derived as

$$\begin{aligned} x(k+1) &= Ax(k) + Bu(k) \\ y(k) &= Cx(k) + Du(k) \end{aligned} \tag{8}$$

where the elements in the Eq. (8) are defined as

$$A = e^{A_c \Delta t};\;\; B = \int_0^{\Delta t} B_c e^{A_c \tau'} d\tau';\;\; C = C_c;\;\; D = D_c$$
$$x(k+1) = x[(k+1)\Delta t];\;\; u(k) = u(k\Delta t) \tag{9}$$

If A_c is asymptotically stable, i.e., the real parts of the eigenvalues are all negative, the A and B in Eq. (9) can be expanded into Taylor series and the series can converge. If all the eigenvalues A_c are non-zero values, B can be computed by $B = [A - I]A_c^{-1}B_c$. The zero eigenvalues in the continuous-time dynamic model means rigid body modes.

The process noise w(k) due to disturbance and modeling inaccuracies, as well as observation noise v(k) due to device inaccuracies can be included into Eq. (8)

$$\begin{aligned} x(k+1) &= Ax(k) + Bu(k) + w(k) \\ y(k) &= Cx(k) + Du(k) + v(k) \end{aligned} \tag{10}$$

The noise cannot be measured, but is assumed to be zero mean white vector sequence with covariance

$$E\left[\begin{pmatrix} w_p \\ v_p \end{pmatrix}\begin{pmatrix} w_q^T & v_q^T \end{pmatrix}\right] = \begin{bmatrix} Q & S \\ S^T & R \end{bmatrix}\delta_{pq} \tag{11}$$

where E denotes the expected values δ_{pq} denotes the Kronecker delta.

Equations (8) and (9) are the state-space discrete-time model for the deterministic system. Equation (10) is the state-space model for the combined deterministic-stochastic system. The subspace identification algorithms for these systems can be found in [4]. It must be stated that in this study, the focus is on the stochastic system.

For the ambient vibration tests or real-time monitoring of structures, the u(k) is unknown and omitted, therefore the input are modeled implicitly by noise only. However, the white noise assumption is still needed. The state-space equations of stochastic system are

$$\begin{aligned} x(k+1) &= Ax(k) + w(k) \\ y(k) &= Cx(k) + v(k) \end{aligned} \tag{12}$$

The w_k and v_k are zero mean white noise vector with covariances as in Eq. (11), independent of x_k,

$$E[w(k)] = 0; \quad E[v(k)] = 0; \quad E[x(k)w^T(k)] = 0; \quad E[x(k)v^T(k)] = 0 \tag{13}$$

The stochastic process is assumed to be stationary, i.e.,

$$\begin{aligned} E[x(k)] &= 0 \\ E[x(k)x^T(k)] &= \Sigma^{STY} \end{aligned} \tag{14}$$

Here the covariance matrix Σ^{STY} is independent of the time k, which implies that A is stable. The output covariances can be defined as

$$E[y(k+i)y^T(k)] = \Lambda(i) \tag{15}$$

The cross covariance of state and output is defined as

$$E[x(k+1)y^T(k)] = G \tag{16}$$

It is easy to derive the following properties

$$\begin{aligned} \Sigma^{STY} &= A\Sigma^{STY}A^T + Q; \quad G = A\Sigma^{STY}C^T + S \\ \Lambda(0) &= C\Sigma^{STY}C^T + R; \quad \Lambda(i) = CA^{i-1}G \end{aligned} \tag{17}$$

Equation (17) conveys that the output covariances can be treated as Markov parameters of the deterministic linear time-invariant system, which are A, G, C, $\Lambda(0)$. More stochastic state-space models are displayed in [4]. All of these models are equivalent in nature.

Some notations used for the subspace algorithms are introduced here. The block Hankel matrices are vital in the algorithm; they are constructed using the output data.

$$Y_{0|2i-1} \triangleq \left[\begin{array}{cccc} y_0 & y_1 & \cdots & y_{j-1} \\ y_1 & y_2 & \cdots & y_j \\ \cdots & \cdots & \cdots & \cdots \\ y_{i-1} & y_i & \cdots & y_{i+j-2} \\ \hline y_i & y_{i+1} & \cdots & y_{i+j-1} \\ y_{i+1} & y_{i+2} & \cdots & y_{i+j} \\ \cdots & \cdots & \cdots & \cdots \\ y_{2i-1} & y_{2i} & \cdots & y_{2i+j-2} \end{array}\right] \triangleq \left[\begin{array}{c} Y_{0|i-1} \\ \hline Y_{i|2i-1} \end{array}\right] \triangleq \left[\begin{array}{c} Y_P \\ \hline Y_f \end{array}\right] = \left[\begin{array}{c} Y_{0|i} \\ \hline Y_{i+1|2i-1} \end{array}\right] \triangleq \left[\begin{array}{c} Y_P^+ \\ \hline Y_f^- \end{array}\right] \tag{18}$$

The number of block rows (i) should be large enough to obtain sufficient information, which at least needs to be greater than the order of the system that is expected to be identified. Let s denote the number of time samples. The number of columns (j) is usually s-2i+1.

The extended observability matrix is defined as

$$\mathcal{O}(i) \triangleq \left[\begin{array}{c} C \\ CA \\ CA^2 \\ \cdots \\ CA^{i-1} \end{array}\right] \in \mathbb{R}^{li \times n} \tag{19}$$

The {A,C} is assumed to be observable, which indicates that all the modes of the system can be observed. The reversed extended stochastic controllability matrix is defined as

$$\mathcal{C}(i) \triangleq \left[\begin{array}{cccc} A^{i-1}G & A^{i-2}G & \cdots & AG \quad G \end{array}\right] \in \mathbb{R}^{n \times li} \tag{20}$$

The pair $\{A,Q^{1/2}\}$ is assumed to be observable, which indicates that all the modes of the system can be excited by noise. The block Toeplitz matrices T_i can be obtained from the output covariance matrices

$$T(i)=\begin{bmatrix} \Lambda(i) & \Lambda(i-1) & \cdots & \Lambda(2) & \Lambda(1) \\ \Lambda(i+1) & \Lambda(i) & \cdots & \Lambda(3) & \Lambda(2) \\ \Lambda(i+2) & \Lambda(i+1) & \cdots & \Lambda(4) & \Lambda(3) \\ \cdots & \cdots & \cdots & \cdots & \cdots \\ \Lambda(2i-1) & \Lambda(2i-2) & \cdots & \Lambda(i+1) & \Lambda(i) \end{bmatrix} \in \mathbb{R}^{li\times li} \tag{21}$$

2.2 Covariance-driven based stochastic subspace identification

Based on equations (15) and (21), and the assumption of ergodicity, the block Toeplitz matrix can be written as the output function

$$T(i)=Y_f Y_p^T \tag{22}$$

From equations (17)-(21) , the block Toeplitz matrix T_i can be decomposed into

$$T(i)=\mathcal{O}(i)\mathcal{C}(i) \tag{23}$$

Decomposing the block Toeplitz matrix by singular value decomposition (SVD)

$$T(i)=USV^T=\begin{bmatrix} U_1 & U_2 \end{bmatrix}\begin{bmatrix} S_1 & 0 \\ 0 & 0 \end{bmatrix}\begin{bmatrix} V_1^T \\ V_2^T \end{bmatrix}=U_1 S_1 V_1^T \tag{24}$$

where $U\in\mathbb{R}^{li\times li}$ and $V\in\mathbb{R}^{li\times li}$ are orthonormal matrices, S is a diagonal matrix, S_1 is a diagonal matrix with the zero diagonal values omitted. In the real world application, the values that are essentially small are treated as zeros and omitted. From equations (23) and (24), the extended observability and reversed extended observability matrices are obtained as

$$\mathcal{O}(i)=U_1 S_1^{1/2};\ \ \mathcal{C}(i)=S_1^{1/2}V_1^T \tag{25}$$

From the definitions of the $\mathcal{O}(i)$ and $\mathcal{C}(i)$, it is clear that the first l rows of $\mathcal{O}(i)$ are equal to the matrix C, and the last l columns of $\mathcal{C}(i)$ are equal to the matrix G.

Define T(i+1) to be

$$T(i+1)=\begin{bmatrix} \Lambda(i+1) & \Lambda(i) & \cdots & \Lambda(3) & \Lambda(2) \\ \Lambda(i+2) & \Lambda(i+1) & \cdots & \Lambda(4) & \Lambda(3) \\ \Lambda(i+3) & \Lambda(i+2) & \cdots & \Lambda(5) & \Lambda(4) \\ \cdots & \cdots & \cdots & \cdots & \cdots \\ \Lambda(2i) & \Lambda(2i-1) & \cdots & \Lambda(i+2) & \Lambda(i+1) \end{bmatrix} \in \mathbb{R}^{li\times li}$$

then

$$T(i+1)=\mathcal{O}(i)A\mathcal{C}(i) \tag{26}$$

Matrix A is obtained by solving Eq. (26)

$$A=\mathcal{O}^{\dagger}(i)T(i+1)\mathcal{C}^{\dagger}(i) \tag{27}$$

The $(\cdot)^{\dagger}$ here denotes Moore-Penrose pseudoinverse.

2.3 Data-driven based stochastic subspace identification

The principles and computational steps of the data-driven SSI method are introduced briefly and used in processing the ambient vibration data in this study.

The Kalman filter plays a vital role in deriving the algorithms for stochastic subspace identification. It is used to optimally predict the state vector, and can be defined by the following recursive formulas

$$\begin{aligned} \hat{x}(k) &= A\hat{x}(k-1)+K(k-1)(y(k-1)-C\hat{x}(k-1)) \\ K(k-1) &= (G-AP(k-1)C^T)(\Lambda(0)-CP(k-1)C^T)^{-1} \\ P(k) &= AP(k-1)A^T+(G-AP(k-1)C^T) \\ &\quad \times(\Lambda(0)-CP(k-1)C^T)^{-1}(G-AP(k-1)C^T)^T \end{aligned} \tag{28}$$

where hat (^) denotes the prediction, and the other symbols are same as those in section 2.1.

The forward Kalman filter state sequence is defined as

$$\hat{X}(i)=[\hat{x}(i) \quad \hat{x}(i+1) \quad \cdots \quad \hat{x}(i+j-1)] \in \mathbb{R}^{n\times j} \tag{29}$$

This sequence can be recovered from the observation data by the SSI algorithm. The backward Kalman filter can be found in [4], which is beyond the scope of this study.

Using the terms of Eq. (18), the projection of row space of future outputs on row space of past outputs is defined as

$$\mathcal{P}(i) = Y_f \,/\, Y_p = Y_f Y_p^T (Y_{\ p} Y_p^T)^{\dagger} Y_p \tag{30}$$

and the SVD of the projection is

$$\mathcal{P}(i) = \begin{bmatrix} U_1 & U_2 \end{bmatrix} \begin{bmatrix} S_1 & 0 \\ 0 & 0 \end{bmatrix} \begin{bmatrix} V_1^T \\ V_2^T \end{bmatrix} = U_1 S_1 V_1^T \tag{31}$$

The main theorem for stochastic subspace identification algorithm in [4] clarifies that

$$\mathcal{P}(i) = \mathcal{O}(i)\hat{X}(i) \tag{32}$$

Because rank ($\mathcal{P}(i)$) = n, $U_1 \in \mathbb{R}^{li \times n}$; $S_1 \in \mathbb{R}^{n \times n}$; $V_1 \in \mathbb{R}^{j \times n}$. From equations (31) and (32), the following extended observability and Kalman filter state sequence are given as

$$\begin{aligned} \mathcal{O}(i) &= U_1 S_1^{1/2} \\ \hat{X}(i) &= \mathcal{O}^{\dagger}(i)\mathcal{P}(i) \end{aligned} \tag{33}$$

The order of the system n can be determined as the number of non-zero singular values of S_1 or the singular values greater than a user-defined small value. Let $\mathcal{O}(i-1)$ denote $\mathcal{O}(i)$ without the last l rows, thus the following equations can be derived

$$\mathcal{P}(i-1) \triangleq Y_f^- \,/\, Y_p^+ = \mathcal{O}(i-1)\hat{X}_{i+1} \tag{34}$$

$$\hat{X}_{i+1} = \mathcal{O}^{\dagger}(i-1)\mathcal{P}(i-1) \tag{35}$$

The following equation can now be obtained below

$$\begin{pmatrix} \hat{X}(i+1) \\ Y(i \mid i) \end{pmatrix} = \begin{pmatrix} A \\ C \end{pmatrix} \left(\hat{X}(i) \right) + \begin{pmatrix} \rho_w \\ \rho_v \end{pmatrix} \tag{36}$$

where Y(i|i) is a block Hankel matrix with one row of output data, the Kalman filter state and the output are known, ρ_w and ρ_v are the Kalman filter residuals uncorrelated with $\hat{X}(i)$, The matrices A and C can therefore be solved by least square method as

$$\begin{pmatrix} A \\ C \end{pmatrix} = \begin{pmatrix} \hat{X}(i+1) \\ Y(i \mid i) \end{pmatrix} \left(\hat{X}^{\dagger}(i) \right) \tag{37}$$

Solving the Lyapunov equation results in

$$\Sigma^{STY} = A \Sigma^{STY} A^T + Q \tag{38}$$

and then using Eq. (17) to compute G and $\Lambda(0)$

$$\begin{aligned} G &= A \Sigma^{STY} C^T + S \\ \Lambda(0) &= C \Sigma^{STY} C^T + R \end{aligned} \tag{39}$$

Now the matrices A, C, G, and $\Lambda(0)$ are all available for modal analysis.

The above computation is based on all the available output data. Peeters and De Roeck [10] proposed an extension of the SSI algorithm called reference-based stochastic identification for output only modal analysis that used reduced output data.

2.4 Extraction of modal characteristics

The modal characteristics include modal frequencies and damping ratios, mode shapes, and modal participation factors. In the output only system identification, the last term cannot be identified, while all the other parameters can be determined from the discrete state matrices A and C.

The matrix A can be decomposed as

$$A = \Psi D \Psi^{-1} \tag{40}$$

where $D = diag(\lambda_r) \in \mathbb{C}^{n \times n}$, r = 1, 2,⋯, n, is a diagonal matrix containing the discrete time

complex eigenvalues, columns of $\Psi \in \mathbb{C}^{n\times n}$ contains the corresponding eigenvectors. For a continuous time system, the continuous state matrix A_c can be decomposed as

$$A_C = \psi_C D_C \psi_C^{-1} \tag{41}$$

where $D_c = diag(\lambda_{c,r}) \in \mathbb{C}^{n\times n}$, r = 1, 2, ···, n, is a diagonal matrix containing the continuous time complex eigenvalues, columns of $\Psi_c \in \mathbb{C}^{n\times n}$ contains the corresponding eigenvectors. These eigenvalues and eigenvectors for the continuous-time state matrix are the same as those for the equation of motion of the structure in Eq. (1).

Recall the relationship in Eq. (9)

$$A = e^{A_C \Delta t};\ \ C = C_c \tag{42}$$

It is easy to derive that

$$\lambda_{c,r} = \frac{\ln(\lambda_r)}{\Delta t};\ \ \Psi_c = \Psi \tag{43}$$

The eigenvalues of A_c can be expressed as the following pairs

$$\lambda_{c,r}, \lambda^*_{c,r} = -\xi_r \omega_r \pm j\omega_r \sqrt{1-\xi_r^2} \tag{44}$$

where ω_r is the circular modal frequency of mode r, and ξ_r is the modal damping ratio of mode r.

The mode shapes can be computed from the eigenvectors and observation matrix

$$\Phi = C_c \Psi_c = C\Psi \tag{45}$$

Analyzing the real measurements usually results in complex modes, whereas for light damping system, we use the amplitudes of complex mode shape with signs of the corresponding real parts to draw them as real mode shapes.

2.5 Stabilization diagrams

Based on the practice of subspace identification algorithms for processing real measurements, the results are not satisfactory using only one or a few estimated model orders. To improve accuracy and reliability, it is essential to specify excessive model orders and to separate the numerical modes later. The stabilization diagram was developed to address this issue, and has been widely used in structural identification [1, 10-12] and other fields. In the diagram, the estimated frequencies, damping ratios, and modal vectors associated with the increasing model orders are plotted.

Distinguishing the physical (true) modes from the numerical (spurious) modes is the most important step. The non-physical modes present only at certain model orders and should be excluded. If the differences in the frequencies, damping ratios, and mode shapes associated with a range of model orders don't exceed specified criteria, the poles under inspection are regarded as stable; otherwise, they will be eliminated. The criteria are typically 1%, for frequencies, 5%~10% for damping ratios, and 1%~5% for mode shape correlations by modal assurance criteria (MAC). In order to exclude the incidentally stable modes, the poles with q ($q>1$) times stable will be considered as physical poles. The value of q is flexible, while it is taken as 5 in some literature [12].

Experienced engineers are needed to analyze the diagrams, and to eliminate the numerical modes and keep the physical modes. The method is very expensive and time consuming due to large number of poles, and the accuracy of results by the stabilization diagrams highly depends on the analyst. To address this issue, efforts have been made to develop automated procedures to analyze stabilization diagrams [11, 13-14]. For the current study in this chapter, the stabilization diagrams have been assessed manually.

3. The Application of Subspace Identification in Modal Identification of Bridge Structures by Using Ambient Vibration Measurements

The effectiveness of the SSI method was investigated by the application in the modal identification of a numerical bridge truss example and an actual highway bridge from output only measurements.

3.1 Numerical example: The use of the SSI method on a plane truss bridge

In the numerical example, a plane truss bridge model is supported at two ends as illustrated in Figure 3, where the node and element numbers are exhibited. Each node has 2 degrees of freedom, i.e., horizontal (x) and vertical (y) translations.

The equation of motion of the system can be written as

$$M\ddot{X} + C\dot{X} + KX = F \tag{46}$$

where M, C, K stand for mass, damping, and stiffness matrices, respectively, X is the displacement vector, and dot (·) denotes the derivative respect to time and F is the vector for external excitation. The stiffness and mass matrices of the entire truss structure may be obtained from

$$K = \sum_{e=1}^{n} K^e = \sum_{e=1}^{n} L^e k^e (L^e)^T;\ M = \sum_{e=1}^{n} M^e = \sum_{e=1}^{n} L^e m^e (L^e)^T \tag{47}$$

where L^e is position vector, and the global stiffness and mass matrices are

$$k^e = E_i A_i / l_i \begin{bmatrix} c^2 & cs & -c^2 & -cs \\ cs & s^2 & -cs & -s^2 \\ -c^2 & -cs & c^2 & cs \\ -cs & -s^2 & cs & s^2 \end{bmatrix};\ m^e = \rho_i / 6 \begin{bmatrix} 2c^2 & 2cs & c^2 & cs \\ 2cs & 2s^2 & cs & s^2 \\ c^2 & cs & 2c^2 & 2cs \\ cs & s^2 & 2cs & 2s^2 \end{bmatrix} \tag{48}$$

where $c = \cos\theta_i$, $s = \sin\theta_i$, and θ represents the angles between members as shown in Figure 3, E denotes Young's modulus, A denotes cross-sectional area, and ρ is mass

density. The Rayleigh damping is used to obtain the damping matrix C = αM+ βK. The two damping coefficients are chosen as α = 0.566; β = 8.62 $\times 10^{-4}$. The structural properties are the same as those of the truss bridge model in [15] and listed in section 5.3 of Chapter III.

Sinusoidal force $F(t) = \sum_{i=1}^{n} a_i \sin(2\pi f_i t)$ was applied at node 3 in the y direction. The sinusoidal force F(t) consisted of a range of excitation frequencies from 2 Hz to 20 Hz, and some values were chosen for the amplitudes and phases. This sinusoidal excitation may not excite all modes. If white noise is applied as excitation, all the modes may be excited. The sampling rate was 1000 Hz, and the time duration 20 seconds. Damage was simulated by abruptly reducing the stiffness of the symmetrical members 3 and 9: E_3A_3/l_3 and E_9A_9/l_9 from 16617 to 6000 kN/m at t = 10 seconds. All the other values were assumed to be constants all the time. The modal frequencies were consequently reduced, and the damping and mode shapes were also changed as a result. The modal frequencies and damping ratios for the truss in both undamaged and damaged states were denoted as exact values and listed in Table 1.

The dynamic responses, i.e., the displacements, velocities, and accelerations, of the truss bridge were obtained by solving Eq. (46) using Newmark-beta method. The SSI method was then used to extract the modal characteristics from the acceleration responses. In this study, no output noise was added to the acceleration responses. So the following discussions regarding this numerical example were suitable for signals with high signal-to-noise-ratio (SNR).

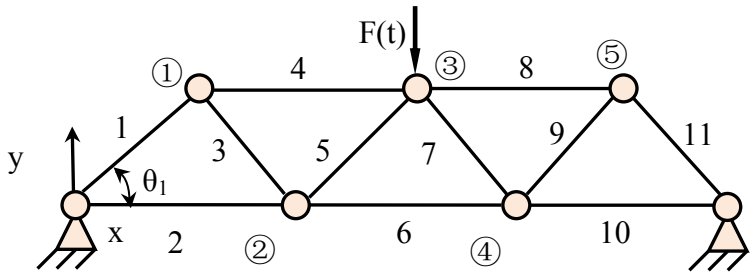

Figure 3. Truss bridge model: the circled numbers denote node numbers and the numbers without circles denote the element number.

The stabilization diagrams with stable frequency and damping ratio for the truss bridge before damage and after damage are shown in Figures 4 and 5, respectively. For both cases, the number of block rows is 400 and the order is from 80 to 100.

For convenience, we can define the difference between the identified values associated with the same mode but different modal orders as uncertainty. It can be observed from these figures that the uncertainties of frequencies are exceptionally low. And the uncertain degree of damping ratio is also very low, but greater than that of frequencies. It is straightforward to determine the modal frequencies and damping ratios from these stabilization diagrams. There were only two numerical (spurious) modes in the stabilization diagrams for damping ratios, and they are eliminated in Figure 4 and Figure 5. These illustrations demonstrate that the frequencies can be identified very well with model order of 80 or even lower. The damping ratios can be determined very well too, but only five damping ratios were determined accurately. An interesting thing is that there are spurious modes with stable frequencies and damping ratios, this may be due to the excitation inputs are deterministic sinusoidal force instead of white noise. So when the SSI and stabilization diagrams are used to process response data due to deterministic input, the identified values associated with stable poles should also be analyzed to determine if they are numerical ones.

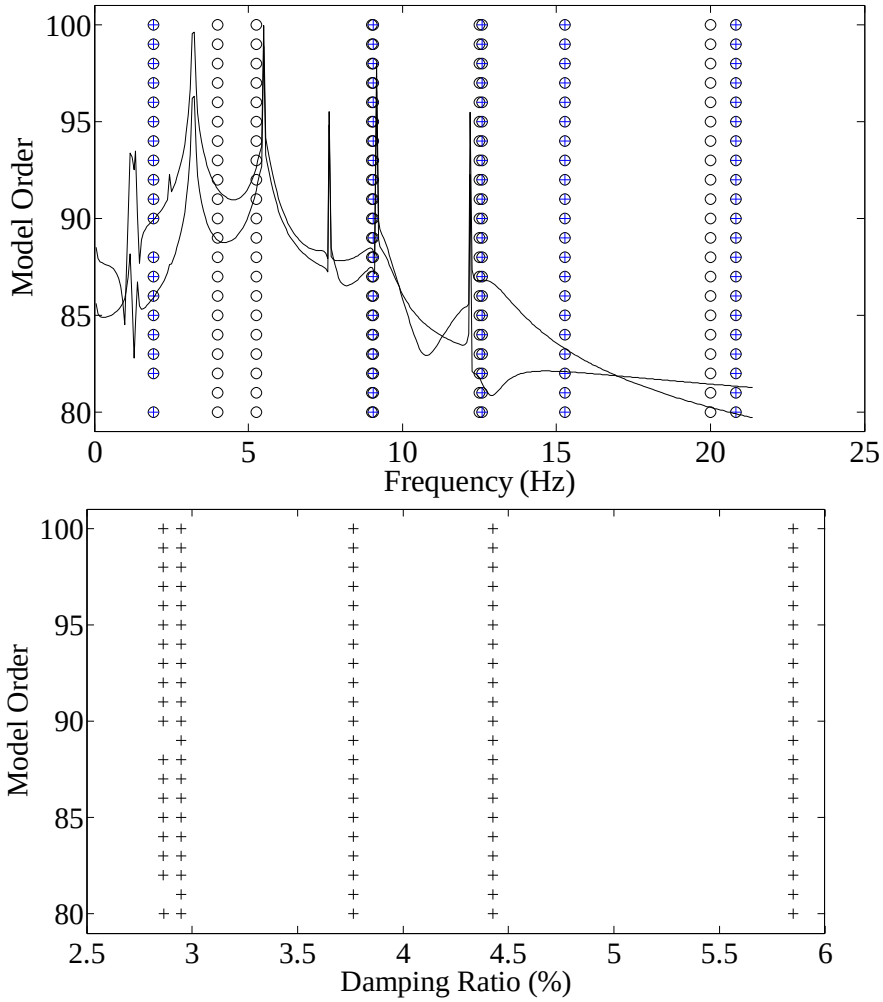

Figure 4. Stabilization diagrams for the truss bridge before damage: upper is for poles with stable frequencies and damping, and lower is for stable damping ratios. The symbols are: '○' for a pole with stable frequency, '+' for a pole with stable damping, and Θ for a pole with stable frequency and damping, curve for a PSD of the response.

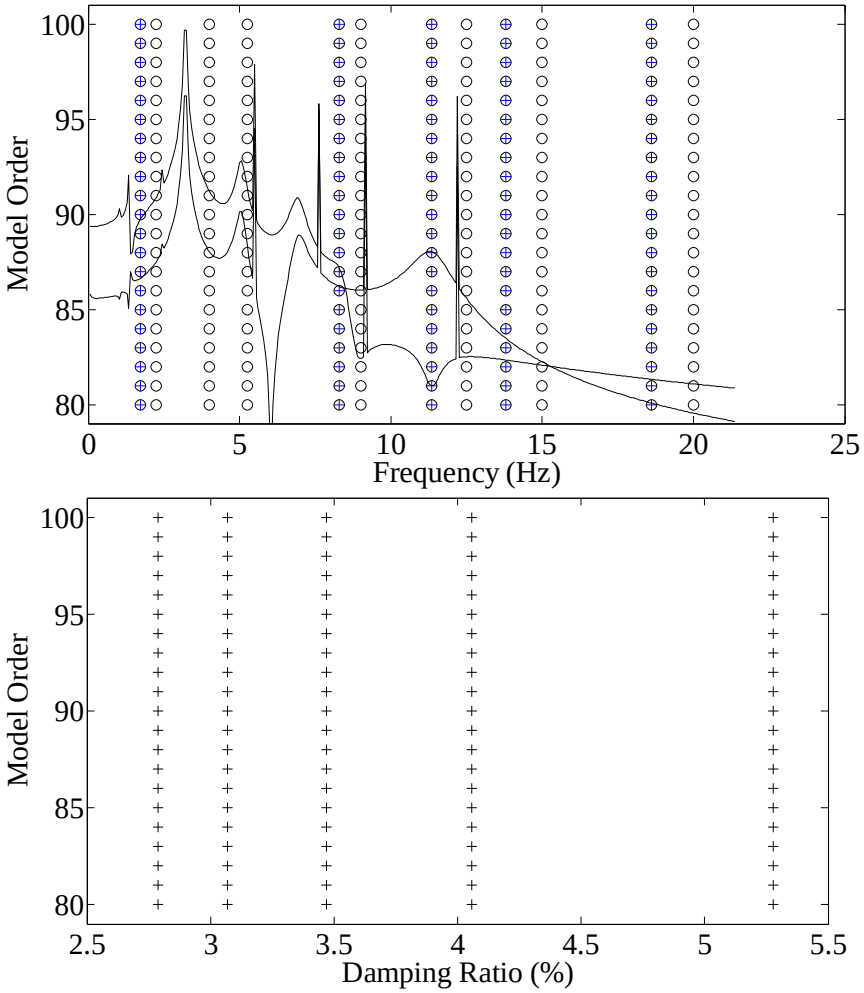

Figure 5. Stabilization diagrams for the truss bridge after damage: upper is for poles with stable frequencies and damping, and lower is for stable damping ratios. The symbols are: '○' for a pole with stable frequency, '+' for a pole with stable damping, and ⊖ for a pole with stable frequency and damping, curve for a PSD of the response.

The frequencies and damping ratios can be determined from the stabilization diagrams. The comparison of the actual and identified frequencies and damping ratios for the truss bridge before damage are listed in Table 1, and those for after damage are listed in Table 2. Note that the percentage differences are based on values with more significant digits than those listed in the tables. For the frequencies before damage, the errors of the 2nd and 3rd modal frequencies were up to 17%, but all the other frequencies were accurate with errors less than 4%, the identified error of 1st modal frequency was only

0.16%. For the frequencies after damage, the errors of the 2nd, 3rd, 5th, and 7th modal frequencies ranged from 7% to 16% while the identified error of 1st, 4th, 6th, 8th, and 9th modal frequencies were less than 0.15%. For both cases of before damage and after damage, 5 modal damping ratios were identified, which have errors of less than 2.5%. This SSI shows its ability to identify the closely spaced modes, e.g., mode 5 and mode 6 of the truss before damage were identified and separated very well as shown in Figure 4 and Table 1. One frequency was not identified; this may be because that this mode was not excited by the sinusoidal excitation.

Table 1. Comparison of the exact and the SSI identified frequencies and damping ratios for the truss before damage.

Mode	Exact values		Identified values		Freq Difference	Damping Difference
	Freq. (Hz)	Damping ratio	Freq. (Hz)	Damping ratio		
1	1.92	2.86%	1.92	2.86%	0.16%	0.09%
2	4.43	2.22%	4.00	-	-9.71%	-
3	6.29	2.42%	5.25	-	-16.53%	-
4	9.05	2.95%	9.05	2.95%	0.02%	-0.06%
5	12.59	3.77%	12.50	-	-0.71%	-
6	12.75	3.81%	12.58	3.76%	-1.31%	-1.20%
7	15.28	4.43%	15.27	4.43%	-0.06%	-0.09%
8	16.43	4.72%	-	-	-	-
9	20.85	5.86%	20.00	-	-4.08%	-
10	21.39	6.00%	20.82	5.85%	-2.68%	-2.48%

Table 2. Comparisons of the exact and the SSI identified frequencies and damping ratios for the truss after damage.

Mode	Exact values		Identified values		Freq Difference	Damping Difference
	Freq. (Hz)	Damping ratio	Freq. (Hz)	Damping ratio		
1	1.73	3.07%	1.73	3.07%	0.15%	-0.04%
2	4.32	2.21%	4.00	-	-7.41%	-
3	5.82	2.35%	5.25	-	-9.79%	-
4	8.29	2.79%	8.28	2.79%	-0.07%	-0.13%
5	10.73	3.33%	9.00	-	-16.12%	-
6	11.36	3.47%	11.35	3.47%	-0.05%	-0.01%
7	13.45	3.98%	12.50	-	-7.06%	-
8	13.80	4.06%	13.79	4.06%	-0.06%	-0.04%
9	18.64	5.29%	18.62	5.28%	-0.09%	-0.21%
10	20.66	5.81%	20.00	-	-3.19%	-

The SSI method obtained the mode shape information from the acceleration responses, and pseudo mode shapes of the 1st mode for the truss bridge before and after damage are plotted in Figure 6. The relative amplitudes of each DOF were available after applying the SSI method. If they were plotted with respect to their real locations they would correspond to real mode shapes. For convenience, the relative amplitudes of each DOF were normalized and plotted with respect to the numbers of DOF.

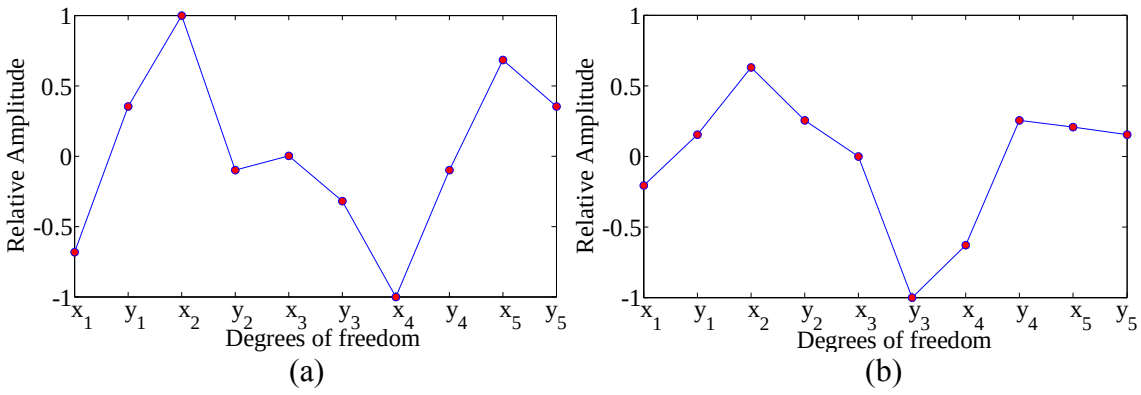

Figure 6. Pseudo mode shapes for the truss bridge identified by the SSI method: (a) before damage corresponding to mode 1 with frequency = 1.92 Hz (b) after damage corresponding to mode 1 with frequency = 1.73 Hz

It can be found in Figure 6 that for both the mode shapes for the truss before and after damage there are: $x_1 = -x_5$, $y_1 = y_5$, $x_2 = -x_4$, and $y_2 = y_4$. These are consistent with the fact that node 1 and node 5 are symmetric about the line of y_3, and node 2 and node 4 are also symmetric about the line of y_3. When the two mode shapes in Figure 6 are compared, it is obvious that the magnitude of y_3 increases significantly after damage; this results from the symmetric damage of members 5 and 7. Also $y_2 = y_4$ becomes larger than $y_1 = y_5$. It can be concluded that the changes of the mode shapes can indicate the damage. This verified that the mode shapes extracted by the SSI method are correct and can be used as damage indicator.

3.2 The use of the SSI algorithm in the modal identification of real vibration measurements of a highway bridge

In this section, the SSI method was used for modal identification of a highway bridge C846 flyover from actual ambient vibration measurements. The C846 flyover bridge is located in Salt Lake City and serves as a connector from westbound I-80 to SR-201 as shown in Figure 7. It sits on soft deep Lake Bonneville sediments and is located just 6 km away from the Wasatch Fault, a large normal fault capable of up to a magnitude 7.5 earthquake event. The bridge is 1.14 km long with 25 spans and is made up of four individual structures. The superstructure consists of a reinforced concrete deck supported by three steel I girders, and the substructure contains tall columns. The bridge has expansion joints to fill gaps between the superstructure and substructure.

A strong motion system was installed by Utah State University to measure the accelerations and transfer them to the Kinematrics Altus K2 digital recorders. The system consists of 18 accelerometers located on the bents and decks of the bridge. These

channels were used to measure the transverse, longitudinal, and vertical accelerations. The data were first transferred to three K2 data loggers called K1656, K2011, and K2650. Basically, K1656 are connected to 1 transverse, 3 longitudinal, and 2 vertical channels; K2011 are connected to 2 transverse, 1 longitudinal, and 3 vertical channels; and K2650 are connected to 3 transverse, and 3 vertical channels. For the layout of the sensors and details of the system, refer to [16]. Since 2007, the data has been streamed to the Utah State University and stored in the MySQL database and can be exported for further analysis.

This section discusses how the SSI method was applied for 150 seconds of` acceleration measurements on June 1st, 2007 to determine modal characteristics of the bridge. The sampling frequency was 200 Hz. The acceleration data from all 18 channels were detrended before modal identification, one typical detrended vertical acceleration response is shown in Figure 8. The forced vibration tests was conducted by Dye [17] on June 2001, an eccentric mass shaker was used to generate sinusoidal forces to the bridge. The environmental conditions for the ambient tests of this section and the forced vibration tests were all in June and similar, therefore the difference between the modal characteristics of these two cases due to the influence of environmental conditions was minimized. The modal frequencies obtained from the forced vibration data by frequency domain decomposition method were used as baseline modal properties to caliber the identified values from the ambient vibration data by the SSI method.

The number of block rows used was 550, and the model orders tested were from 140 to 160. Due to the limitation of the available PC, the 18 channels were separated into 7 for each SSI identification procedure, which is the 6 channels of K1656 with 1 channel

of K2011, the 6 channels of K2011 with 1 channel of K2650, and the 6 channels of K2650 with 1 channel of K1656. The overlap of one channel was done to act as a reference sensor for identification of mode shape. Additionally, because the vertical accelerations are very concerned for the performance evaluation of bridges, the 6 channels of vertical channels were grouped together for SSI identification purposes.

Figure 7. The aerial view of the bridge under monitoring

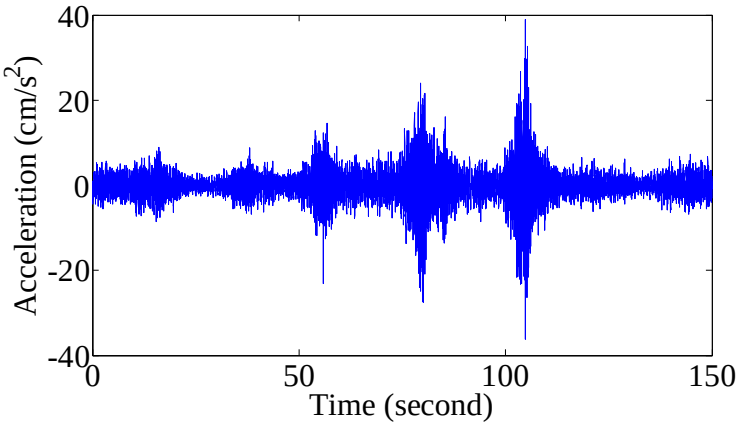

Figure 8. Typical vertical acceleration response measured on the bridge deck (the 3rd channel recorded by K2011).

The stabilization diagram from the vertical accelerations that does not eliminate the spurious modes is illustrated in Figure 9. Both the physical and spurious (numerical) modes are shown in this diagram, which also contains the PSD curve of the acceleration response. It shows that stabilization diagram is able to identify frequencies more clearly and accurate that the PSD plot. The stable frequencies and the damping ratios were combined to determine and keep the physical models, and eliminate the numerical modes. The stabilization diagrams that keep only the physical modes with stable frequencies and damping ratios are shown in Figure 10-Figure 13. The identified values of frequencies and damping ratios are listed in Table 3 and compared with the frequencies obtained from the forced vibration tests in [17].

It can be observed from the stabilization diagrams that the data from K2011 and K2650 provided more stable and accurate identification results than the data from K1656. This is probably because the K1656 have more longitudinal sensors, while the K2011 and K2650 contain more vertical and transverse sensors and most modes are vertical and transverse. Therefore in the bridge health monitoring, vertical and transverse sensors may provide more accurate modal identification results, while the longitudinal sensors are also essential.

The frequencies were clearly identified from the real measurements of the highway bridge as shown in the Figures 10-13. The difference between identified values associated with same mode but different model orders are larger than those in the numerical truss bridge example; this may be due to output noise in the real measurements. Compared with frequencies, the damping ratios carry much more uncertainty than the frequencies do. The identified damping rations are accurate within 3% ratios and many

values of them scatter randomly outside the range of 0%~3%.

Table 3 presents the identified results of frequencies and damping ratios. In this table, the SSI identified frequencies are compared with those identified from force vibration tests, which are closest to the exact values. The errors of the first 18 SSI identified modal frequencies are between 0.00% and 5.34%, which verifies the extreme accuracy of the SSI identified frequencies. The SSI identified damping ratios are also listed in Table 3, most of which (1.34%~5.94%) are within normal range of damping ratios for bridge, which are typically between 2% and 7% for concrete bridges and can be higher values in cases where the bridge is heavily influenced by soil-structure interaction or energy dissipation [18]. Thus the damping ratios obtained in this study by the SSI algorithms and stabilization diagrams were validated to be reasonable values. Since damping ratios were not obtained from the forced vibration tests in [17], the damping ratios obtained from the ambient vibration data in this study did not have baseline data to be compared, and further studies may be conducted to obtain these ratios from the forced vibration test data to verify the corresponding values from the ambient vibration data.

The mode shapes were also obtained from the acceleration measurements by the SSI method. Since the sensors are sparse in this bridge, the mode shape information is not considered in the stabilization diagrams in this dissertation. The mode shape information is available for the ongoing research.

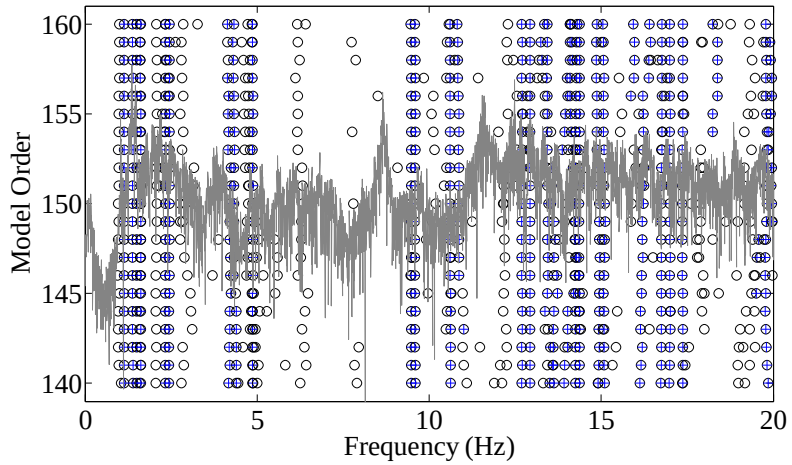

Figure 9. Stabilization diagrams obtained from the measurements of the 6 vertical channels before elimination of spurious modes. The symbols are: '○' for a pole with frequency, '+' for a pole with stable damping, curve for a PSD of acceleration response.

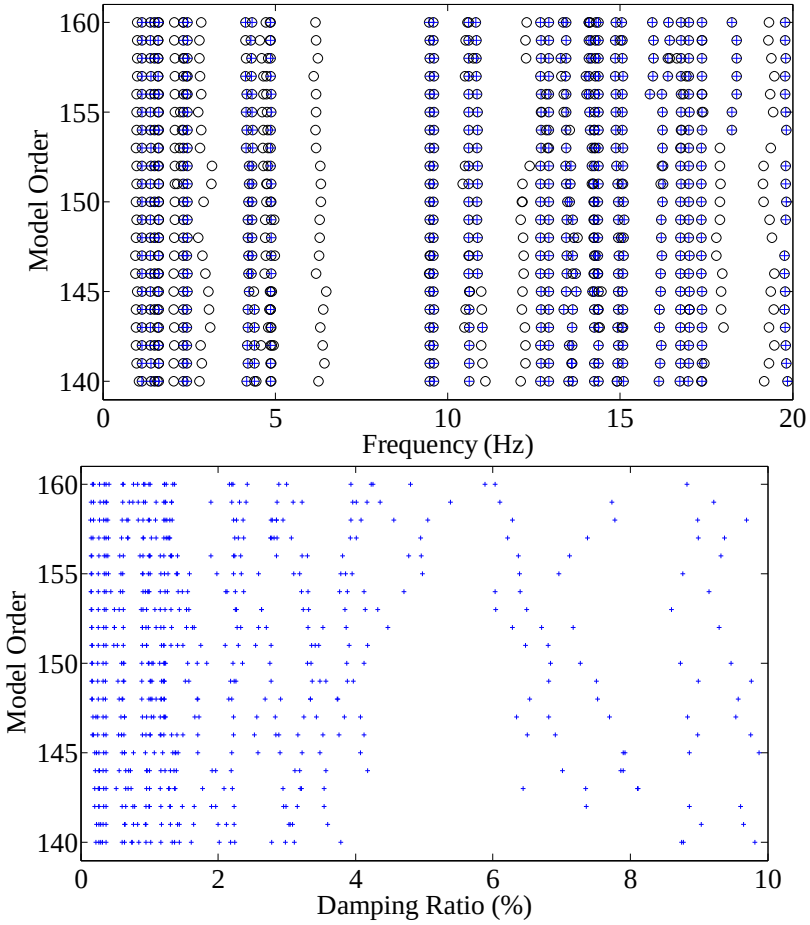

Figure 10. Stabilization diagrams obtained from the measurements of the 6 vertical channels: upper is for poles with stable frequencies and damping, and lower is for damping ratios. The symbols are: '○' for a pole with stable frequency, '+' for a pole with stable damping, and ⊖ for a pole with stable frequency and damping.

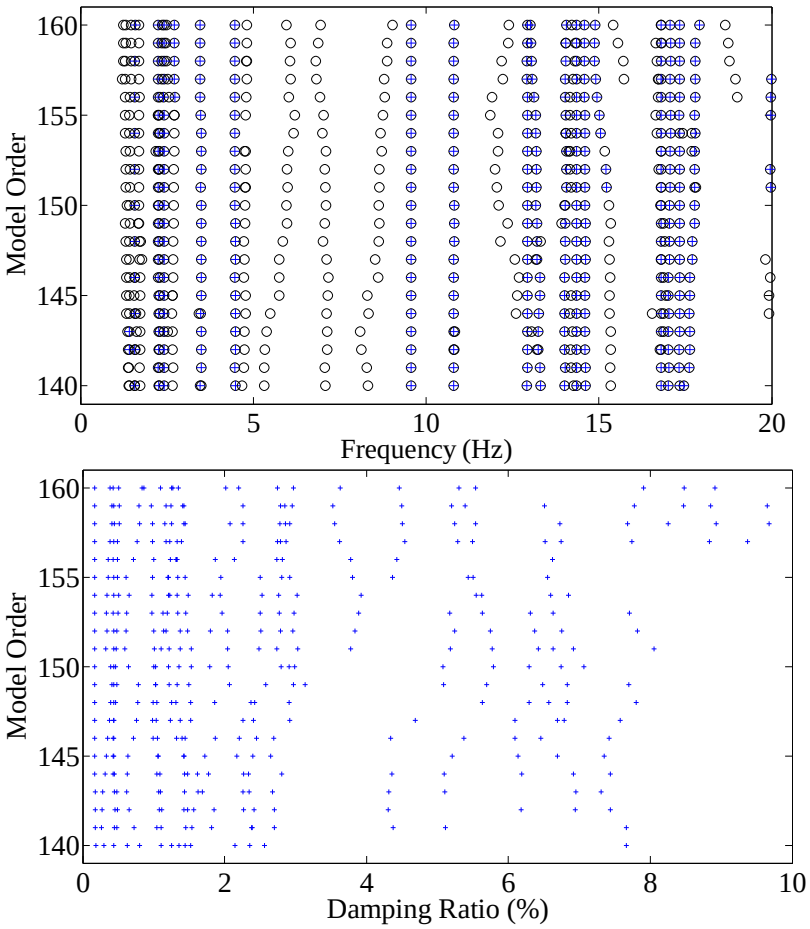

Figure 11. Stabilization diagrams obtained from the measurements of K1656 and a K2011 channel: upper is for poles with stable frequencies and damping, and lower is for damping ratios. The symbols are: '○' for a pole with stable frequency, '+' for a pole with stable damping, and Θ for a pole with stable frequency and damping.

3.3 The application of the subspace identification method N4SID in the modal identification of the highway bridge from ambient vibration measurements

Numerical algorithms for subspace state space system identification (N4SID) [6] has some advantages over other SSI algorithms because it does not require most of the a priori parameters; only the modal order is needed. It is non-iterative and is without nonlinear optimization part; therefore, it is numerically robust. N4SID can be used for output-only systems as well as input-output systems. By using N4SID, Skolnik et al. [19]

acquired frequencies, mode shapes, and damping ratios of a 15-story steel-frame building from the Parkfield earthquake as well as ambient vibration measurements. This section utilizes N4SID to investigate its effectiveness in obtaining modal characteristics of the highway bridge C846 flyover described in section 7.2 from its ambient vibration measurements.

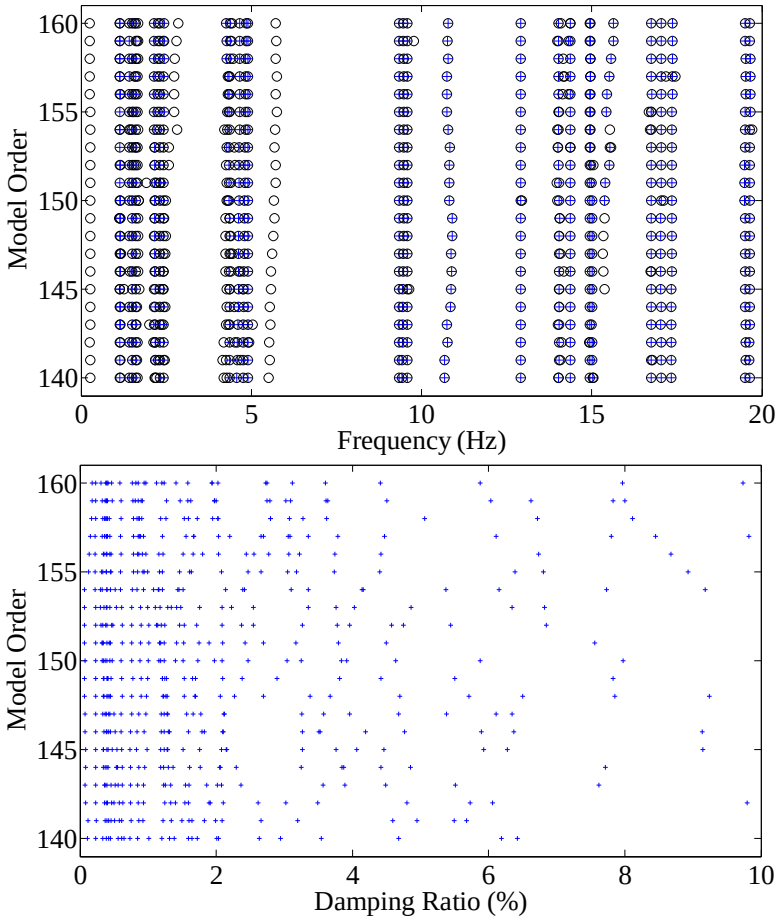

Figure 12. Stabilization diagrams obtained from the measurements of K2011 and a K2650 channel: upper is for poles with stable frequencies and damping, and lower is for damping ratios. The symbols are: '○' for a pole with stable frequency, '+' for a pole with stable damping, and ⊖ for a pole with stable frequency and damping.

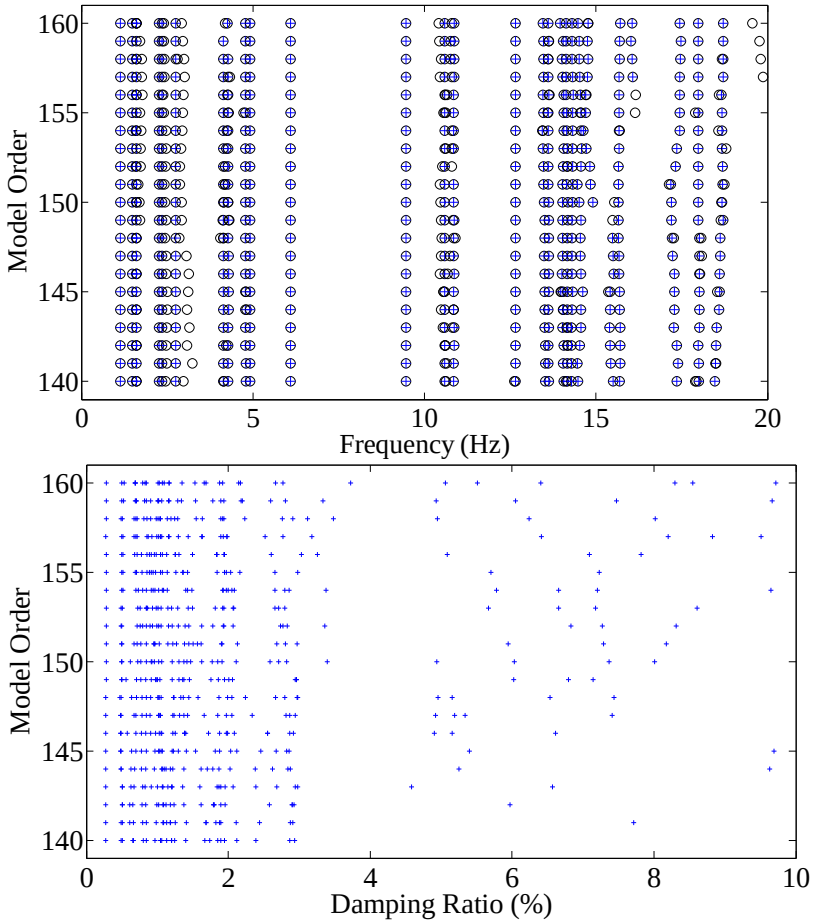

Figure 13. Stabilization diagrams obtained from the measurements of K2650 and a K1656 channel: upper is for poles with stable frequencies and damping, and lower is for damping ratios. The symbols are: '○' for a pole with stable frequency, '+' for a pole with stable damping, and Θ for a pole with stable frequency and damping.

Basic formulations of modal analysis using N4SID are described below. In the case of ambient vibration, the input is implicitly accounted for by unknown noise w; a linear time-invariant structural model can be described by the discrete 1st order difference equation

$$x(k+1) = Ax(k) + w(k) \tag{49}$$

$$y(k) = Cx(k) + v(k) \tag{50}$$

where k is the sampling instant ($t = k\Delta t$), x is state vector and A is the state matrix, C is

the output matrix, w is the process noise and v is the measurement noise, w and v are assumed as uncorrelated zero-mean stationary white noise vector sequences [20].

Table 3. Identified frequencies and damping ratios from the ambient vibrations and the comparison of them with the results identified from forced vibrations.

Frequency identified from forced vibration tests (Hz) in [17]	Frequency identified from ambient vibration data by SSI (Hz)	Damping ratio identified from ambient vibration by SSI	Frequency differences
1.11	1.13	2.87%	1.71%
1.31	1.38	2.72%	5.34%
1.49	1.49	1.34%	0.00%
1.58	1.58	2.01%	-0.18%
1.76	1.72	5.94%	-2.27%
2.25	2.24	2.75%	-0.33%
2.37	2.35	1.92%	-0.81%
2.70	2.72	4.46%	0.66%
3.07	3.13	-	2.05%
3.49	3.46	2.97%	-0.77%
4.25	4.26	3.73%	0.20%
4.72	4.78	1.17%	1.24%
5.17	4.91	0.69%	-4.99%
5.58	5.72	7.97%	2.47%
6.15	6.11	1.06%	0.65%
7.30	7.13	7.44%	-2.33%
8.97	9.35	0.89%	4.23%
10.70	10.80	2.79%	0.89%
11.75	10.96	5.27%	-6.72%
13.00	12.70	1.31%	-2.31%
14.29	14.30	1.01%	0.13%
15.59	15.64	4.41%	0.31%
17.08	17.06	1.10%	-0.14%

The complex eigenvalues (λ) and eigenvectors (ψ) of the damped system can be calculated from the system matrix A. The natural frequency f_k and the damping ratio ς_k are

$$\omega_k = \frac{|\ln(\lambda_k)|}{\Delta t}; \qquad f_k = \frac{\omega_k}{2\pi}; \qquad \varsigma_k = \frac{-\mathrm{Re}[\ln(\lambda_k)]}{\omega_k \Delta t} \tag{51}$$

The k^{th} complex mode shape ϕ_k sampled at sensor locations can be evaluated using the following expression

$$\phi_k = C\psi_k \tag{52}$$

If the damping is assumed to be small and nearly classical, then the modal properties of the undamped structure can be approximated as [21]

$$f_k = \frac{|\lambda_k|}{2\pi}; \qquad \varsigma_k = \frac{\mathrm{Re}(\lambda_k)}{2\pi f_k}; \qquad \phi_k = |C\psi_k| \mathrm{sign}[\mathrm{Re}(C\psi_k)] \tag{53}$$

N4SID was applied to the ambient vibration data of one accelerometer on February 21, 2008. The duration of the dataset was 300 seconds, and the sampled frequency was 200 Hz. The data had been detrended to remove the mean shift from zero due to sensor inaccuracies before modal analysis. The frequencies, mode shapes, and damping ratios were determined, while the frequencies were presented in this study to be examined.

Determination of the order of the state-space model, i.e., dimension of the state vector x(k), is an important step for implementation of the subspace method. Theoretically, an N-DOF system will have an order of 2N. The N4SID has been conducted with an order number from 60 to 540 with step of 40, and the representative results are demonstrated in the stabilization diagram shown in Figure 14. It can be

determined that N4SID needs a much larger order number than the theoretical value of 2N, greater than 140 in this study, to achieve accurate results and obtain modal characteristics of sufficient modes. This figure also shows that most mode frequencies can be identified; the larger the order, the more modal frequencies can be identified, but this also means that more spurious modes will be created. As the order number increased, the computational time also increased rapidly; this is a disadvantage of N4SID found in this study.

Table 4 lists the identified frequencies based on the stabilization diagram, which is compared with those frequencies identified from forced vibration data described in section 3.2, which are identified by frequency domain decomposition method. The frequencies obtained from the forced vibration data can be understood as values that are closest to the actual values. The two sets of frequencies in Table 4 correspond with differences of 0.16%~7.59%. The variation between them is due to many factors besides the modal analysis methods. The previous results are from forced vibration data from all the 18 channels in 2002, and the N4SID results from this study only processed the data from 1 channel only in 2008. Further studies are needed to examine the effectiveness of N4SID using same sets of data as those for forced vibration test.

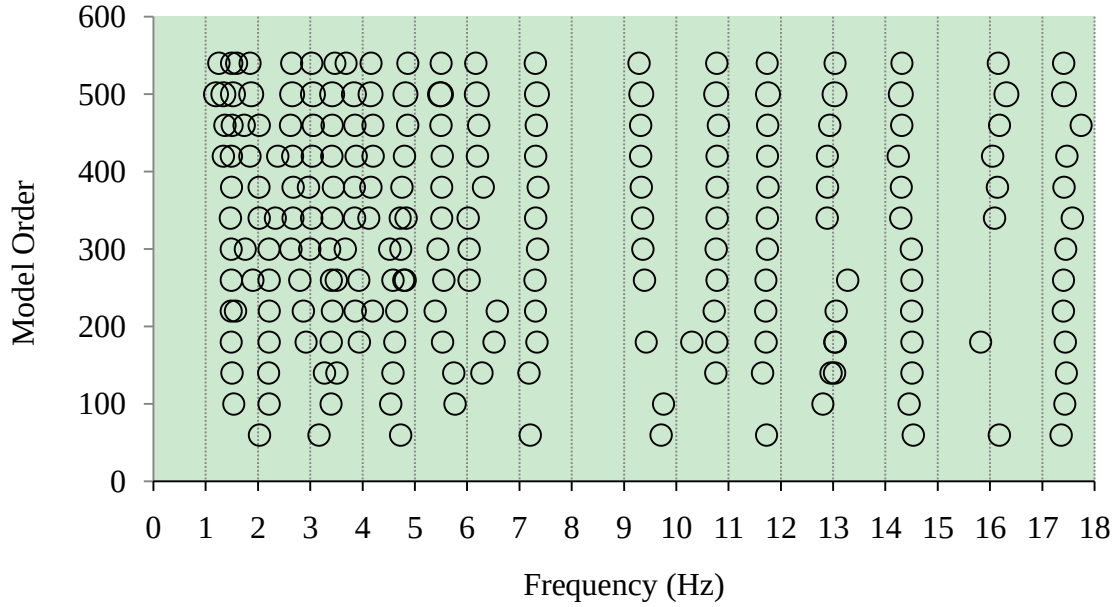

Figure 14. Stabilization diagram of frequencies by N4SID from ambient vibration measurements.

Table 4. Comparison of frequencies identified by N4SID from ambient vibration data with those from forced vibration tests in Dye [17].

Identified from forced vibration (Hz)	1.11	1.48	1.58	1.76	2.70	3.07	3.49
Identified from ambient vibration by N4SID (Hz)	1.19	1.50	1.59	1.85	2.64	3.03	3.47
Difference (%)	7.59	1.01	0.63	5.11	-2.22	-1.30	-0.57
Identified from forced vibration (Hz)	5.58	6.15	7.30	8.97	10.7	11.75	13.00
Identified from ambient vibration by N4SID (Hz)	5.50	6.16	7.30	9.28	10.80	11.70	13.00
Difference (%)	-1.43	0.16	0.00	3.46	0.93	-0.43	0.00

4. Effects of Temperature on the Modal Frequencies

Much research has concluded that environmental conditions can affect the dynamic behavior of structures. These environmental conditions include temperature, humidity, wind, and excitation amplitudes. The change in temperature can have a great

effect on material properties and boundary conditions, which consequently has an impact on the stiffness and frequencies. Young's moduli of concrete and asphalt decrease when the temperate increases. The frequencies are proportional to the square root of Young's modulus, $f \sim E^{1/2}$ [12]. Also,, when the temperature is lower than 0 ℃, the soil may be frozen, which changes the boundary conditions and consequently the frequencies [22]. The normal changes in frequencies due to the variations in temperature should not be alarming. But the changes in frequencies due to damage can be masked by their normal changes associated with variation of temperature and other environmental conditions. In order to provide correct information for decision making regarding the stability of bridges, it is vital to distinguish between the changes in modal characteristics due to damage and those due to normal temperature fluctuations. It is very hard to measure and quantify this physical phenomenon even when all aspects have been considered. At this point in the research, it is very useful to study the correlation between frequency and temperature changes. It is certain that such knowledge about the pattern of changes in frequencies due to temperature is valuable in finding a solution to this problem. Study of environmental effects on a classical post-tensioned concrete box girder bridge with a total length of 63.4 m was presented based on a one-year monitoring period in [12].

4.1 The modal frequencies and temperatures obtained from the one-year ambient vibration data of a highway bridge

In this section, the variation of modal frequencies with respect to the changes in temperature is investigated statistically using ambient vibration data of C846 Flyover Bridge described in section 7.2. This was a much longer and larger bridge than the one pictured in [12]. The frequency domain decomposition (FDD) method was employed to

identify the modal characteristics of the bridge. It performs well for the identification of undamaged structures. For more details and references regarding FDD, refer to Chapter IV. The subspace identification algorithm will be used to obtain all modal characteristics in future studies.

Each dataset consisted of 200 seconds of acceleration measurements selected every 6 hours from February 2007 to February 2008. The recording system was down occasionally, so the data were not recorded each day, but all four seasons were represented with temperate ranges of -10.8 ℃ ~ 39 ℃ as listed in Table 5. Therefore, the data were sufficient with a large enough range of temperatures to be useful for statistical analysis.

Table 6 lists the basic statistics of the identified frequencies at times specified above, the maximum differences were 6~18%, which were close to those (14%~18%) presented in [12]. The standard deviations ranged from 0.018 Hz to 0.088 Hz for the 1st~17th frequencies and from 0.119 Hz to 0.294 Hz for the 18th~26th frequencies. This indicates that the identified results for the first 17 modes were more stable. Note that the temperatures were recorded from a weather station UT23 at the U.S. National Weather Service near the bridge; thus, their temperature records were very close to the real temperatures of the bridge, but were different from the actual temperatures where the sensors were instrumented. It is recommended to install temperature sensors near the accelerometers on bridges to record the actual temperatures of various locations on the bridge for future studies.

4.2 Using nonlinear and linear regression models to correlate the modal frequencies and temperatures

Both nonlinear and linear regression models were used to correlate the frequencies and the corresponding temperatures. Nonlinear regression is an essential statistical tool to analyze data. Gauss fit model is a non-linear least-squares fit to a function with generally four unknown parameters [23]. The Gauss fit was used in this study. A sample curve of the Gauss function is illustrated in Figure 15, in which

$$w = \frac{w_1}{\sqrt{2\ln 2}};\ y_c = y_0 + \frac{A}{w\sqrt{\pi/2}} \tag{54}$$

The Gauss fit function is

$$y = y_0 + \frac{A}{w\sqrt{\pi/2}} e^{-2\left(\frac{x-x_c}{w}\right)^2} \tag{55}$$

where y is a vector of dependent variables, which represent frequency in this study, and x is a vector of independent variables, which represent temperature in this study, y_0 means offset, x_c means center, w means width, A means area.

Some other parameters were also shown in the results. The height of the Gaussian is computed as $\frac{A}{w\sqrt{\pi/2}}$. The full width at half maximum (FWHM) of the Gaussian can me computed as $\sqrt{2\ln 2}w$. The σ represents the 1-sigma error estimates of the returned parameters and it can be computed as w/2. Adjusted R^2 is a modification of R^2 that measure the goodness-of-fit. The standard error is a method of estimation of the standard deviation of the sampling distribution associated with the estimation method [24].

Table 5. Basic statistics of the temperature corresponding to the selected data.

	Mean	Standard Deviation	Minimum	Median	Maximum
Temperature (°C)	10.19	12.25	-10.8	6.9	39

Table 6. Basic statistics of the estimated frequencies.

Mode	Mean (Hz)	Standard Deviation (Hz)	Minimum (Hz)	Median (Hz)	Maximum (Hz)	Maximum Difference (%)
1	1.14	0.018	1.08	1.14	1.18	9
2	1.34	0.031	1.25	1.34	1.40	12
3	1.48	0.018	1.41	1.48	1.52	8
4	1.58	0.023	1.53	1.58	1.69	10
5	1.75	0.029	1.70	1.75	1.85	9
6	1.93	0.029	1.86	1.93	2.00	8
7	2.24	0.054	2.00	2.26	2.32	16
8	2.40	0.030	2.32	2.40	2.47	6
9	2.71	0.064	2.50	2.71	2.90	16
10	3.06	0.057	2.90	3.07	3.20	10
11	3.30	0.040	3.20	3.30	3.40	6
12	3.48	0.039	3.40	3.48	3.59	6
13	3.83	0.082	3.60	3.84	4.00	11
14	4.20	0.080	4.01	4.20	4.49	12
15	4.75	0.083	4.57	4.74	5.00	9
16	5.18	0.088	5.00	5.20	5.39	8
17	5.57	0.071	5.40	5.57	5.80	7
18	6.25	0.158	5.82	6.25	6.89	18
19	7.42	0.208	6.91	7.38	8.00	16
20	9.51	0.161	8.80	9.55	9.84	12
21	10.71	0.119	10.32	10.72	11.13	8
22	11.64	0.269	11.20	11.64	12.30	10
23	13.07	0.205	12.57	13.09	13.71	9
24	14.40	0.214	13.81	14.40	14.99	9
25	15.64	0.294	15.00	15.63	16.50	10
26	17.19	0.268	16.50	17.21	17.99	9

Linear regression can be viewed as a special case of nonlinear regression. When the nonlinear regression analysis indicates that the data can be fitted by linear models, the

linear regression can be used for its simplicity in explanation. The equation of linear model can be written in slope-intercept form as follows:

$$y = mx + b \tag{56}$$

where y and x have the same meaning as in Eq. (55), m is the slope and, b is the y-intercept. A sample line of linear fit model is illustrated in Figure 16.

The nonlinear Gauss model was used to fit to each data set between frequency and temperature for the data gathered. The parameters of the nonlinear fit models for the typical data are listed in Table 7. It is apparently that the standard errors are low, especially for the lower order modes. So the nonlinear models fit well to the data. The correlation plots are shown in Figure 17(a), 18(a), 18(c), 19-22. Each figure contains frequency-temperature plots for one mode or two modes with similar relationship.

By analyzing the nonlinear curves, it can be deduced that generally all the curves are able to be simplified and represented by multiple lines. Most of the curves can be replaced by two lines or one line effectively. Linear regression was used to correlate the 1st, 5th, and 12th frequencies and temperatures as shown in Figures 17 (b), 18 (b) and (d). The parameters for the linear models are listed in Table 8.

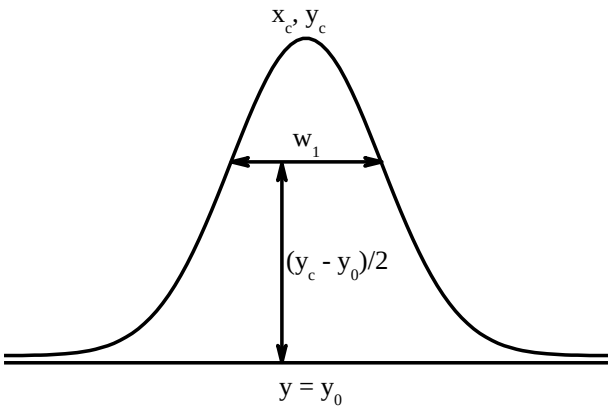

Figure 15. A sample curve of the Gauss function.

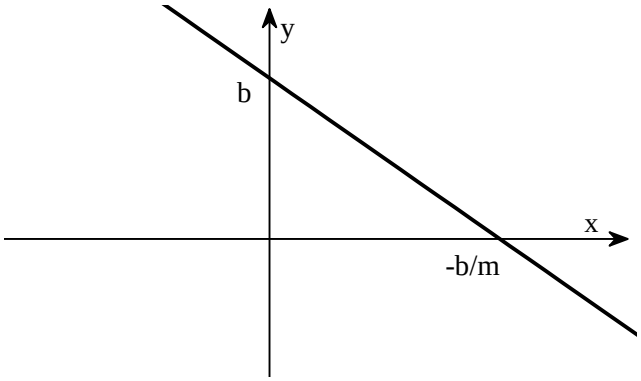

Figure 16. A sample line of linear fit model.

By comparing the adjusted R^2 values listed in Table 8 of the linear regression with those of the nonlinear regression listed in Table 7, it is seen that for the 1st line of mode 1 and the two lines of mode 5, the linear regression lines fit the data better, and for the 2nd line of mode 1 and the lines of mode 12, the nonlinear fit the data better. So it can be drawn that whether nonlinear or linear curve fitting is better depends on the data, the nonlinear regression is not always better than linear regression.

Based on the nonlinear and linear regression analysis, the relationship between frequencies and temperatures and the trends are briefly summarized in Table 9. It is clear that the trends of different modes vary. The relationship for the 1st frequency in Figure 17 is in accordance with the expectation that the lines exhibit a downward trend throughout the temperature range. This shows that the frequency increases as the temperature drops. The reason for this may be the partial fixity at the girder supports, which is caused by freezing of accumulated dust and moisture. The degree of frequency increase for partial fixity support due to freezing compared to non-frozen simple supports was evaluated using vibration theory in [22]. Another reason may be that the asphalt does not have any effect during warm times, but becomes very stiff during cold times. These factors can also explain the significant increase of frequency with decrease of temperature in Figure

18 and Figure 20. The upward trends in Figure 18 and Figure 22 may be caused by the expansion of joints due to the increase in temperature. The flat trends in Figure 19 and Figure 21 may be caused by the combination of all the factors mentioned above when they reached a balance leading to unchanged frequencies. In short, there are different effects leading to either an increase or decrease of the frequencies at specific temperature ranges. Weighting the effects of these factors for the different modal frequencies results in a unique relationship between frequency and temperature for each mode.

Further studies on this topic to obtain more accurate and extensive results are necessary for establishing statistical model of frequency-temperature relationship and discriminating changes in frequencies due to damage from those normal changes due to temperature variation.

5. Conclusion

5.1 The applications of subspace identification algorithms

This study investigated the effectiveness and applicability of the data-driven subspace identification algorithms in modal identification of bridges using output-only measurements. It was examined through a numerical truss bridge and a real concrete girder bridge. Stabilization diagrams with a range of model orders were used to determine the modal frequencies, damping ratios, and mode shapes. The stabilization diagrams with stable frequencies and damping ratios were used to determine and preserve the physical models, and eliminate the numerical modes. The mode shapes of the numerical example were presented and shown to be correct.

In the numerical example, a sinusoidal force (with a range of frequencies) was

applied to the truss. At a time when the excitation was applied, abrupt damages occurred. The responses were computed as the output measurements for identification. No noises were considered in this numerical study.

Table 7. The parameters for the nonlinear fit models for the selected modes.

		Value	Standard Error
Mode 1	Adjusted R^2	0.0811	-
	y_0	1.133	0.0007
	x_c	-8.4718	1.5281
	w	8.3935	2.0966
	A	0.2318	0.0733
	σ	4.1968	-
	FWHM	9.8826	-
	Height	0.0220	-
Mode 5	Adjusted R^2	0.0599	-
	y0	1.7642	0.0040
	xc	11.7117	0.9065
	w	18.1694	3.8814
	A	-0.5288	0.1811
	σ	9.0847	-
	FWHM	21.3928	-
	Height	-0.0232	-
Mode 12	Adjusted R^2	0.03907	-
	y0	3.4947	0.0038
	xc	9.6593	1.1095
	w	15.7049	3.6892
	A	-0.4666	0.1601
	σ	7.8524	-
	FWHM	18.4911	-
	Height	-0.0237	-
Mode 3	Adjusted R^2	0.0151	-
	y0	1.4780	0.0007
	xc	-0.5065	0.4967
	w	2.9402	1.0437
	A	0.0293	0.0102
	σ	1.4701	-
	FWHM	3.4618	-
	Height	0.0080	-

Table 7. Cont'd

		Value	Standard Error
Mode 8	Adjusted R^2	0.0222	-
	y0	2.3985	0.0012
	xc	-0.7240	0.3828
	w	2.7040	0.8039
	A	0.0568	0.0164
	σ	1.3520	-
	FWHM	3.1838	-
	Height	0.0168	-
Mode 24	Adjusted R^2	0.1365	-
	y0	14.2075	0.0935
	xc	-14.8931	17.0390
	W	50.3989	32.1611
	A	19.7915	22.0246
	σ	25.1994	-
	FWHM	59.3401	-
	Height	0.3133	-
Mode 2	Adjusted R^2	0	-
	y0	1.3281	-
	xc	4.9000	-
	W	-0.0535	-
	A	0.6530	-
	Σ	-0.0268	-
	FWHM	-0.0630	-
	Height	-9.7330	-
Mode 10	Adjusted R^2	-0.0035	-
	y0	3.0605	0.0019
	xc	65.1958	-
	w	0.2866	-
	A	0.0622	-
	σ	0.1433	-
	FWHM	0.3374	-
	Height	0.1733	-
Mode 22	Adjusted R^2	0.1999	-
	y0	11.9197	0.0708
	xc	-4.4906	3.6195
	w	37.9905	10.5332
	A	-19.1461	8.7244
	σ	18.9953	-
	FWHM	44.7304	-
	Height	-0.4021	-

Table 8. The parameters for the linear regression models for modes 1, 5, and 12.

		Value	Standard Error
Mode 1: the line before 0ºC	Adjusted R^2	0.0886	-
	Slope	-0.0025	0.0006
	Intercept	1.1353	0.0024
Mode 1: the line after 0ºC	Adjusted R^2	0.0025	-
	Slope	-0.0001	0.0001
	Intercept	1.1348	0.0010
Mode 5: the line before 12ºC	Adjusted R^2	0.0609	-
	Slope	-0.0014	0.0002
	Intercept	1.7541	0.0013
Mode 5: the line after 12ºC	Adjusted R^2	0.0629	-
	Slope	0.0009	0.0002
	Intercept	1.7303	0.0049
Mode 12: the line after 12ºC	Adjusted R^2	0.0070	-
	Slope	-0.0007	0.0003
	Intercept	3.4817	0.0018
Mode 12: the line after 12ºC	Adjusted R^2	0.0647	-
	Slope	0.0014	0.0003
	Intercept	3.4524	0.0078

The frequencies and damping ratios of the truss before damage and after damage were obtained from the stabilization diagrams. It was observed that the uncertainties were exceptionally low. There were two spurious modes in the stabilization diagrams for damping ratios. The identified frequencies and damping ratios corresponded well with the exact values. For the frequencies before damage, the error of 1st modal frequency was only 0.16%, and most other frequencies had an error of less than 4%. For the frequencies after damage, the identified errors of frequencies were also low. For both cases of before damage and after damage, only five modal damping ratios were identified, but the identified values were accurate with errors less than 2.5%. The algorithm also showed its

ability to identify the closely spaced modes, e.g., modes 5 and 6 of the truss before damage was detected. The SSI method obtained the mode shapes information. The 1st mode shapes of the truss bridge before and after damage were investigated and found to be able to indicate the damage.

It must be noted that if the excitation is white noise instead of the sinusoidal force, all the modes can be excited and identified, and therefore the identified modal characteristics should be more accurate.

As for the application of actual vibration measurements, the algorithm was used in modal identification of a concrete highway bridge. The monitoring system consisted of 18 accelerometers installed on the bridge to measure the transverse, longitudinal, and vertical accelerations.

In the stabilization diagrams, the frequencies identified from the real measurements were also very clear, while they are not as certain as those obtained from the numerical example. The damping ratios were even more uncertain than the frequencies, and they were certain within the range of 2~3%. Many spurious modes were generated and they are eliminated based on the criteria for the stabilization diagrams. The identified frequencies were compared with those from forced vibration tests. The errors of the first 18 frequencies were between 0.12% and 5%, this shows that the SSI can estimate frequencies very well for real measurements. The SSI also obtained reasonable damping ratios for the bridges.

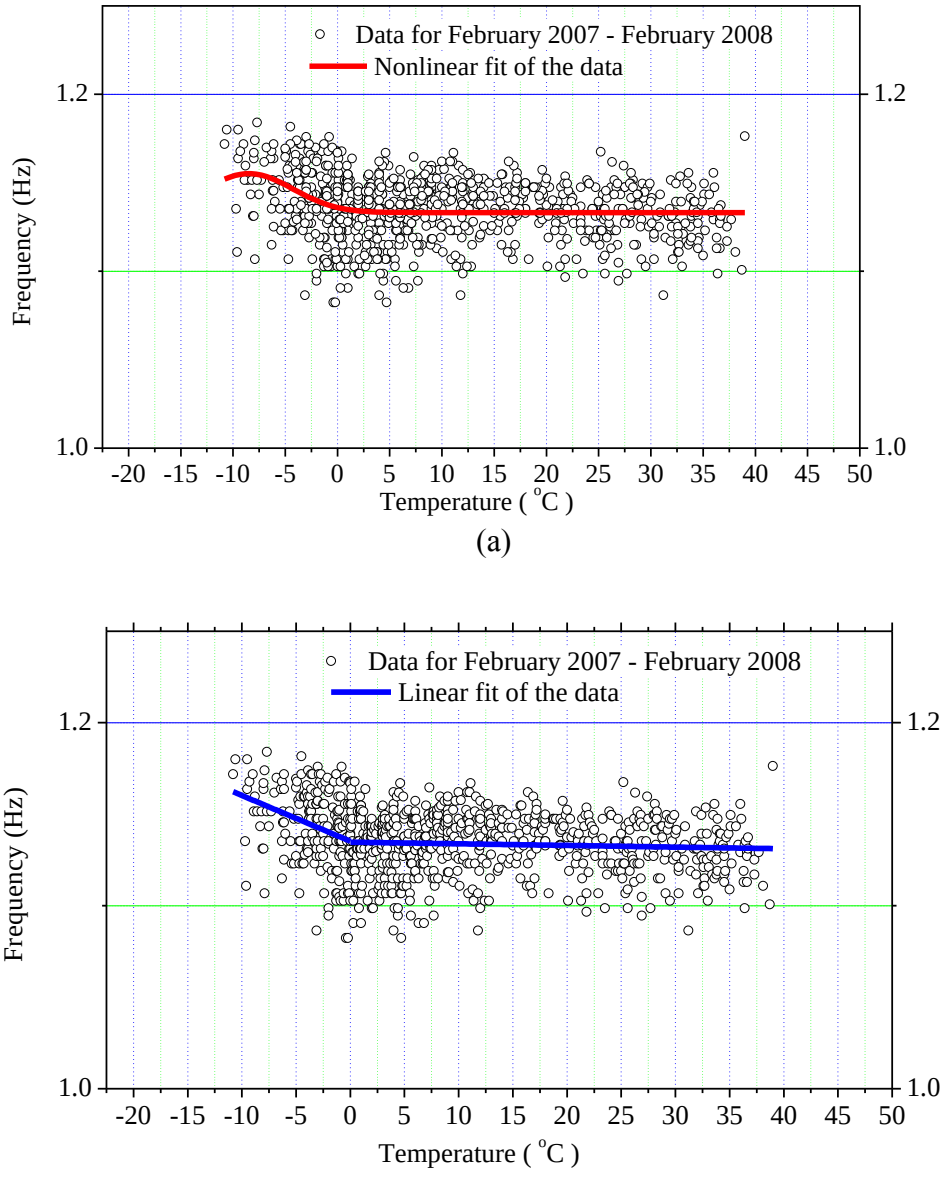

Figure 17. Modal frequency vs. temperature for the 1st frequency, and the data fitting: (a) nonlinear fit model; (b) linear fit model.

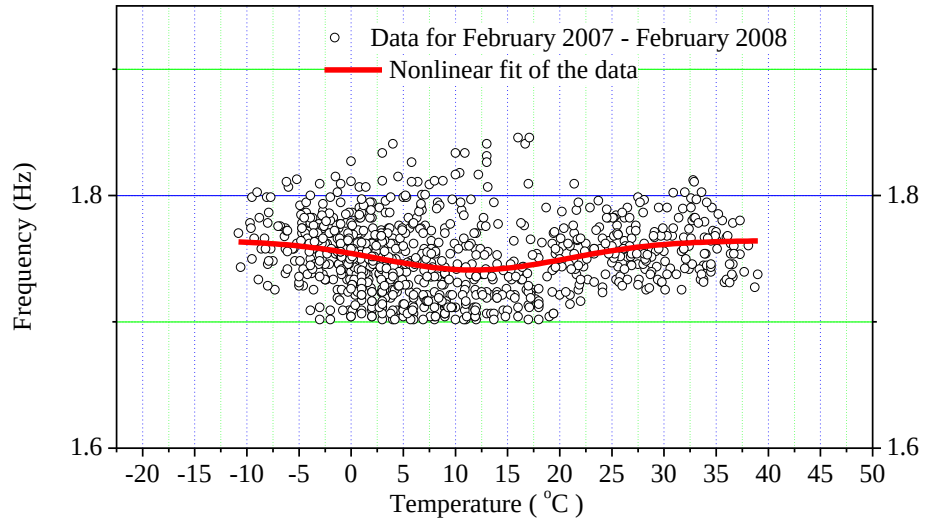

(a)

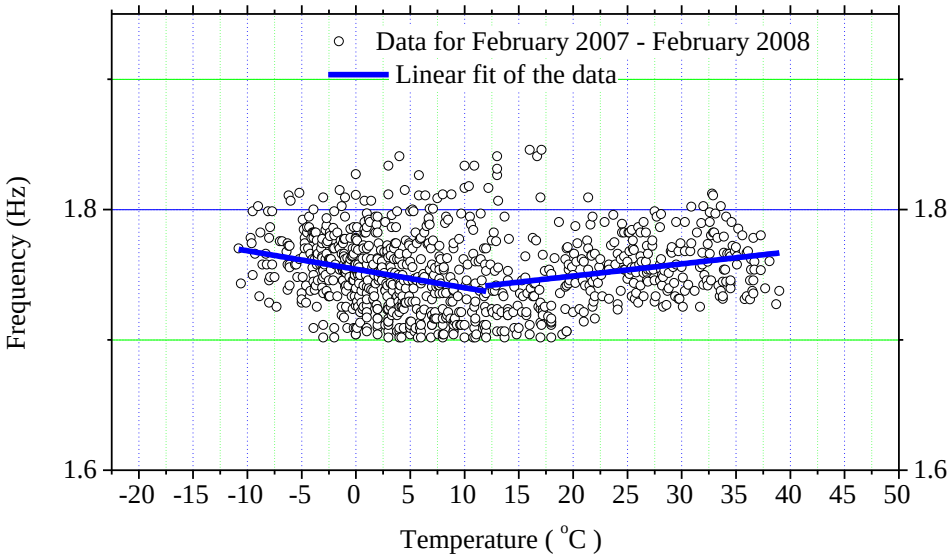

(b)

Figure 18. Modal frequency vs. temperature for the 5th and 12th frequencies, and the data fitting: (a) nonlinear fit model for the 5th frequency; (b) linear fit model for the 5th frequency; (c) nonlinear fit model for the 12th frequency; (d) linear fit model for the 12th frequency.

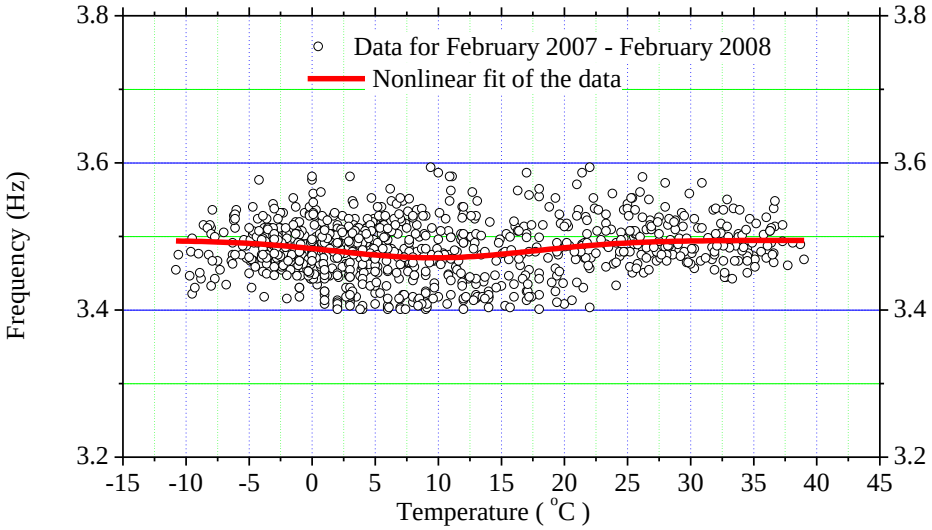

(c)

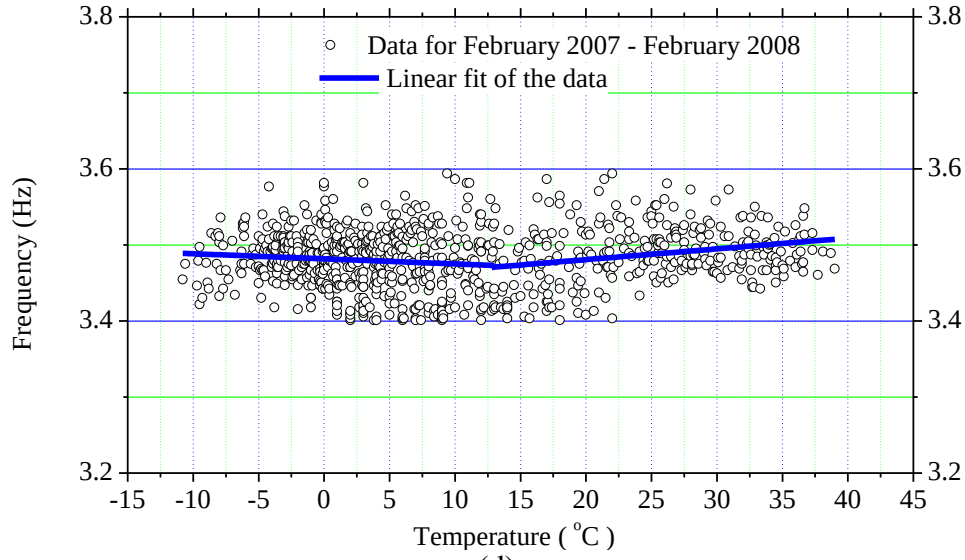

(d)

Figure 18. Cont'd

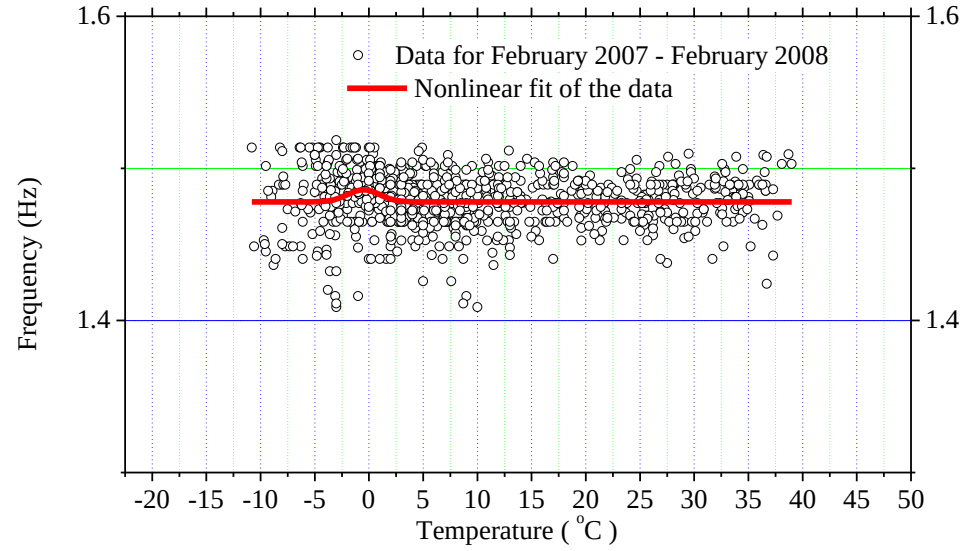

(a)

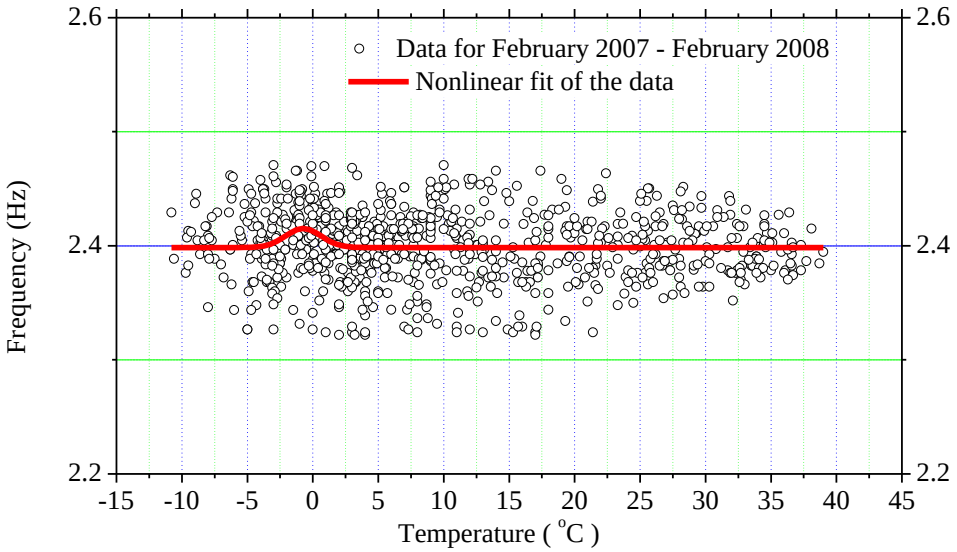

(b)

Figure 19. Modal frequency vs. temperature for the 3rd and 8th frequencies, and the nonlinear fit models: (a) nonlinear fit model for the 3rd frequency; (b) nonlinear fit model for the 8th frequency.

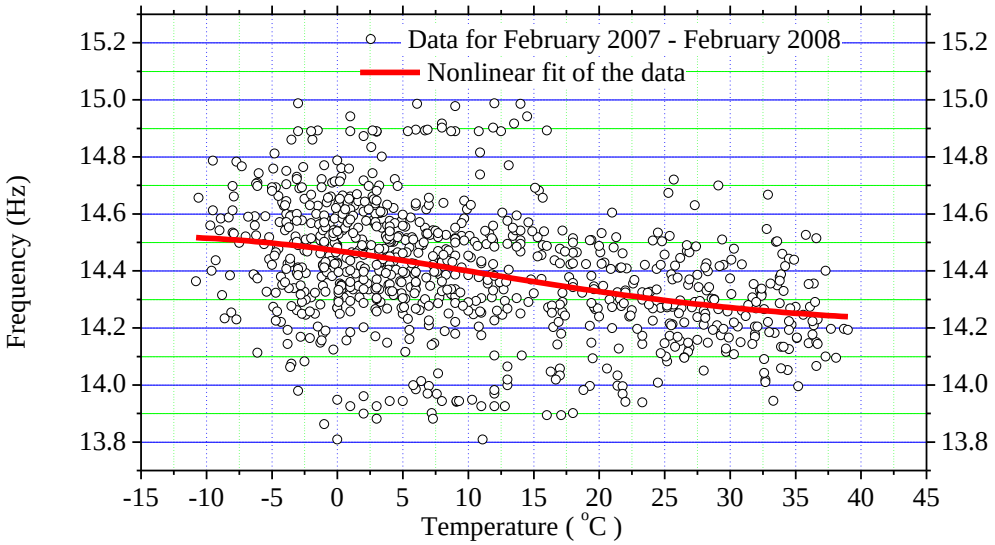

Figure 20. Modal frequency vs. temperature for the 24th frequency, and the nonlinear fit model.

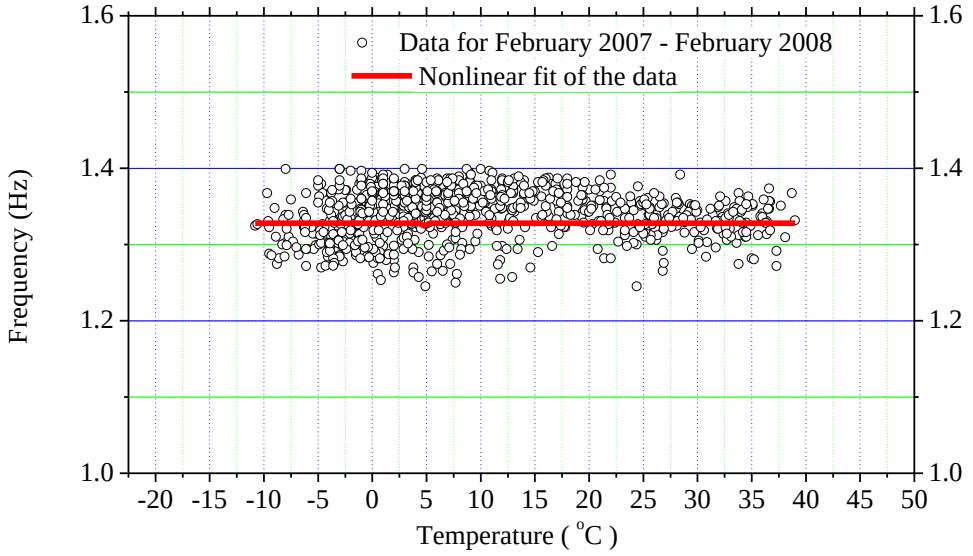

(a)

Figure 21. Modal frequency vs. temperature for the 2nd and 10th frequencies, and the nonlinear fit models: (a) nonlinear fit model for the 2nd frequency; (b) linear fit model for the 10th frequency.

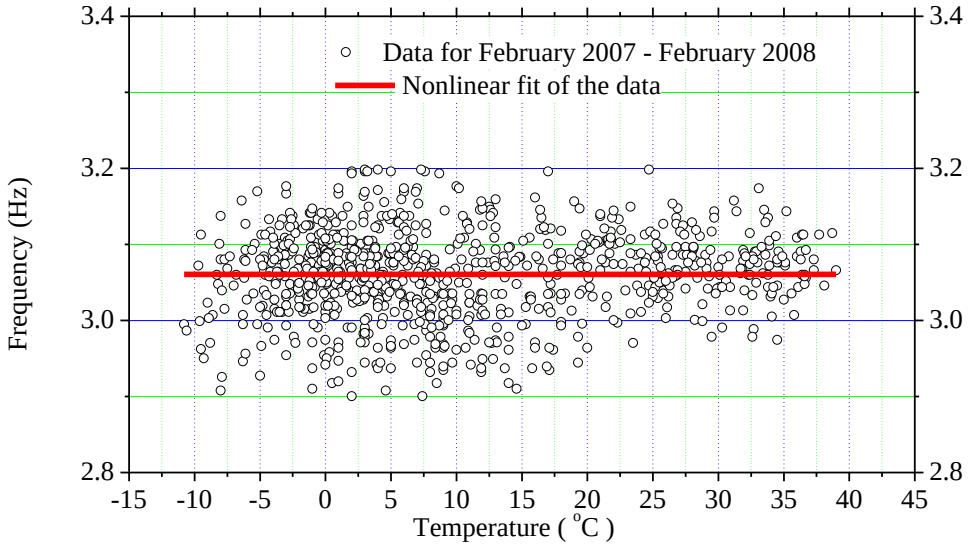

(b)

Figure 21. Cont'd.

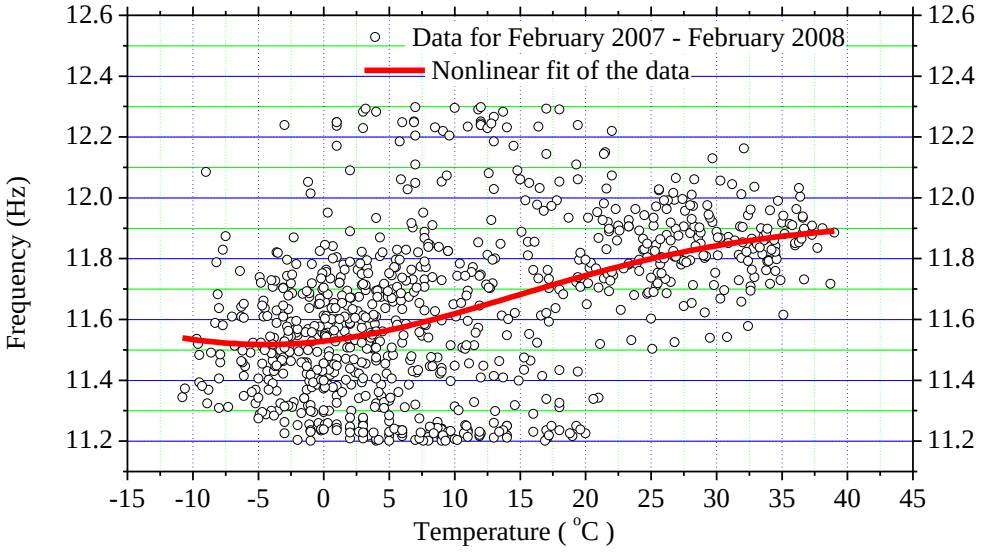

Figure 22. Modal frequency vs. temperature for the 22nd frequency, and the nonlinear fit model.

Table 9. Summary of the trends of modal frequency vs. temperature

Figure 17. Modal frequency vs. temperature for the 1st frequency, and the data fitting	2 lines intersect at 0 ℃: both with a downward trend. The slope is larger before 0 ℃.
Figure 18. Modal frequency vs. temperature for the 5th and 12th frequencies, and the data fitting.	2 lines intersecting at10 ℃; Downward trend before 10 ℃, upward trend after 10 ℃.
Figure 19. Modal frequency vs. temperature for the 3rd and 8th frequencies, and the nonlinear fit model.	1 line with constant 0 slope, but with abrupt upward and downward around 0 ℃.
Figure 20. Modal frequency vs. temperature for the 24th frequency, and the nonlinear fit model.	1 line with downward trend.
Figure 21. Modal frequency vs. temperature for the 2nd and 10th frequencies, and the nonlinear fit models.	1 line with flat trend.
Figure 22. Modal frequency vs. temperature for the 22nd frequency, and the nonlinear fit model.	1 line with upward trend. 9th has a small slope, and 22nd has a large slope after 0 ℃.

N4SID is one of the subspace identification algorithms that can be used for both output-only and input-output systems. This study examined the effectiveness of N4SID in modal identification of the C846 highway bridge using ambient vibration measurements. The frequencies, mode shapes, and damping ratios were able to be determined. The frequencies obtained from the stabilization diagram corresponded with the values from the force vibration tests with differences of 0.16%~7.59%. It was observed from the stabilization diagrams that N4SID needs a much larger order than its theoretical value. When the system order number increases, the computation time also increases significantly, therefore, this algorithm is not recommended for large systems before significant improvement of its performance.

The mode shapes need further analysis. A denser layout of sensors on the highway bridge is needed to obtain complete mode shapes. The information for the mode shapes

based on the modal assurance criteria can be included in the stabilization diagrams. The final objective is to incorporate the subspace-based identification algorithms with the stabilization diagrams into the real-time bridge health monitoring system.

5.2 Statistical analysis of the influence of temperature on frequencies

A statistical analysis was conducted to study the influence of temperature on the dynamic properties of the C846 concrete highway bridge by using one-year ambient vibration data with a temperature range of -10.8 ℃ ~ 39 ℃. The difference between minimum and maximum identified frequencies ranged from 6% to 12% for the first 15 modes.

The modal frequencies and temperatures were correlated by nonlinear and linear regression curve fitting, which demonstrated that correlations for most modes can be represented by a single or a bilinear line. Downward, upward, and flat trends of the frequencies at specific temperature ranges were exhibited at different modes. For example, at the fundamental mode, both lines show a downward trend, and the line had a bigger slope when the temperature was below 0 ℃, that means the frequency increased with a decrease in temperature. This can be explained as: a) the decrease of Young's moduli of concrete and asphalt with the increase of temperature resulting in a decrease of frequencies; b) when the temperature drops below 0 ℃, the frozen accumulated dust and moisture may cause partial fixity at the girder supports that can lead to the increase of frequencies; c) the asphalt may not be affected during the warm times and contribute negligible stiffness, but become very stiff during cold times; d) some higher modes exhibited upward trends, which may be caused by the expansion of joints. In a word,

different weights of these effects on each modal frequency resulted in unique correlations for each mode.

The variations of damping ratios and mode shapes need to be investigated in future studies. Also, temperature sensors are recommended to be installed on the bridge to provide exact temperatures.

REFERENCES

[1] B. Peeters, C.E. Ventura, Comparative study of modal analysis techniques for bridge dynamic characteristics, *Mechanical Systems and Signal Processing* 17 (2003) 965-988.

[2] R. Brincker, L. Zhang, P. Andersen, Modal identification from ambient responses using frequency domain decomposition, *Proceedings of the 18th International Modal Analysis Conference,* San Antonio, TX, 2000, 625-630.

[3] P. Van Overschee, B. De Moor, Subspace algorithms for the stochastic identification problem, *Automatica* 29 (1993) 649-660.

[4] P. Van Overschee, B. De Moor, *Subspace Identification for Linear Systems: Theory, Implementation, Applications,* Kluwer Academic Publishers, Dordrecht, 1996.

[5] M. Viberg, B. Wahlberg, B. Ottersten, Analysis of state space system identification methods based on instrumental variables and subspace fitting, *Automatica* 33 (1997) 1603-1616.

[6] P. Van Overschee, B. De Moor, N4SID: subspace algorithms for the identification of combined deterministic-stochastic systems, *Automatica* 30 (1994) 75-93.

[7] M. Abdelghani, M. Verhaegen, P. Van Overschee, B. De Moor, Comparison study of subspace identification methods applied to flexible structures, *Mechanical Systems and Signal Processing* 12 (1998) 679-692.

[8] C.T. Chen, *Linear System Theory and Design*, third ed., Oxford University Press, USA, New York, 1999.

[9] J.-N. Juang, *Applied System Identification*, PTR Prentice-Hall, Englewood Cliffts, NJ, 1994.

[10] B. Peeters, G. De Roeck, Reference-based stochastic subspace identification for output-only modal analysis, *Mechanical Systems and Signal Processing* 13 (1999) 855-878.

[11] B. Peeters, G. Lowet, H.V.D. Auweraer, J. Leuridan, A new procedure for modal parameter estimation, *Sound and Vibration* 38 (2004) 24-29.

[12] B. Peeters, G.D. Roeck, One-year monitoring of the Z24-Bridge: environmental effects versus damage events, *Earthquake Engineering & Structural Dynamics* 30 (2001) 149-171.

[13] M. Scionti, J.P. Lanslots, Stabilisation diagrams: pole identification using fuzzy clustering techniques, *Advances in Engineering Software* 36 768-779.

[14] H. Van der Auweraer, P. Guillaume, P. Verboven, S. Vanlanduit, Application of a fast-stabilizing frequency domain parameter estimation method, *Journal of Dynamic Systems, Measurement, and Control* 123 (2001) 651-658.

[15] J. Chen, J. Li, Simultaneous identification of structural parameters and input time history from output-only measurements, *Computational Mechanics* 33 (2004) 365-374.

[16] M.W. Halling, T. Petty, Strong motion instrumentation of I-15 bridge C-846, UDOT Report No. UT-01.12, 2001.

[17] T.M. Dye, Forced and ambient vibration testing of a permanently instrumented full-scale bridge, Department of Civil and Envirionmental Engineering, Utah State University,

Logan, 2002.

[18] M.J.N. Priestley, F. Seible, G.M. Calvi., *Seismic design and retrofit of bridges*, John Wiley and Sons, Inc, 1996.

[19] D. Skolnik, Y. Lei, E. Yu, J.W. Wallace, Identification, model updating, and response prediction of an instrumented 15-story steel-frame building, *Earthquake Spectra* 22 (2006) 781-802.

[20] L. Ljung, *System Identification: Theory for the User*, second ed., Prentice Hall PTR, Upper Saddle River, NJ, 1999.

[21] K.F. Alvin, K.C. Park, Second-order structural identification procedure via state-space-based system identification, *AIAA JOURNAL* 32 (1994) 397-406.

[22] S. Alampalli, Influence of in-service environment on modal parameters 16th International Modal Analysis Conference, Santa Barbara, CA, USA, 1998, pp. 111-116.

[23] http://www.ucl.ac.uk/~ucaptss/work/technical/gaussfit/index.html.

[24] B.S. Everitt, A. Skrondal, *The Cambridge Dictionary of Statistics*, fourth ed., Cambridge University Press, 2010.

CHAPTER III

DAMAGE IDENTIFICATION OF SUBSTRUCTURES BY USING ADAPTIVE KALMAN FILTER AND WAVELET TRANSFORM

ABSTRACT

Substructure identification is a method to address the numerical difficulty and insufficient sensors involved in structural identification of a large system. This method divides the structure into many small substructures and identifies them separately. Various structural identification algorithms have been applied in substructure identification that includes the extended Kalman filter, which has been used for identifying constant structural parameters. This study proposes to use the adaptive Kalman filter to identify varying properties of substructures. To investigate the effectiveness of the substructure identification by using adaptive Kalman filter, numerical studies were performed on a shear building, a plane frame, and a plane truss bridge. It was demonstrated that the stiffness and damping of substructures can be identified successfully from the limited acceleration responses and abrupt changes of these properties can be identified as well. Wavelet analysis was also proposed for damage detection of substructures and applied to the frame structure to show the ability of scalograms of acceleration responses in detecting and approximately locating changes of structural properties or damages. These studies can be very useful for structural health monitoring and structural model updating.

1. Review of the Applications of Substructural Approach

For structural health monitoring of large structures, it is impractical to obtain

complete measurements due to the limited number of sensors and the difficulty of conducting field tests. In addition, it is inconvenient to identify a large number of unknown parameters in a full system because of numerical difficulty in convergence and accuracy [1]. Adopting the strategy of "divide-and-conquer," substructural identification is formulated to address this issue and assess localized damage. The purpose is to reduce a seemingly insurmountable problem into many smaller problems of manageable size, thereby improving numerical convergence and accuracy [2-3]. The effect of excitation can be expressed in terms of the responses at the interfaces, and therefore substructural identification may be carried out without measuring the actual input excitation to the structure [4].

Efforts have been made to develop methods to eliminate the need for interface measurements and thus to reduce the computational costs. Koh and Shankar [2] proposed a method for parameter identification of substructures without the interface measurements. Tee et al. [1] presented a novel substructure strategy involving model condensation for stiffness matrix identification and damage assessment with incomplete measurement. Likewise, Sandesh [5] and Shankar presented a method that requires only the acceleration measurement at the interior DOFs of the substructure. In [6], the equations of motion of the complete system were derived and the dimension was reduced considerably. In [7-8], the procedures of a dynamic stiffness method that reduce the global matrix dimension were proposed and improved. Weng et al. [9] proposed the modal truncation approximation in a substructuring method that only needs to calculate the lowest eigensolutions of the substructures.

The substructural identification has been used to determine the localized structural

damage. Park et al. [10], Sandesh and Shankar [5], and Skjaeraek et al. [11] also investigated methods for damage localization of structures. Okuma et al. [12], and Su and Juang [13] explored the possibility of performing system identification at the substructural level and then synthesizing the results to obtain an analysis model for the assembled structure.

The probabilistic approaches have been studied in [14-16] for substructure identification, by which the probability of different damage levels in each substructure can be computed.

To identify the dynamic properties of substructures, various system identification algorithms have been employed and discussed in the literature. Oreta and Tanabe [17] and Koh et al. [18] used the extended Kalman filter (EKF) with a weighted global iteration algorithm to formulate and solve state and observation equations. Tee et al. [19] employed the eigensystem realization algorithm (ERA) and the observer/Kalman filter identification (OKID). Huang and Yang [20] employed an adaptive damage tracking technique, the sequential nonlinear least-square estimation to identify damage to a complex structure. Bakhary et al. [21], Wu et al. [22], Xu [23], and Yun et al. [24] used the neural networks for identification. Rothwell et al. [25] used a short-time Fourier transform with an adaptive window width to analyze the transient response of radar targets. Koh et al. [3] used a non-classical approach of genetic algorithms. Ma and Vakakis [26] performed system identification of the dynamics using Karhunen-Loeve (K-L) decomposition. Yun and Lee [4] derived an autoregressive moving average with a stochastic input (ARMAX) model for a substructure to process the noise-polluted measurement data.

The substructural identification methods have been applied to damage identification of numerous types of structures. Some of the applications are briefly summarized here. The numerical/experimental studies using substructural identification methods were performed for shear buildings in [1, 3, 5, 15, 18, 23] and other lumped mass systems under different excitations [27]. The localized substructure identification of a shear building involving soil-structure interaction effects was presented in [28]. Substructuring approaches were applied for the parameterization of multi-story buildings in [10, 15-16]. The applicability and effectiveness of substructure identification methods in beam structures were investigated in [7-8, 29-31]. The substructure approaches were employed in estimating and tracking the stiffness and damping of truss structures [4, 18, 20, 26, 32]. The use of the substructure methods to identify dynamic properties of plane frame structures were presented in [17-18, 27], and the use for multi-storey frames were studied in [1, 9, 12, 19, 21, 33]. The effectiveness of substructure approaches in plates and continuous concrete slabs were addressed in [34] and [21], respectively. The identification of linear and non-linear joint properties involving substructure methods can be found in [31, 34-38]. It was stated in [39] that in engineering dynamics, substructuring technique was first choice in solving large numerical systems and performing experimental analyses on large structures, and the technique has been applied to both civil and mechanical structures.

The above literature review shows that the methodology of substructure was able to locate and quantify damage accurately for various types of structures from incomplete dynamic measurements by using different damage identification algorithms.

2. Objective of this Study

The purpose of this study is to investigate the effectiveness of substructural identification of shear building, truss bridge and frame structure with abrupt degradation in stiffness and damping. The extended Kalman filter was used to identify dynamic properties and detect damage. Furthermore, the effectiveness of wavelets in damage detection of substructures was also investigated. The vibration-based damage identification by wavelet transform has been used for frame structures [40], beams and plates [41-42], and it has been studied extensively in the literature. The motivation for using wavelets in substructure identification is to provide immediate useful information for decision-making regarding maintenance of the structures based on damage assessment using wavelet analysis of the measurements from sparsely deployed sensors.

3. Formulation of Substructure

Without loss of generality, a linear elastic plane frame structure was used to illustrate the formulation of substructure identification. Figure 23 illustrates the frame and a substructure of it. The equation of motion of the entire structure can be expressed as

$$M(t)\ddot{U}(t) + C(t)\dot{U}(t) + K(t)U(t) = F(t) \tag{57}$$

where M, C, K are the mass, damping and stiffness matrices of the entire structure, respectively, U is the displacement vector, the dot (·) denotes derivative respect to time, and F is the external excitation on the structures and can represent force or motion.

The equation of motion for the substructure can be extracted from the partitioned matrices of Eq. (57) as

$$\begin{bmatrix} M_{rr} & M_{rs} & O \\ M_{sr} & M_{ss} & M_{sd} \\ O & M_{ds} & M_{dd} \end{bmatrix} \begin{Bmatrix} \ddot{u}_r \\ \ddot{u}_s \\ \ddot{u}_d \end{Bmatrix} + \begin{bmatrix} C_{rr} & C_{rs} & O \\ C_{sr} & C_{ss} & C_{sd} \\ O & C_{ds} & C_{dd} \end{bmatrix} \begin{Bmatrix} \dot{u}_r \\ \dot{u}_s \\ \dot{u}_d \end{Bmatrix} + \begin{bmatrix} K_{rr} & K_{rs} & O \\ K_{sr} & K_{ss} & K_{sd} \\ O & K_{ds} & K_{dd} \end{bmatrix} \begin{Bmatrix} u_r \\ u_s \\ u_d \end{Bmatrix} = \begin{Bmatrix} F_r \\ F_s \\ F_d \end{Bmatrix} \quad (58)$$

where U is replaced by u to denote displacement of substructures, O is zero block matrix, subscript ‘s’ denotes internal DOFs of the substructure, subscripts ‘r’ and ‘d’ denote interface DOFs between the substructure and its neighboring structures, subscripts ‘R’ and ‘D’ denote the neighboring substructures shown in Figure 23(a).

To identify the structural parameters within the substructure, the second block matrix of Eq. (58) is taken to formulate a state equation as follows:

$$\begin{aligned} M_{ss}\ddot{u}_s(t) + C_{ss}\dot{u}_s(t) + K_{ss}u_s(t) = F_s(t) - M_{sr}\ddot{u}_r(t) - M_{sd}\ddot{u}_d(t) - C_{sr}\dot{u}_r(t) \\ - C_{sd}\dot{u}_d(t) - K_{sr}u_r(t) - K_{sd}u_d(t) \end{aligned} \quad (59)$$

The right hand side of Eq. (59) is treated as an input excitation to the substructure, the u_s, $\dot{u}_s$, and $\ddot{u}_s$ are output responses.

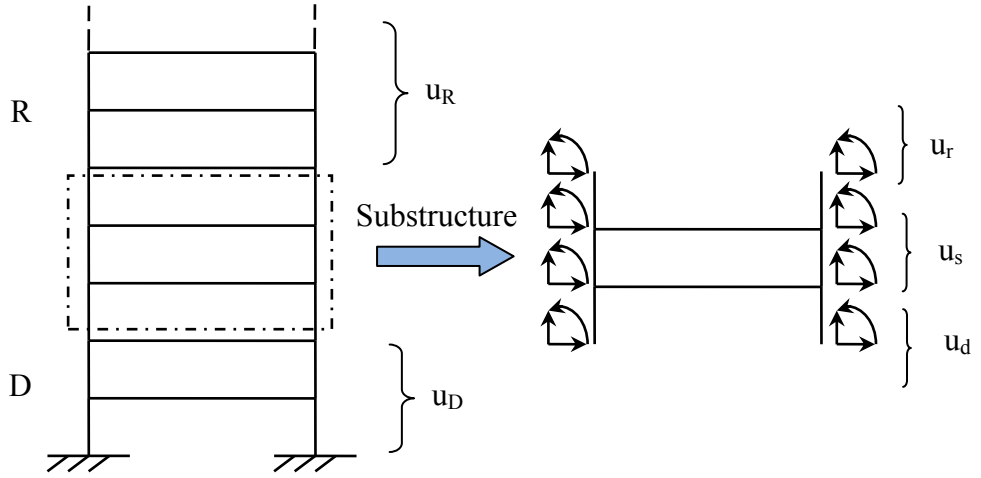

Figure 23. Illustration of substructure: (a) Frame structure (b) A Substructure of the frame structure.

The displacement, velocity and acceleration responses of all degrees of freedom within the substructure and at the interfaces of the substructure can be used for structural identification. In the structural identification by the adaptive Kalman filter algorithm in this study, not all these measurements are required.

The following state vectors are introduced into the state equation as

$$X_1 = \begin{bmatrix} u_{s,1} & u_{s,2} & \cdots & u_{s,n} \end{bmatrix}^T ; X_2 = \begin{bmatrix} \dot{u}_{s,1} & \dot{u}_{s,2} & \cdots & \dot{u}_{s,n} \end{bmatrix}^T ; X_3 = \begin{bmatrix} \theta_1 & \theta_2 & \cdots & \theta_m \end{bmatrix}^T \quad (60)$$

where X_1 is the state for displacements, X_2 is the state for velocities, the array X_3 contains the unknown parameters to be determined, such as those in the M, C and K matrices. For convenience, more vectors, such as X_4, can be added for more unknown parameters. The state-space equations of the system may be expressed as

$$\frac{d}{dt}\begin{Bmatrix} X_1 \\ X_2 \\ X_3 \end{Bmatrix} = \begin{Bmatrix} X_2 \\ -M_{ss}^{-1}(X_3)[C_{ss}(X_3)X_2 + K_{ss}(X_3)X_1 + F_{sr}(t) + F_{sd}(t) + F_s(t)] \\ 0 \end{Bmatrix} \quad (61)$$

where

$$F_{sr}(t) = M_{sr}(X_3)\ddot{u}_r(t) + C_{sr}(X_3)\dot{u}_r(t) + K_{sr}(X_3)u_r(t)$$

$$F_{sd}(t) = M_{sd}(X_3)\ddot{u}_d(t) + C_{sd}(X_3)\dot{u}_d(t) + K_{sd}(X_3)u_d(t)$$

The observation (measurement) equation is written as

$$Y(k) = H(k)X(k) + v(k) \quad (62)$$

where Y(k) is the discrete observation vector that contains the measurements, H(k) is the observation (measurement) matrix, v(k) is the noise vector with covariance R, k denotes time t_k. Since acceleration is the most frequently used on-line dynamic response measurement, acceleration signals were investigated for structural identification in this study.

Depending on whether overlapping reference measurements (sensors) were used or not, the application of the substructural identification procedure usually can be classified in one of two ways, namely identification with or without a reference measurement. In addition to the two common ways, Koh et al. [3] also developed a new substructural procedure, the so-called progressive substructural identification. The different identification forms are illustrated in Figure 24, among which, Figure 24 (a) shows the form without reference measurements, by which no overlap exists between adjacent substructures, Figure 24 (b) shows the form with overlapping reference measurements, and Figure 24 (c) shows a progressive form developed by Koh et al. [3].

Substructure identification without overlapping references needs the interface responses as input excitation to the substructure. Since interface masses are not included, they cannot be identified. This method converges fast and it does not have the problem of error propagation. Since interface response can be computed from a previous identified substructure and be used in the identification of subsequent substructure, substructure identification with overlap requires less response measurements. But the substructure identification with overlap has the problem of error propagation and accumulation, and it converges slower. Because all masses are included in the substructures, identification of all the unknown masses is theoretically achievable.

The progressively substructural identification proposed in [3] is an alternative method. It takes advantage of all the available measurements by progressively extending substructures with few unknowns at each stage. It identifies the unknown masses very well. However, the computational cost is increased for this method.

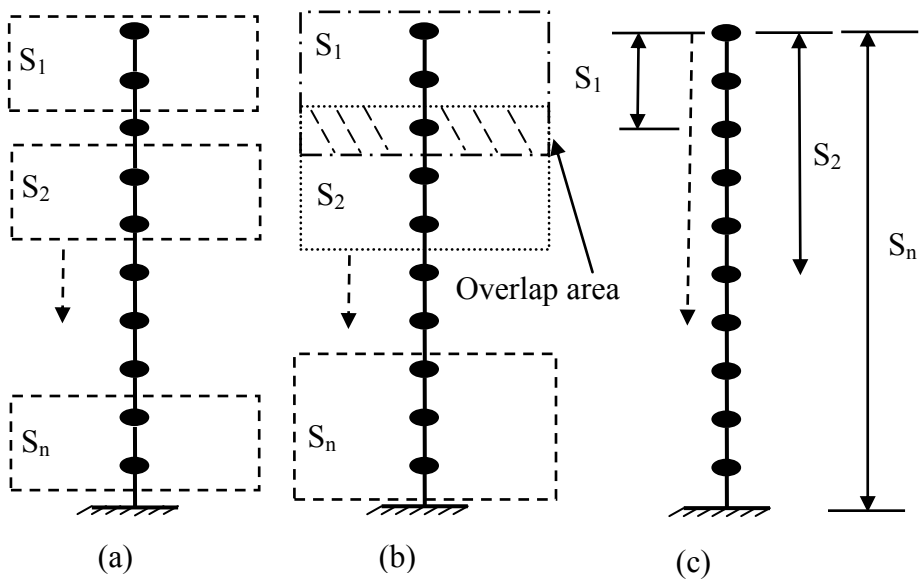

Figure 24. Illustration of substructural approaches: (a) Substructural identification w/o overlapping references; (b) Substructural identification with overlapping references; (c) Progressive substructural identification.

This study focused on investigating the effectiveness of the adaptive Kalman filter and wavelets on substructure identification, the identification without overlapping reference measurements was used.

Accelerometer is a reliable and most frequently used sensor for structural health monitoring. It is essential to develop methods that can identify substructure using only acceleration response. The Eq. (59) may be rewritten as

$$M_{ss}\ddot{u}_s(t)+C_{ss}\dot{u}_s(t)+K_{ss}u_s(t)=F_s(t)-M_{sc}\ddot{u}_c(t)-C_{sc}\dot{u}_c(t)-K_{sc}u_c(t) \tag{63}$$

where subscript "c" is use to denote all the interface degrees of freedom, which are represented by "r" and "d" in Eq. (59).

To remove the input displacement and velocity on the right-hand-side of Eq. (63), Koh et al. [3] proposed that the displacements of internal degrees of freedom can be represented by the sum of a “quasi-static displacement” and a relative displacement, which can be expressed as

$$u_s(t) = u_s^s(t) + u_s^r(t) \tag{64}$$

where $u_s^s(t)$ is 'quasi-static displacement' and $u_s^r(t)$ is 'relative displacement'. Suppose the external excitation and the time-derivative terms Eq. (63) to be zero, it yields

$$u_s^s(t) = -K_{ss}^{-1}K_{sc}u_c = \eta u_c \tag{65}$$

where η is the influence matrix to correlate the interface DOFs to internal DOFs of the substructure. Substitute equations (64) and (65) into (63), it yields

$$M_{ss}\ddot{u}_s^r(t) + C_{ss}\dot{u}_s^r(t) + K_{ss}u_s^r(t) = F_s(t) - (M_{sc} + M_{ss}\eta)\ddot{u}_c(t) - (C_{sc} + C_{ss})\dot{u}_c(t) \tag{66}$$

Damping force is usually a very small value compared to the inertial force, so the damping force may be ignored and Eq. (66) becomes

$$M_{ss}\ddot{u}_s^r(t) + C_{ss}\dot{u}_s^r(t) + K_{ss}u_s^r(t) = F_s(t) - (M_{sc} + M_{ss}\eta)\ddot{u}_c(t) \tag{67}$$

If M represents a lumped mass system, then M is a diagonal matrix and M_{sc} vanishes, then equation (67) becomes

$$M_{ss}\ddot{u}_s^r(t) + C_{ss}\dot{u}_s^r(t) + K_{ss}u_s^r(t) = F_s(t) - M_{ss}\eta\ddot{u}_c(t) \tag{68}$$

If the substructure has free ends, then the influence matrix $\eta = [1\ \ 1...1]^T$, and if there is no external excitation on the substructure, the governing equation of motion becomes simplified to an output only system,

$$M_{ss}\ddot{u}_s^r(t) + C_{ss}\dot{u}_s^r(t) + K_{ss}u_s^r(t) = -M_{ss}[1\ \ 1...1]^T\ddot{u}_c(t) \tag{69}$$

4. Brief Review of Kalman Filter Algorithms

A Kalman filter is an optimal recursive data processing algorithm that can estimate the past, present, and future states of process even if the modeled system is not completely known. It is widely used, for example, in the area of autonomous or assisted

navigation [43], and it has been used in structural identification in recent years [19, 44-46].

This section gives a brief summary of the Kalman filter, extended Kalman filter, and adaptive Kalman filter. The adaptive Kalman filter algorithm is used in the substructural identification of the three numerical examples.

4.1 Kalman filter algorithm

The general computations involved in the Kalman filter are outlined in this subsection. More extensive references include [43, 47-49].

The discrete line dynamic system is governed by the vector difference equation

$$x_k = \Phi(k,k-1)x_{k-1} + B_{k-1}u_{k-1} + w_{k-1} \tag{70}$$

with the discrete observation

$$y_k = H_k x_k + \nu_k \tag{71}$$

where x_k is the state vector at t_k, $\Phi(k,k-1)$ is the nonsingular state transition matrix (from t_{k-1} to t_k), u_k is the optional control input, B_k is the matrix that relates the input u to the state x, y_k is the observation (measurement) at t_k, H_k is the observation matrix, w_k and ν_k represent the system and measurement noises, respectively. It is assumed w_k and ν_k are white Gaussian sequences and independent of each other with

$$E(w_{k-1}) = 0; \qquad E(w_{k-1}w_{l-1}^T) = Q_k\delta_{kl}; \qquad w_{k-1} \sim N(0, Q_{k-1})$$

$$E(\nu_k) = 0; \qquad E(\nu_k\nu_l^T) = R_k\delta_{kl}; R_k > 0; \qquad \nu_k \sim N(0, R_k)$$

where δ_{kl} is the Kronecker delta.

Generally, the Kalman filtering consists of two procedures: the prediction (time update) and updating (measurement update). The predicted state estimate and the

improved estimate via updating are termed the a priori and a posteriori, respectively. The main equations are

Prediction

$$\hat{x}_{k|k-1} = \Phi(k,k-1)\hat{x}_{k-1|k-1} + B_{k-1}u_{k-1} \tag{72}$$

$$P_{k|k-1} = \Phi(k,k-1)P_{k-1|k-1}\Phi^T(k,k-1) + Q_{k-1} \tag{73}$$

Updating

$$K_k = P_{k|k-1}H_k^T[H_kP_{k|k-1}H_k^T + R_k]^{-1} \tag{74}$$

$$\hat{x}_{k|k} = \hat{x}_{k|k-1} + K_k[y_k - H_k\hat{x}_{k|k-1}] \tag{75}$$

$$P_{k|k} = (I - K_kH_k)P_{k|k-1} \tag{76}$$

where $\hat{x}_{k|k}$ denotes state estimate at t_k given y_k, $P_{k|k-1}$ denotes a covariance matrix of the error in $\hat{x}_{k|k-1}$, namely $P_{k|k-1} = E\{(x_k - \hat{x}_{k|k-1})(x_k - \hat{x}_{k|k-1})^T \mid y_k\}$, K_k is the Kalman gain matrix at t_k.

After each prediction and updating pair, the process is repeated with the previous a posteriori estimates used to predict the new a priori estimates. It must be noted that the formulas for the updated estimates and covariance in (72)-(76) are only for the optimal Kalman gain. For the usage of other Kalman gain values, the equations need to be changed accordingly.

4.2 Extended Kalman filter

In practice, most problems are nonlinear rather than the linear models as in equations (70)-(71). Before applying the Kalman filter, the system must be linearized. The Kalman filter that linearizes the current mean and the covariance is termed as

extended Kalman filter (EKF). A nonlinear continuous system and nonlinear discrete observations may be expresses as

$$dx_t / dt = f(x_t, u_t, t) + G(t)w_t, \quad t \geq t_0, \quad x_{t_0} \sim N(\hat{x}_{t_0}, P_{t_0}) \tag{77}$$

$$y_{t_k} = h(x_{t_k}, t_k) + v_k \tag{78}$$

where $G(t)$ is the system noise coefficient matrix, the other symbols are similar to those in section 4.1.

The state and the error covariance may be updated by the prediction equations (79) and (80), and by the updating at the observation equations (81)-(83).

Prediction

$$\hat{x}_{t_{k+1}|t_k} = \hat{x}_{t_k|t_k} + \int_{t_k}^{t_{k+1}} f(\hat{x}_{t|t_k}, u_t, t)dt \tag{79}$$

$$P_{t_{k+1}|t_k} = \Phi[t_{k+1}, t_k; \hat{x}_{t_k|t_k}]P_{t_k|t_k}\Phi^T[t_{k+1}, t_k; \hat{x}_{t_k|t_k}] + Q_{t_{k+1}} \tag{80}$$

Updating

$$\hat{x}_{t_{k+1}|t_{k+1}} = \hat{x}_{t_{k+1}|t_k} + K[t_{k+1}; \hat{x}_{t_{k+1}|t_k}] \times [y_{t_{k+1}} - h(\hat{x}_{t_{k+1}|t_k}, t_{k+1})] \tag{81}$$

$$\begin{aligned} P_{t_{k+1}|t_{k+1}} = {} & [I - K(t_{k+1}; \hat{x}_{t_{k+1}|t_k})H(t_{k+1}; \hat{x}_{t_{k+1}|t_k})]P_{t_{k+1}|t_k} \times [I - K(t_{k+1}; \hat{x}_{t_{k+1}|t_k})H(t_{k+1}; \hat{x}_{t_{k+1}|t_k})]^T \\ & + K(t_{k+1}; \hat{x}_{t_{k+1}|t_k})R_{k+1}K^T(t_{k+1}; \hat{x}_{t_{k+1}|t_k}) \end{aligned} \tag{82}$$

The Kalman gain matrix

$$K(t_{k+1}; \hat{x}_{t_{k+1}|t_k}) = P_{t_{k+1}|t_k}H^T(t_{k+1}; \hat{x}_{t_{k+1}|t_k})[H(t_{k+1}; \hat{x}_{t_{k+1}|t_k})P_{t_{k+1}|t_k}H^T(t_{k+1}; \hat{x}_{t_{k+1}|t_k}) + R_{k+1}]^{-1} \tag{83}$$

where $H[t_k; \hat{x}_{t_k|t_k}] = \left[\frac{\partial h_i(x_{t_k}, t_k)}{\partial x_j}\right]$ *at* $x_{t_k} = \hat{x}_{t_k|t_k}$; the state transition matrix Φ is obtained from Taylor's series of first order as $F[t_k; \hat{x}_{t_k|t_k}] = \left[\frac{\partial f_i(x_{t_k}, u_{t_k}, t_k)}{\partial x_j}\right]$ at $x_{t_k} = \hat{x}_{t_k|t_k}$, $\Phi[t_{k+1}, t_k; \hat{x}_{t_k|t_k}] = I + \Delta t F[t_k; \hat{x}_{t_k|t_k}]$, in which Δt is a sampling interval of measurements;

the denotations of the other terms in equations (79)-(83) are similar to those in section 4.1.

The EKF may be iterated globally as well as locally. For more details see [46-47]. When used for system identification, the unknown parameters to be determined may be contained in the state vector.

4.3 Adaptive Extended Kalman Filter and its application in structural identification

Despite the successful use of the Kalman filter, sometimes it is not the optimal choice and even leads to divergence due to the inaccuracy of the system models. To keep the filter stable, researchers have proposed to limit the memory of the Kalman filter by applying fading factors on the past data.

Fagin [50] used a constant fading factor λ_k to apply exponential fading on the past data, so the memory of the filter would be limited. The fading Kalman filter is identical to the one seen in section 4.1, except for the introduction of the forgetting factor into the error covariance Eq. (73) as the following

$$P_{k|k-1} = \lambda_k \Phi(k, k-1) P_{k-1|k-1} \Phi^T(k, k-1) + Q_{k-1} \tag{84}$$

with $\lambda_k \geq 1$, where the most recent observation is overweighed and subsequently divergence has been avoided.

The constant fading factor is not satisfactory for the systems with uncertainty, and it is necessary to vary the factor when there are unpredictable jumps and drifts. For this reason, many adaptive Kalman filter algorithms have been developed to estimate the fading factors. Xia et al. [51] proposed algorithms to adaptively adjust the forgetting factor using the predicted residuals. The value of the forgetting factor is computed by minimizing

$$f(\lambda;k) = 1/2\sum_{i=1}^{n}\sum_{j=1}^{m} S_{ij}^2(k) \tag{85}$$

where S_{ij} is the (i, j)th element of S(k),

$$S(k) = P_{k|k-1}H_k^T - K_k C_0(k) \tag{86}$$

where $C_0(k)$ is the covariance of the predicted observation residuals.

$$C_0(k) = E[(y_k - H_k\hat{x}_{k|k-1})(y_k - H_k\hat{x}_{k|k-1})^T] \tag{87}$$

As $f(\lambda;k)$ is minimized, $S(k)$ is closest to zero and the filter is optimized. λ_k may be computed by

$$\lambda_k = \max\{1, \frac{1}{m} trace\{[C_0(k) - H_k Q_{k-1} H_k^T - R_k][H_k \Phi(k,k-1) P_{k-1|k-1} \Phi^T(k,k-1) H_k^T]^{-1}\}\} \tag{88}$$

The single-variable forgetting factor cannot guarantee complete stability and optimality of the system estimation. The multiple forgetting factor Kalman filter was proposed to increase the predicted variance components by researchers [45, 48].

$$P_{k|k-1} = \Lambda(k)\Phi(k,k-1)P_{k-1|k-1}\Phi^T(k,k-1)\Lambda^T(k) + Q_{k-1} \tag{89}$$

where $\Lambda(k) = diag(\lambda_1(k), \lambda_2(k), \cdots, \lambda_n(k))$ contains the forgetting factors to be determined.

In [48], the forgetting factors in $\Lambda(k)$ are computed separately based on the statistical evaluations of the predicted residuals using a Chi-square test. In [45], the adaptive forgetting factors were used in EKF and applied to structural identification with abrupt changes of properties. The states to be estimated are similar as those in Eq. (60), $x_k = \left[X_1^T, X_2^T, X_3^T\right]_k^T$, where X_3 contains the unknown dynamic parameters to be identified. The objective function to be minimized for calculation of forgetting factors of

EKF is

$$f(\hat{X}_3[k\,|\,k;\Lambda(k)]) = \sum_l \left\| \frac{\hat{X}_{3,l}[k\,|\,k] - \hat{X}_{3,l}[k-1\,|\,k-1]}{\hat{X}_{3,l}[k-1\,|\,k-1]} \right\| \tag{90}$$

subjected to constraint of

$$\left\| C_0(k) - M_k R_{k+1}^{-1} M_k^{-1} \right\| \le \varepsilon$$

where

$$M_k = H(t_{k+1}; \hat{x}_{t_{k+1}|t_k}) P_{t_{k+1}|t_k} H^T(t_{k+1}; \hat{x}_{t_{k+1}|t_k}) + R_{k+1}$$

The basic idea of using the fading Kalman filter to detect structural damages is that the sudden changes of structural parameters result in jumps of the state, while the forgetting factors are able to limit the memory of the past data and outweigh the current data, therefore the changed parameters can be identified correctly.

5. Numerical Studies

Numerical studies were conducted to test the performance and feasibility of using the adaptive Kalman filter and wavelet analysis for substructure identification. The substructure identification without overlapping measurements as discussed in section 3 was performed on a 10 DOFs shear building, a 5-story plane frame structure, and a plane truss bridge. All the numerical examples were assumed to be linear elastic structures. The shear building underwent stiffness-proportional damping while the frame and truss endured Rayleigh damping. The external excitations on these structures were ground motion or forces. The El Centro earthquake wave was applied as the input excitation for shear building.

All the exact values of the structural properties were known and used for

establishing the finite element models for the structures. Then the dynamic responses were computed from the equations of motion of the finite element models by the Newmark-beta method. More details of this method can be referred to [52-54]. The Newmark-beta method, used in this study, where γ=0.5, β=0.25, is actually same to the constant average acceleration method.

In the identification process, the adaptive Kalman filter was used to track the damage quantitatively, and the wavelet scalogram was examined to identify damage qualitatively. In this study, all the masses were assumed to be known, and the stiffness and damping were the unknown parameters to be identified. The acceleration responses calculated by the Newmark-beta method were used as the observation measurements. The stiffness and damping of some elements of these structures were abruptly reduced during excitation to simulate actual damage in order to study the effectiveness of the structural identification algorithms in tracking the damage of substructures.

5.1 Example 1: 10-DOF shear building under ground motion

The 10-DOF is shown in Figure 25, the element numbers 1~10 begin from the lowest to the highest nodes. In the identification process, the masses m_1~m_{10} and acceleration responses are known parameters. The stiffness represented by k_1~ k_{10} and the damping coefficients represented by c_1~ c_{10} were the unknown parameters to be identified.

5.1.1 State space equations for the substructures

The entire structure was divided into two substructures, namely substructure 1 and substructure 2 as illustrated in Figure 25.

The equation of motion for substructure 1 can be written as

$$M_{s1}\ddot{u}^r_{s1}(t)+C_{s1}\dot{u}^r_{s1}(t)+K_{s1}u^r_{s1}(t)=F_{s1}(t)-M_{s1}\eta_{s1}\ddot{u}_5(t) \tag{91}$$

where $u_i^r(t)$ denotes the *i-th* relative displacement with respect to u_5, and the structural matrices are

$$M_{s1}=\begin{bmatrix} m_6 & & & & \\ & m_7 & & & \\ & & m_8 & & \\ & & & m_9 & \\ & & & & m_{10} \end{bmatrix}; C_{s1}=\begin{bmatrix} c_6+c_7 & -c_7 & & & \\ -c_7 & c_7+c_8 & -c_8 & & \\ & -c_8 & c_7+c_8 & -c_9 & \\ & & -c_9 & c_8+c_9 & -c_{10} \\ & & & -c_{10} & c_{10} \end{bmatrix};$$

$$K_{s1}=\begin{bmatrix} k_6+k_7 & -k_7 & & & \\ -k_7 & k_7+k_8 & -k_8 & & \\ & -k_8 & k_7+k_8 & -k_9 & \\ & & -k_9 & k_8+k_9 & -k_{10} \\ & & & -k_{10} & k_{10} \end{bmatrix};\ \eta_{s1}=[1\quad 1\quad 1\quad 1\quad 1]^T$$

Since only ground motion was applied, $F_{s1} = 0$.

The state variables are

$$X_1=[u_6^r\quad u_7^r\quad u_8^r\quad u_9^r\quad u_{10}^r]^T;\ X_2=[\dot{u}_6^r\quad \dot{u}_7^r\quad \dot{u}_8^r\quad \dot{u}_9^r\quad \dot{u}_{10}^r]^T$$

$$X_3=[k_6\quad k_7\quad k_8\quad k_9\quad k_{10}]^T;\ X_4=[c_6\quad c_7\quad c_8\quad c_9\quad c_{10}]^T$$

$$X=[X_1^T\quad X_2^T\quad X_3^T\quad X_4^T]^T$$

The state equation can be expressed as

$$\frac{d}{dt}\begin{Bmatrix} X_1 \\ X_2 \\ X_3 \\ X_4 \end{Bmatrix}=\begin{Bmatrix} X_2 \\ -M_{s1}^{-1}(C_{s1}(X_4)X_2+K_{s1}(X_3)X_1)-\eta_{s1}\ddot{u}_5(t) \\ 0 \\ 0 \end{Bmatrix} \tag{92}$$

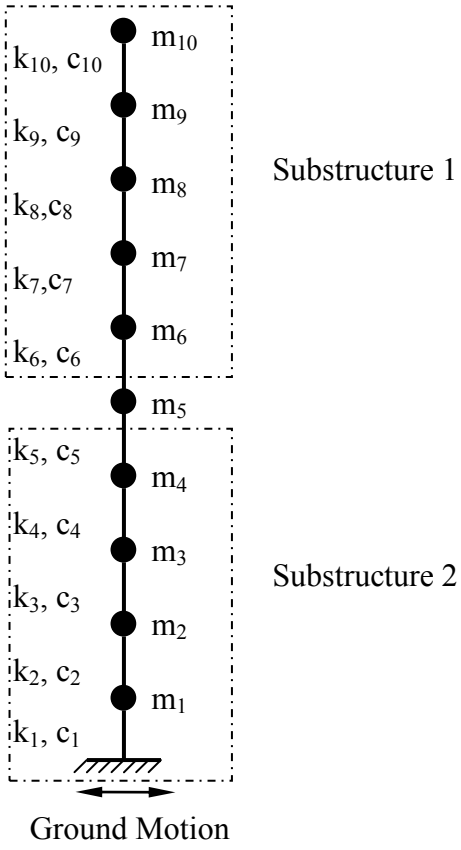

Figure 25. 10-DOF shear building for Example 1.

The discrete observation equation is

$$Y = [\ddot{u}_6 \quad \ddot{u}_7 \quad \ddot{u}_8 \quad \ddot{u}_9 \quad \ddot{u}_{10}]^T \tag{93}$$

The equation of motion for substructure 2 can be expressed as

$$M_{s2}\ddot{u}^r_{s2}(t) + C_{s2}\dot{u}^r_{s2}(t) + K_{s2}u^r_{s2}(t) = -M_{s2}\eta_{s2}\ddot{u}_6(t) - M_{s2}\eta_{s2}\ddot{u}_g(t) \tag{94}$$

where $\ddot{u}_g$ is the ground acceleration, superscript r means the parameter is relative respect to that of element 6, and the structural matrices are

$$M_{s2} = \begin{bmatrix} m_1 & & & & \\ & m_2 & & & \\ & & m_3 & & \\ & & & m_4 & \\ & & & & m_5 \end{bmatrix};\ C_{s2} = \begin{bmatrix} c_1+c_2 & -c_2 & & & \\ -c_2 & c_2+c_3 & -c_3 & & \\ & -c_3 & c_3+c_4 & -c_4 & \\ & & -c_4 & c_4+c_5 & -c_5 \\ & & & -c_5 & c_5+c_6 \end{bmatrix}$$

$$K_{s2}=\begin{bmatrix} k_1+k_2 & -k_2 & & & \\ -k_2 & k_2+k_3 & -k_3 & & \\ & -k_3 & k_3+k_4 & -k_4 & \\ & & -k_4 & k_4+k_5 & -k_5 \\ & & & -k_5 & k_5+k_6 \end{bmatrix};\ \eta_{s2}=[1 \quad 1 \quad 1 \quad 1 \quad 1]^T$$

The state vectors are given as

$$X_1=[u_1 \quad u_2 \quad u_3 \quad u_4 \quad u_5]^T;\ X_2=[\dot{u}_1 \quad \dot{u}_2 \quad \dot{u}_3 \quad \dot{u}_4 \quad \dot{u}_5]^T$$

$$X_3=[k_1 \quad k_2 \quad k_3 \quad k_4 \quad k_5]^T;\ X_4=[c_1 \quad c_2 \quad c_3 \quad c_4 \quad c_5]^T$$

$$X=[X_1^T \quad X_2^T \quad X_3^T \quad X_4^T]^T \tag{95}$$

The state equation can be expressed as

$$\frac{d}{dt}\begin{Bmatrix} X_1 \\ X_2 \\ X_3 \\ X_4 \end{Bmatrix}=\begin{Bmatrix} X_2 \\ -M_{s2}^{-1}(C_{s2}(X_4)X_2+K_{s2}(X_3)X_1)-\eta_{s2}\ddot{u}_6(t)-\eta_{s2}\ddot{u}_g(t) \\ 0 \\ 0 \end{Bmatrix} \tag{96}$$

The discrete observation equation is

$$Y=[\ddot{u}_1 \quad \ddot{u}_2 \quad \ddot{u}_3 \quad \ddot{u}_4 \quad \ddot{u}_5]^T \tag{97}$$

The previous results identified from substructure 1 can be used to identify substructure 2. For example, the damping force can be added to the RHS of Eq. (94). And the state variables can be changed accordingly. These are beyond the scope of this study, only the results of Eq. (94) were discussed in this paper.

The structural parameters used in this study are the same as those of the 5-DOF system in [45]. The values of lumped masses are: $m_1 = m_2 = m_3 = m_4 = m_5 = m_6 = m_7 = m_8 = m_9 = m_{10} = 125.53$ kg. The values of stiffness are: $k_1 = k_2 = k_3 = k_4 = k_5 = k_6 = k_7 = k_8 = k_9 = k_{10} = 24.49$ kN/m. The stiffness-proportional damping coefficients are assumed to be: $c_1 = c_2 = c_3 = c_4 = c_5 = c_6 = c_7 = c_8 = c_9 = c_{10} = 0.175$ kN s/m. The k_8 and c_8 reduced

abruptly after damage at t = 10 seconds new values: $k_{8,\text{after damage}}$ = 15.0 kN/m, $c_{8,\text{after damage}}$ = 0.12 kN.s/m. It must be pointed out that the values for each DOF are identical and this is acceptable for examination of identification algorithm, while they can differ from each other and more practical values can be used in future studies. Initial estimate for values of the stiffness and damping are 20 kN/m and 0.15 kN.s/m, respectively.

The ground motion applied to the shear building was El Centro earthquake acceleration as illustrated in Figure 26. The PGA = 3.08 g, time duration = 30 seconds, and time interval = 0.001 seconds. The responses for each DOF due to the El Centro ground acceleration are shown in Figure 27. The random excitation by means of Gaussian white noise at the 3rd, 6th, 9th nodes had also been tried, however, the identified results were not as effective as applying the El Centro ground motion, therefore, the identified results for this case need further examination and are not shown in this paper.

In the identification process, the masses and acceleration responses were known, while the stiffness and damping were the unknown parameters to be determined. The output noises were not considered in the numerical studies. The identified results by using adaptive Kalman filter are illustrated in the following figures and tables.

5.1.2 Numerical results and discussion

In the application of the adaptive Kalman filter, due to numerical issues, the values of R and Q should be selected and finely tuned in order to get satisfactory results; they should be assigned small values instead of zeros for the case without noise. These values can have significant influence on the final estimated tracking results. The weight values may also have significant effects and further studies are needed in order to determine these values. Some identification results are demonstrated in this section to

show the ability of the adaptive Kalman filter. In the identification process, the masses and acceleration responses are known, while the stiffness and damping are the unknown parameters to be determined.

Three identification cases were analyzed: a) the identification of substructure 1 without output noise; b) the identification of substructure 2 without output noise; c) the identification of substructure 2 with 2% root-mean-square (RMS) output noise.

For the identification of substructure 1 without output noise, the parameters k_6~k_{10}, and c_6~c_{10} were to be determined. The initial estimate of the stiffness and damping values were 20 kN/m and 0.15 kN.s/m, respectively. Figure 28 plots the identified values and the exact values with respect to time. Table 10 lists the errors of final identified values compared to the exact values for substructure 1 from Example 1. It was observed that the stiffness can be identified very well with errors less than 3%, and the abrupt change of stiffness can also be effectively tracked. The damping can be identified well, but the identified values of damping converge more slowly and are less stable than the identification of stiffness.

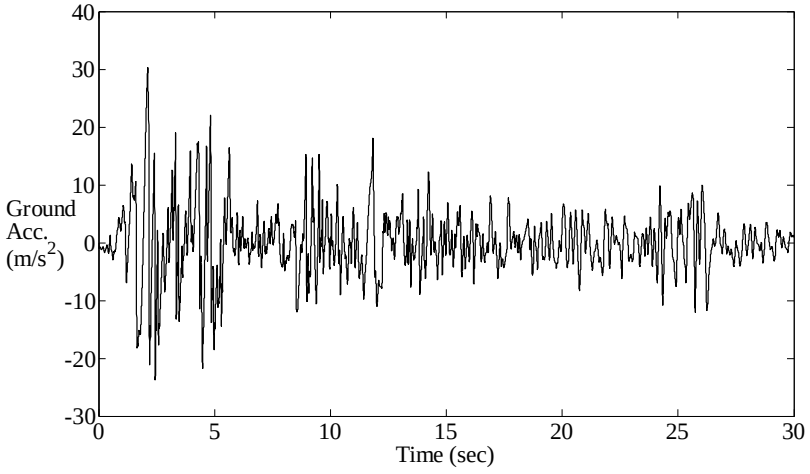

Figure 26. The ground acceleration applied to the 10-DOF shear building.

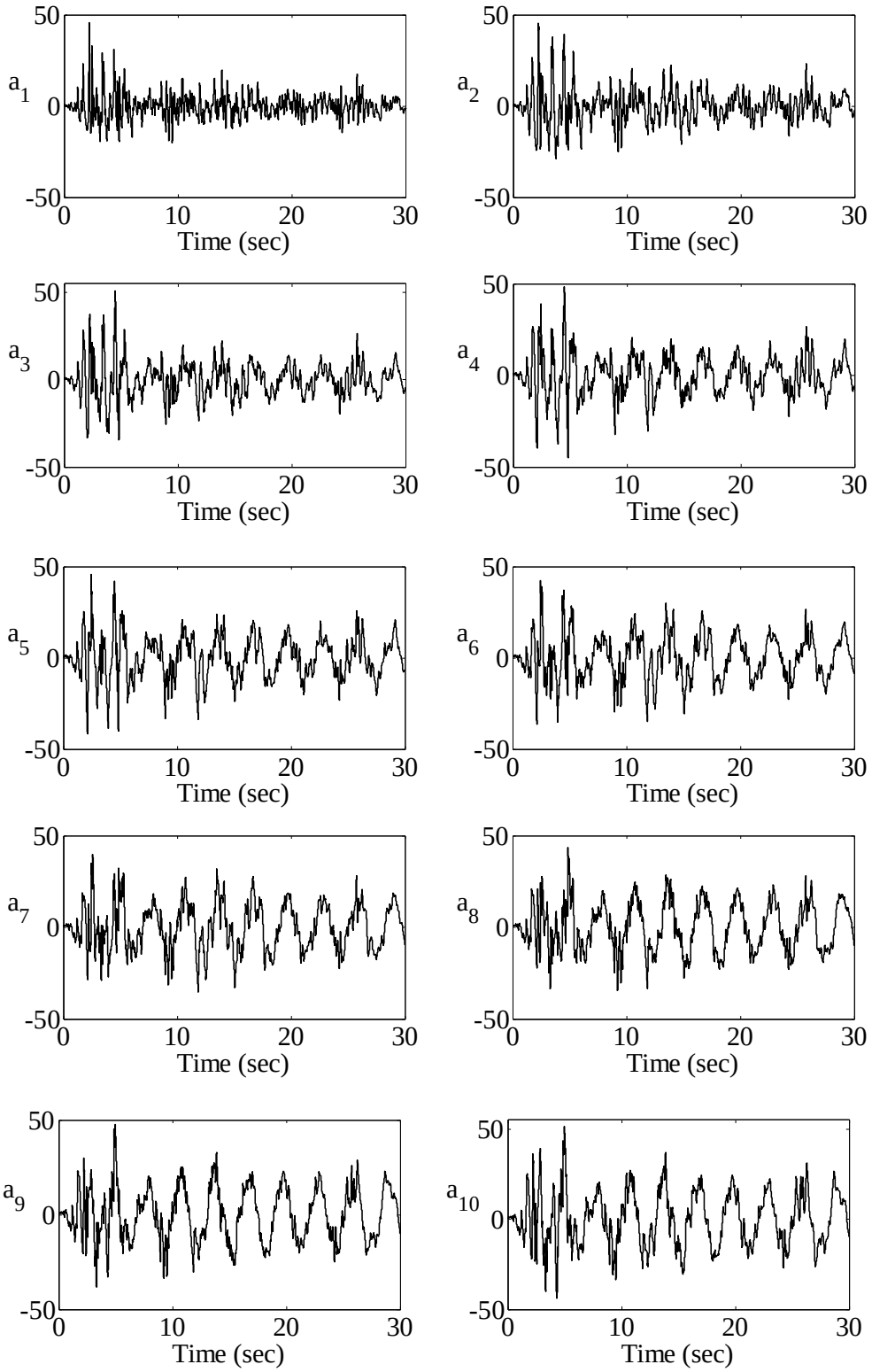

Figure 27. The acceleration responses due to the El Centro ground acceleration in m/s^2.

For the identification of substructure 2 without output noise, the parameters k_1~k_5, and c_1~c_5 were to be determined. The initial guess of the stiffness and damping values were 20 kN/m and 0.15 kN.s/m, respectively. Figure 29 plots the identified values and the exact values with respect to time. Table 11 lists the errors of final identified values compared to the exact values for substructure 2 from Example 1. It was found that stiffness can be identified effectively with errors less than 5%, and the abrupt change of stiffness can be tracked well. The damping can be identified within 15% error, and the identified values of damping converge much more slowly.

As for the identification of substructure 2 with 2% RMS output noise, the parameters to be determined and the initial hypothesis of the unknown parameters are same as the case without noise. Figure 30 plots the identified values and the exact values with respect to time. Table 12 lists the errors of final identified values compared to the exact values for substructure 2 of Example 1 with 2% noise. Our research determined that stiffness can be identified effectively with errors of less than 9%, and the abrupt change of stiffness can be tracked well. The damping can be identified within a 29% error, and the identified values of damping converge much slower. Comparing the results of the same substructure, i.e. substructure 2 here, with and without output noise, it can be concluded that the added noise can reduce the accuracy of the identified results, while if the noise is at a low level, the identified results are still reasonable and can converge within a short time.

5.2 Example 2: 6-story plane frame structure with 18 DOFs

The frame used here was similar to but not exactly the same as the frame in [18].

The 6-story plane frame is shown in Figure 31(a), the element numbers are illustrated. The axial deformations have been ignored, therefore each story was modeled by 3 DOFs, i.e., 1 horizontal translation and 2 rotations as demonstrated in Figure 31(b). The height of each story was 4m and the length of each beam was 9m. The linear mass densities of the column and beam were 33 kg/m and 0.058 kg/m respectively. The flexural stiffness for the 18 members is listed in Table 13. For convenience, the E_iI_i/l_i will be denoted by k_i in the following discussion. The finite element model is constructed by using these structural properties, the mass and stiffness matrices of the entire structure can be denoted by M and C. The Rayleigh damping was used to obtain the damping matrix, namely $C = \alpha M + \beta K$. The two damping coefficients are $\alpha = 0.6344$, $\beta = 0.002061$.

A sinusoidal force f(t) was applied horizontally on the roof floor as shown in Figure 31. The sampling rate was 1000 Hz. After some trial tests, to get good identification results, a range of different frequencies rather than a single frequency were used as follows:

$$f(t) = \sum_{i=1}^{Nf} A_i \sin(2\pi f_i + \phi_i) \tag{98}$$

where A_i, f_i, and φ_i are the amplitude, frequency, and phase angle, respectively, of the i-th sinusoidal component. The frequencies f_i ranging from 1.75 Hz to 55 Hz were used for the force and some values were chosen for amplitudes and phases.

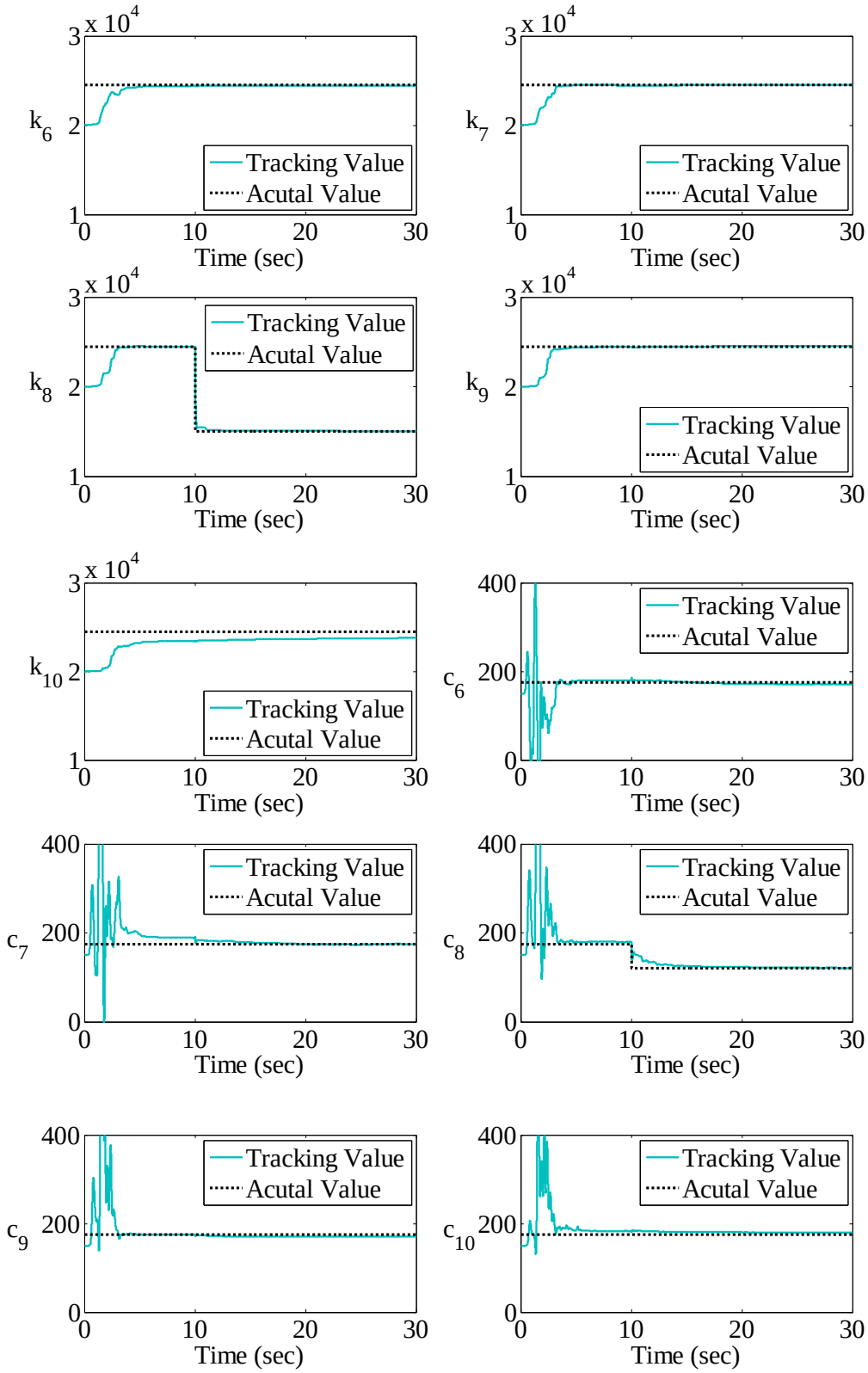

Figure 28. Comparison of the identified results with the exact values for substructure 1of Example 1 w/o noise (unit for stiffness: N/m; unit for damping: N.s/m).

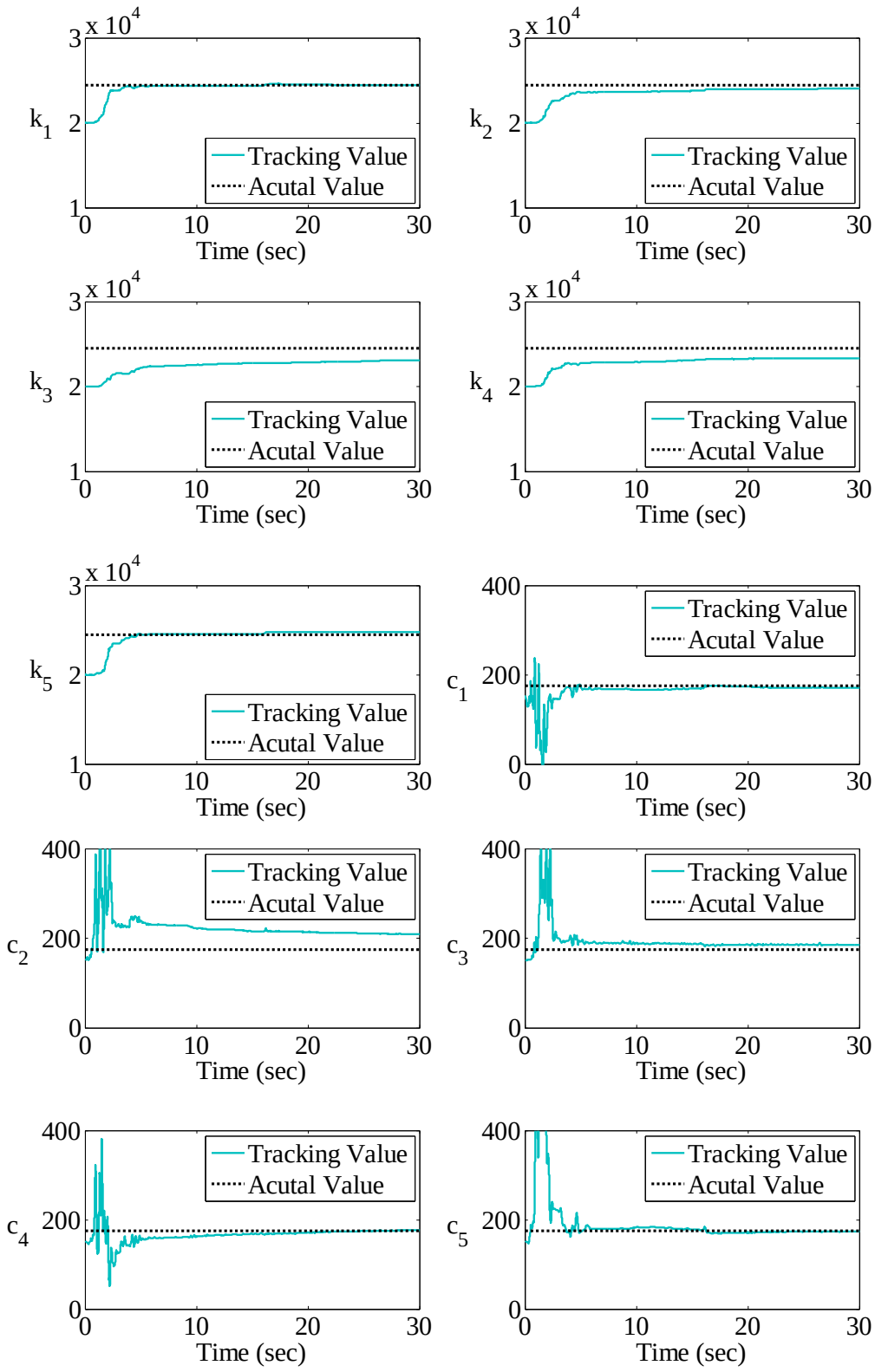

Figure 29. Comparison of the identified results with the exact values for substructure 2 of Example 1 w/o noise (unit for stiffness: N/m; unit for damping: N.s/m).

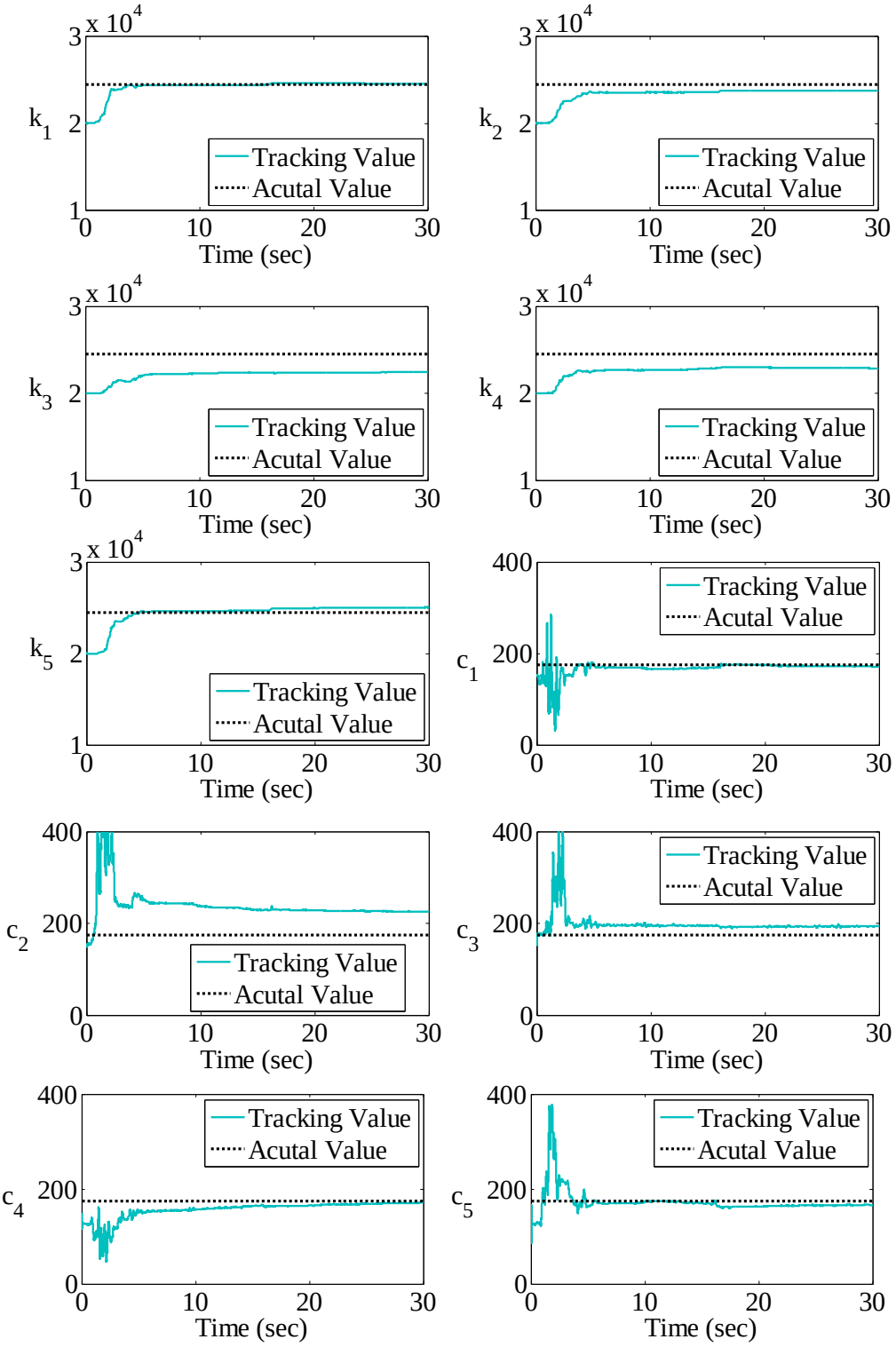

Figure 30. Comparison of the identified results with the exact values for substructure 2 of Example 1 w/ 2% noise (unit for stiffness: N/m; unit for damping: N.s/m).

Table 10. The errors of identified results for substructure 1 of Example 1, w/o noise

Stiffness parameter	k_6	k_7	k_8 before damage	k_8 after damage	k_9	k_{10}
Error (%)	-0.06	-0.03	-0.01	0.29	0.19	-2.94
Damping parameter	c_6	c_7	c_8 before damage	c_8 after damage	c9	c_{10}
Error (%)	-2.23	0.19	2.59	1.14	-2.66	2.54

Table 11. The errors of identified results for substructure 2 of Example 1, w/o noise

Stiffness Parameter	k_1	k_2	k_3	k_4	k_5
Error (%)	0.57	2.70	5.63	4.92	-0.15
Damping parameter	c_1	c_2	c_3	c_4	c_5
Error (%)	-4.01	14.96	7.97	0.65	1.04

Table 12. The errors of identified results for substructure 2 of Example 1, w/ 2% noise

Stiffness Parameter	k_1	k_2	k_3	k_4	k_5
Error (%)	0.37	3.01	8.29	6.64	2.23
Damping parameter	c_1	c_2	c_3	c_4	c_5
Error (%)	1.98	29.02	10.71	1.95	5.15

The damage was simulated by reducing both k_7 and k_8 to the values 600 kN/m, which occurred at t = 15 seconds after the excitation was applied. The modal frequencies and damping ratios for the frame structure before and after damage are listed in Table 14, which shows that the frequencies of the damaged model were lower than those of the undamaged model.

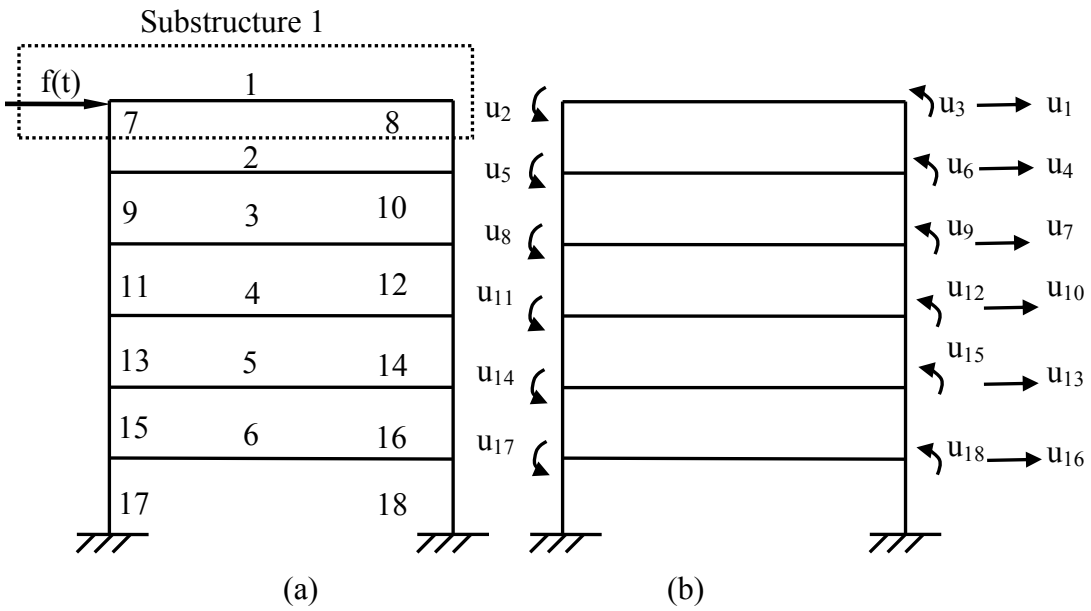

Figure 31. Frame structure: (a) structural model; (b) degrees of freedom

Table 13. Flexural stiffness of the frame members.

Element No.	1	2	3	4	5	6	7	8	9
E_iI_i/l_i (kN/m)	2730	2880	2870	2750	2770	2811	1800	1820	1760
Element No.	10	11	12	13	14	15	16	17	18
E_iI_i/l_i (kN/m)	1890	1860	1830	1730	1760	1900	1920	1876	1892

For the identification of substructure 1, the masses and accelerations of the substructure were known, and the parameters k_1, k_7, k_8, α, and β associated with substructure 1 were to be determined. The initial estimates of these values were 2500 kN/m, 1200 kN/m, 1200 kN/m, 0.7, and 1.8, respectively. Figure 32 shows the identified and exact values. Table 15 lists the errors of final identified values compared to the exact values for substructure 1 of Example 2. It is observed that with reasonable initial guess of unknown parameters, the stiffness can be identified very well with an error of less than 4%, and the abrupt change of stiffness can also be tracked well. The identified values of damping converged adequately, but the errors of converged values were large up to 29%. Hence, damping can be a reference but is not recommended as a damage indicator alone.

Table 14. The modal frequencies and damping ratios of the frame before and after damage

Modal No.	Before damage		After damage	
	Frequency (Hz)	Damping ratio (%)	Frequency (Hz)	Damping ratio (%)
1	1.63	4.15	1.62	4.17
2	5.03	4.26	4.68	4.11
3	8.64	6.18	7.52	5.54
4	12.60	8.56	11.18	7.69
5	16.49	10.99	15.52	10.37
6	19.31	12.76	16.27	10.84
7	19.46	12.86	19.13	12.65
8	21.63	14.24	20.69	13.64
9	24.05	15.78	22.54	14.82
10	26.73	17.50	25.41	16.65
11	29.18	19.07	28.54	18.66
12	30.64	20.01	30.43	19.87
13	61.06	39.62	59.21	38.42
14	65.23	42.31	63.38	41.12
15	72.09	46.75	68.71	44.56
16	80.10	51.93	76.07	49.32
17	87.37	56.63	85.19	55.22
18	92.28	59.81	91.42	59.25

Table 15. The errors of identified results for substructure 1 of Example 2, w/o noise.

	k_1	k_7 before damage	k_7 after damage	k_8 before damage	k_8 after damage	α	β
Error (%)	3.71	-1.39	0.86	-1.30	0.92	-29.14	16.08

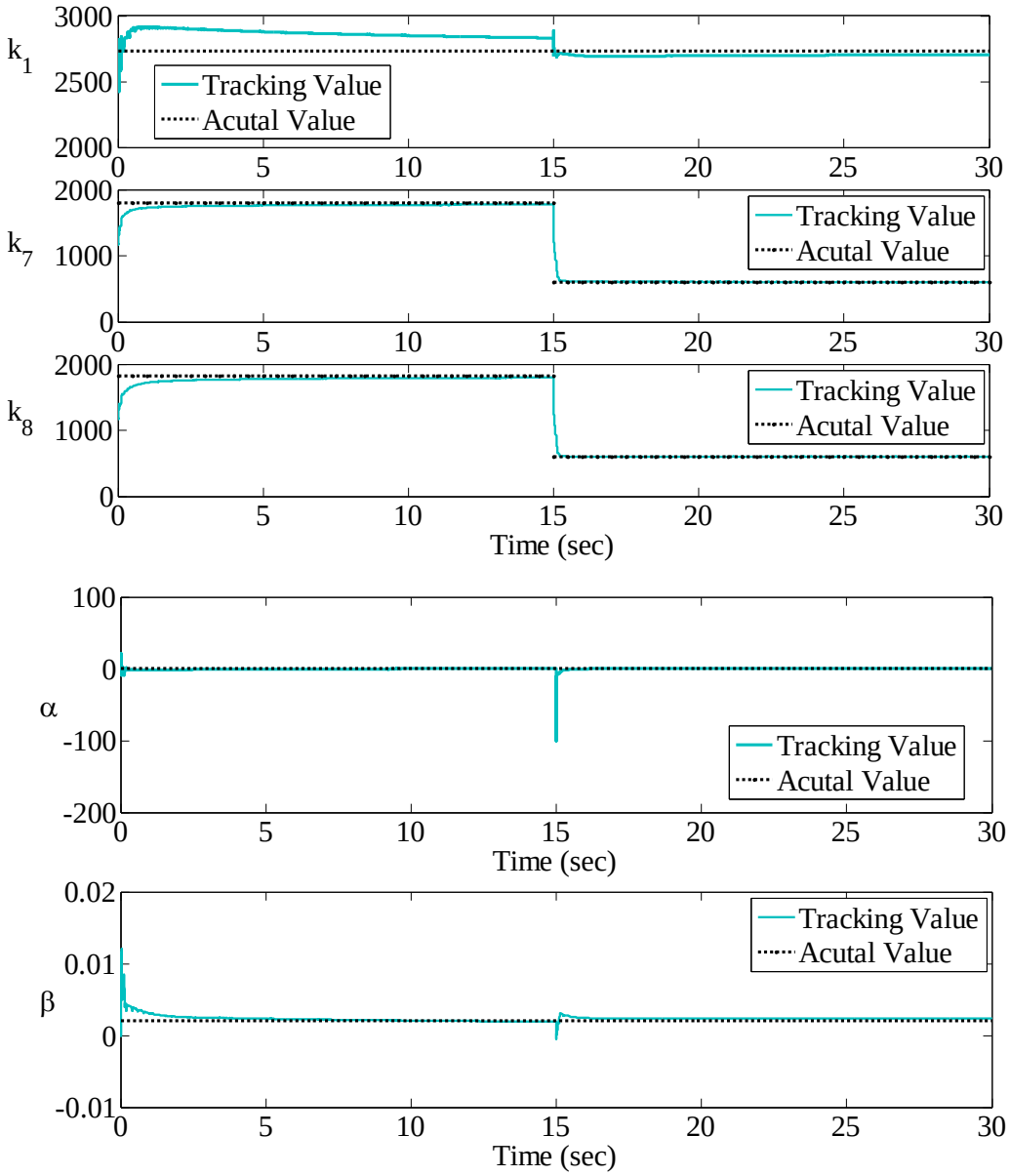

Figure 32. Comparison of the identified results with the exact values for substructure 1 of Example 2 (unit for stiffness: kN/m).

5.3 Example 3: 10-DOF plane truss bridge

The plane truss bridge model supported at two ends is as illustrated in Figure 33, where the node and element numbers are shown. Each node has two degrees of freedom, i.e., horizontal (x) and vertical (y) translations. The structural properties are the same as

those of the truss bridge model in [55] and listed in Table 16. The stiffness and mass matrices of the entire truss structure may be obtained from

$$K = \sum_{e=1}^{n} K^e = \sum_{e=1}^{n} L^e k^e (L^e)^T;\ M = \sum_{e=1}^{n} M^e = \sum_{e=1}^{n} L^e m^e (L^e)^T \tag{99}$$

where L^e is the position vector, and the global stiffness and mass matrices are

$$k^e = E_i A_i / l_i \begin{bmatrix} c^2 & cs & -c^2 & -cs \\ cs & s^2 & -cs & -s^2 \\ -c^2 & -cs & c^2 & cs \\ -cs & -s^2 & cs & s^2 \end{bmatrix};\ m^e = \rho_i / 6 \begin{bmatrix} 2c^2 & 2cs & c^2 & cs \\ 2cs & 2s^2 & cs & s^2 \\ c^2 & cs & 2c^2 & 2cs \\ cs & s^2 & 2cs & 2s^2 \end{bmatrix}$$

where $c = \cos\theta_i$, $s = \sin\theta_i$, θ is the angles between members as shown in Figure 33, E is Young's modulus, A is cross-sectional area, and ρ is mass density.

The Rayleigh damping was used to obtain the damping matrix $C = \alpha M + \beta K$. The two damping coefficients were chosen as $\alpha = 0.566$; $\beta = 8.62 \times 10^{-4}$. The sinusoidal force was acted upon node 3 along the y direction. The sinusoidal force consisted of a range of excitation frequencies, and can be expressed in Eq. (98). The frequency f_i used for the force on the truss range from 2 Hz to 20 Hz, and some values were chosen for amplitudes and phases. The sampling rate was 1000 Hz.

The truss bridge was divided into substructure 1 and the remaining substructure. The axial stiffness $E_1A_1/l_1 \sim E_6A_6/l_6$, and the damping coefficients α and β were to be determined. For convenience, the E_iA_i/l_i will be denoted by k_i in the following discussion. The damage occurred at t = 10 seconds counted from the start of excitation. The k_3 and k_9 reduced abruptly from 16617 to 6000 kN/m, all the other values were assumed to be constants. The modal frequencies and damping ratios for the truss in both undamaged and damaged states are listed in Table 17.

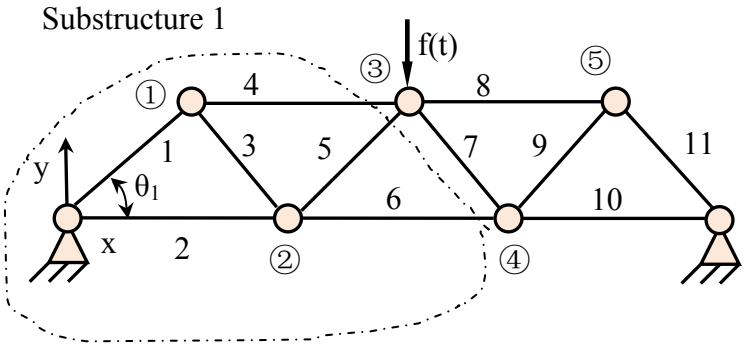

Figure 33. Truss bridge model for Example 3: the circled numbers denote node numbers and the numbers w/o circles denote the element number.

Table 16. Structural properties of the truss bridge

Element No.	E_iA_i/l_i (kN/m)	$\rho_i l_i/6$ (kg/m^2)	θ (radian)
1	14142	540	π/4
2	11000	520	0
3	16617	530	3π/4
4	11500	510	0
5	15627	550	π/4
6	10000	560	0
7	15627	550	3π/4
8	11500	510	0
9	16617	530	π/4
10	11000	520	0
11	14142	540	3π/4

Table 17. The modal frequencies and damping ratios of the truss before and after damage

	Before damage		After damage	
Modal No.	Frequency (Hz)	Damping ratio (%)	Frequency (Hz)	Damping ratio (%)
1	1.92	2.86	1.73	3.07
2	4.43	2.22	4.32	2.21
3	6.29	2.42	5.82	2.35
4	9.05	2.95	8.29	2.79
5	12.59	3.77	10.73	3.33
6	12.75	3.81	11.36	3.47
7	15.28	4.43	13.45	3.98
8	16.43	4.72	13.80	4.06
9	20.85	5.86	18.64	5.29
10	21.39	6.00	20.66	5.81

For the identification of substructure 1, the masses and the acceleration responses of the substructure were known, and the parameters k_1~k_6, α, and β associated with substructure 1 were yet to be determined. The initial estimate of these values was 16000 kN/m, 8000 kN/m, 11000 kN/m, 15000 kN/m, 18000 kN/m, 8000 kN/m, 5, and 8, respectively. Figure 34 plots the identified values and the exact values with respect to time. Table 18 lists the errors of final identified values compared to the exact values for substructures 1 found in Example 3. It was observed that the stiffness could be identified very well with an percent error of less than 5%, and the abrupt change of stiffness could also be tracked efficiently. The identified values of damping converged almost completely, the errors of the final identified values were approximately 6%, which are better than those of the frame in Example 2, and this may be because the DOFs of the truss were less than those of Example 2. Hence the identified damping can be a reference indicator for structural health monitoring.

Table 18. The errors of identified results for substructure 1 of Example 3, w/o noise.

	k_1	k_2	k_3 before damage	k_3 after damage	k_4
Error (%)	0.05	6.31	-0.17	0.06	-0.09
	k_5	k_6	α	β	
Error (%)	0.40	-4.52	-4.95	6.17	

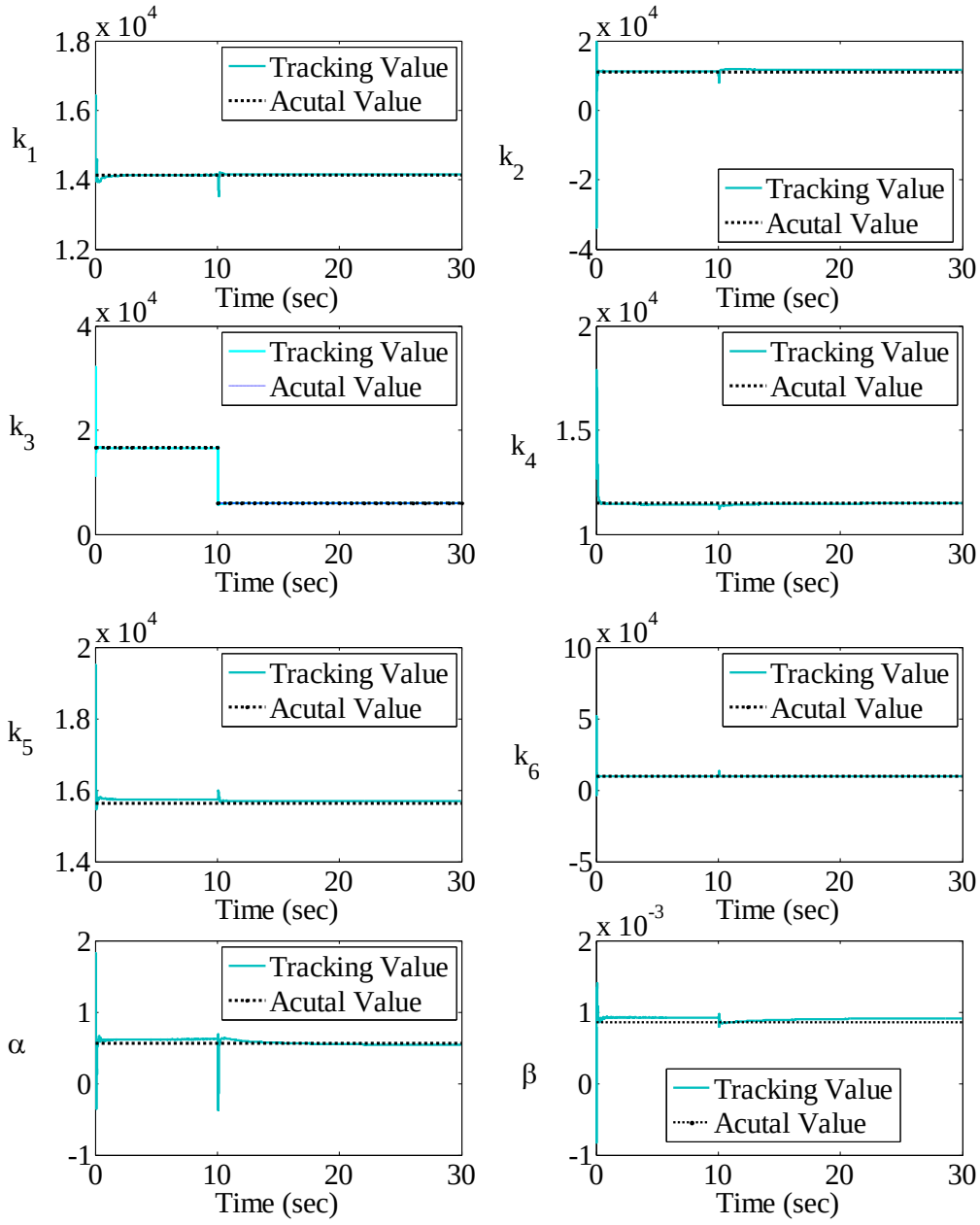

Figure 34. Comparison of the identified results with the exact values for substructure 1 of Example 3 (unit for stiffness: kN/m).

6. Wavelet Scalogram in Damage Identification of Substructures

Wavelet theory has emerged over the past twenty years as one of the best signal processing tools and is known for its many advantages. Wavelets can be used for multi-scale analysis of signals and extraction of time-frequency features, and therefore is suitable to process non-stationary signals. Wavelet analysis was applied in fault diagnostics, structural performance testing, and ground motion analysis [56-57]. It was used in damage detection of various structures, e.g., beam [58-60], plate [61-62], and frame structures [63]. The occurrence of either abrupt or accumulative damage of structures can be determined by the wavelet analysis of response measurement, e.g., abrupt stiffness degradation [64]. This study makes use of the wavelet in determining the presence of abrupt stiffness degradation in the substructures of a frame structure.

6.1 Brief introduction of wavelet transform

The wavelet $\psi_{a,b}(t)$ generated by dilation and translation from the analyzing wavelet $\psi(t)$ is defined as

$$\psi_{a,b}(t) = |a|^{-1/2} \psi\left(\frac{t-b}{a}\right) \tag{100}$$

where a is a scale parameter and b is a translation parameter. $\psi(t)$ is called the mother wavelet, and $\psi_{a,b}(t)$ is called the son wavelet.

It is supposed that $\psi(t) \in L^2(\mathbb{R})$ and it satisfies the admissibility condition,

$$C_\psi = \int |\omega|^{-1} |\hat{\psi}(\omega)|^2 \, d\omega < \infty \tag{101}$$

where $\hat{\psi}(\omega) = \int \psi(t) e^{-i\omega t} dt$ is the Fourier transform. It can be derived that,

$$\int \psi(t)dt = 0 \tag{102}$$

The wavelet transform of a function is a linear transform that correlates a finite-energy function x(t) with a series of oscillating functions $\psi_{a,b}(t)$ as

$$Wx(a,b) = |a|^{-1/2} \int x(t)\psi^{*}_{a,b}(t)dt > 0 \tag{103}$$

where the asterisk denotes complex conjugate.

The function can be reconstructed by the inverse wavelet transform

$$x(t) = C_{\psi}^{-1} \int_{-\infty}^{\infty} \int_{-\infty}^{\infty} \frac{da\, db}{a^2} |Wx(a,b)|^2 \tag{104}$$

The modulus is defined as

$$\|Wx(a,b)\| = (\mathrm{Re}^2[Wx(a,b)] + \mathrm{Im}^2[Wx(a,b)])^{1/2} \tag{105}$$

The phase is defined as

$$\varphi(a,b) = \arctan \frac{\mathrm{Im}[Wx(a,b)]}{\mathrm{Re}[Wx(a,b)]} \tag{106}$$

Wavelet scalogram is defined as the square of the modulus of the wavelet transform and represents energy density that measures the energy of *x(t)* in the Heisenberg box of each wavelet $\psi_{a,b}(t)$ centered at $(a, \xi = \frac{\eta}{b})$ [65]:

$$P_W x(a,\xi) = \|Wx(a,b)\|^2 = \left\| Wx(a, \frac{\eta}{\xi}) \right\|^2 \tag{107}$$

It can be regarded as a spectrum with constant relative bandwidth. Wavelet scalograms were employed in this study to determine the occurrence of abrupt damage of structures.

A variety of mother wavelets, which include Haar, Morlet, Mexican Hat, Hermitian, and Daubechies wavelets, have been developed to meet different criteria. The Morlet wavelet consists of a Fourier wave modulated by a Gaussian envelope. It has a

good time-frequency localization feature, and has been applied in seismic signal detection [66]. It has also been proven to be a strong tool for feature extraction for mechanical vibration signals and fault diagnosis [67-68]. Based on these research, the complex Morlet wavelet was chosen for this study, which is defined as in [69]:

$$\psi(x) = \frac{1}{\sqrt{\pi f_b}} e^{2i\pi f_c x} e^{-\frac{x^2}{f_b}} \tag{108}$$

where f_b is a bandwidth parameter, f_c is a wavelet center frequency. $f_b = 1.5$, $f_c = 1$ were used in this study.

6.2 Application of wavelet scalogram of acceleration in damage detection

To investigate the feasibility of the wavelet method in damage identification and localization of structures, wavelet analyses were conducted on the frame structure of Example 2 in section 5. Cases of damage as well as cases where no damage occurred were considered. The external excitation was El Centro acceleration instead of the sine waves in section 5, and the stiffness of members 7 and 8 abruptly reduced at 15 seconds for the damaged case. The acceleration responses and their wavelet scalograms were used to determine the occurrence and location of damage qualitatively in the current research stage.

Although accelerations were examined, we were unable to determine if any degradation was present. The structural degradation can be detected by comparing the energy of the vibration signals before and after damage, which are represented by wavelet scalograms. To examine the ability of wavelets in detection of the structural damage, the wavelet scalograms of accelerations were plotted. Figures 35 and 36 show the scalograms

of accelerations $\ddot{u}_3, \ddot{u}_4, \ddot{u}_7$, and $\ddot{u}_{13}$ for both undamaged and damaged scenarios. It was observed that the scalograms of DOFs that were within or near the damaged areas, e.g. $\ddot{u}_3$ and $\ddot{u}_4$, showed significant changes when damage occurred. Generally there was much less high frequency energy after damage. The scalograms of DOFs that were farther away from damage locations indicated much fewer changes, As for the DOFs that were far enough, e.g., $\ddot{u}_{13}$, it was found that the changes in scalograms were negligible.

It can be concluded that the abrupt reduction of stiffness can have considerable effects on the scalogram. For DOFs of the area that were further away from the damage, the acceleration scalograms changed less compared to those of the undamaged structure for the same DOFs. This may be useful for initial determination and location of damage.

7. Summary and Conclusions

In this study, an adaptive Kalman filter was used to identify varying substructural parameters under external excitations. Identification of structural properties can be very useful for structural health monitoring and structural model updating. The effectiveness of the adaptive Kalman filter in substructure identification was investigated by performing numerical studies on three types of linear structures: a shear building, a plane frame building, and a plane truss bridge. In the numerical studies, the masses and the acceleration responses were known and used for identification of the unknown stiffness and damping.

Conclusions from these numerical studies can be briefly summarized. The estimation of the initial state parameters should be in a reasonable range to obtain faster convergence. The weight values in the algorithm should be selected properly to obtain

convergence. The results showed that if given proper initial estimates of the state and weight values, the stiffness can be accurately determined and the abrupt changes of stiffness can be tracked quite well. The damping can also be identified but with slower convergence and more significant errors. Comparing the identifications of substructure 2 without output noise and with 2% RMS output noise showed that the method can still identify the stiffness and damping effectively. However, the added noise can reduce the accuracy of the identified values and extend convergence time.

This study proposed use of wavelet transform for substructural damage identification. Wavelet scalograms of acceleration responses of the frame structure with damage during external excitation were examined. The scalograms of the damaged scenario were significantly different from those of the undamaged case, the further from the damage location, the greater the differences. It can be concluded that the scalograms can indicate changes of structural parameters and approximately locate damage.

Use of the actual measurements of real structures is desired for substructure identification with the adaptive Kalman filter algorithm. The accuracy and robustness of the methods need to be improved, and the convergence time should be reduced for large structures. With regard to substructural damage identification with wavelet analysis, further study is necessary for obtaining quantitative results and a clearer interpretation with results based on actual measurements.

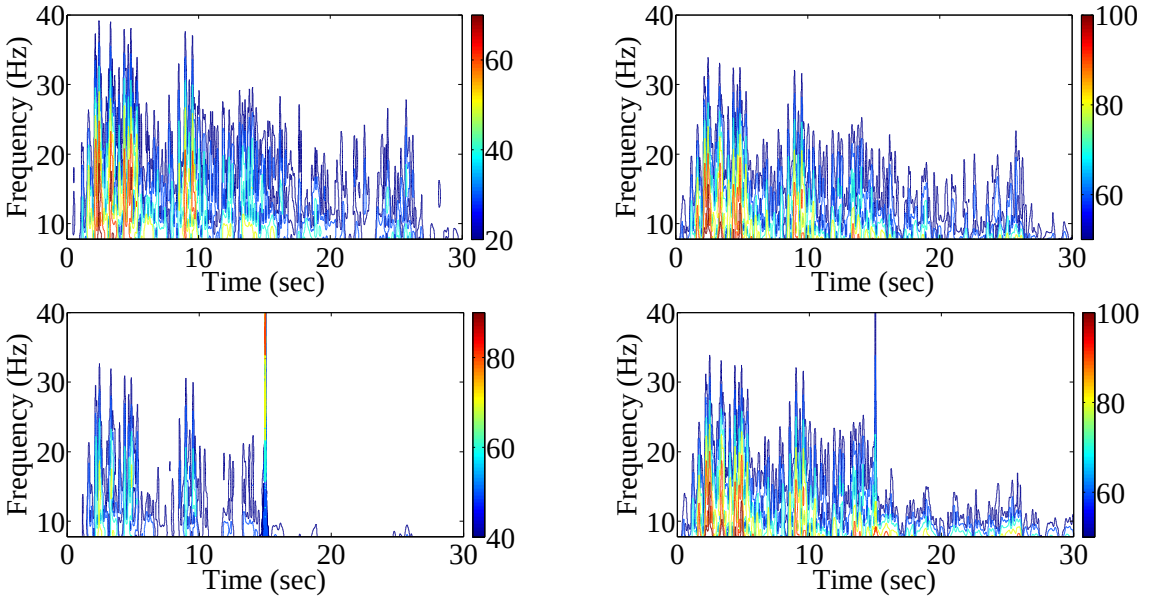

Figure 35. Wavelet scalograms of $\ddot{u}_3$ and $\ddot{u}_4$ (left column is for $\ddot{u}_3$, right column is for $\ddot{u}_4$; upper row is for undamaged; lower row is for damaged)

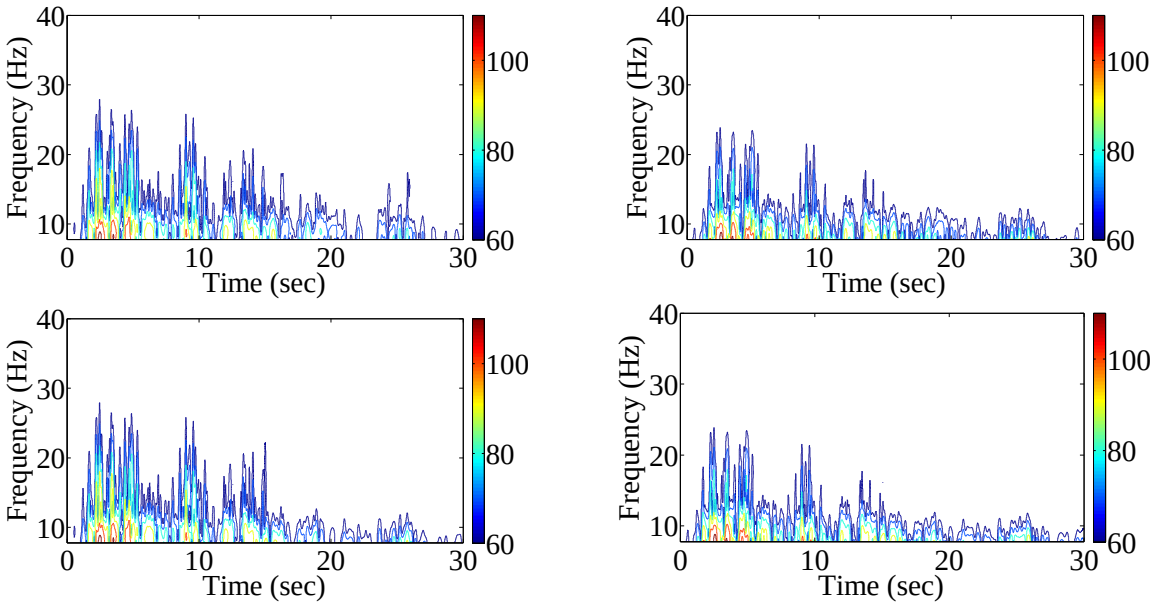

Figure 36. Wavelet scalograms of $\ddot{u}_7$ and $\ddot{u}_{13}$ (left column is for $\ddot{u}_7$, right column is for $\ddot{u}_{13}$; upper row is for undamaged; lower row is for damaged)

REFERENCES

[1] K.F. Tee, C.G. Koh, S.T. Quek, Numerical and experimental studies of a substructural identification strategy, *Structural Health Monitoring* 8 (2009) 397-410.

[2] C.G. Koh, K. Shankar, Substructural identification method without interface measurement, *ASCE Journal of Engineering Mechanics* 129 (2003) 769-776.

[3] C.G. Koh, B. Hong, C.Y. Liaw, Substructural and progressive structural identification methods, *Engineering Structures* 25 (2003) 1551-1563.

[4] C.B. Yun, H.J. Lee, Substructural identification for damage estimation of structures, *Structural Safety* 19 (1997) 121-140.

[5] S. Sandesh, K. Shankar, Time domain identification of structural parameters and input time history using a substructural approach, *International Journal of Structural Stability and Dynamics* 9 (2009) 243-265.

[6] D. Giagopulos, S. Natsiavas, Hybrid (numerical-experimental) modeling of complex structures with linear and nonlinear components, *Nonlinear Dynamics* 47 (2007) 193-217.

[7] S.L. Chen, M. Geradin, Dynamic force identification for beamlike structures using an improved dynamic stiffness method, *Shock and Vibration* 3 (1996) 183-191.

[8] S.L. Chen, M. Geradin, E. Lamine, An improved dynamic stiffness method and modal analysis for beam-like structures, *Computers & Structures* 60 (1996) 725-731.

[9] S. Weng, Y. Xia, Y.L. Xu, X.Q. Zhou, H.P. Zhu, Improved substructuring method for eigensolutions of large-scale structures, *Journal of Sound and Vibration* 323 (2009) 718-736.

[10] K.C. Park, G.W. Reich, K.F. Alvin, Structural damage detection using localized flexibilities, *Journal of Intelligent Material Systems and Structures* 9 (1998) 911-919.

[11] P.S. Skjaeraek, S.R.K. Nielsen, A.S. Cakmak, Identification of damage in reinforced concrete structures from earthquake records - Optimal location of sensors, *Soil Dynamics and Earthquake Engineering* 15 (1996) 347-358.

[12] M. Okuma, W. Heylen, H. Matsuoka, P. Sas, Identification and prediction of frame structure dynamics by spatial matrix identification method, *Journal of Vibration and Acoustics* 123 (2001) 390-394.

[13] T.J. Su, J.N. Juang, Substructure system-identification and synthesis, *Journal of Guidance Control and Dynamics* 17 (1994) 1087-1095.

[14] K.V. Yuen, S.K. Au, J.L. Beck, Two-stage structural health monitoring approach for phase I benchmark studies, *ASCE Journal of Engineering Mechanics* 130 (2004) 16-33.

[15] K.V. Yuen, J.L. Beck, L.S. Katafygiotis, Unified probabilistic approach for model updating and damage detection, *Journal of Applied Mechanics-Transactions of the ASME* 73 (2006) 555-564.

[16] K.V. Yuen, L.S. Katafygiotis, Substructure identification and health monitoring using noisy response measurements only, *Computer-Aided Civil and Infrastructure Engineering* 21 (2006) 280-291.

[17] A. Oreta, T. Tanabe, Element identification of member properties of framed structures, *ASCE Journal of Structural Engineering* 120 (1994) 1961-1975.

[18] C.G. Koh, L.M. See, T. Balendra, Estimation of structural parameters in time domain - a substructure approach, *Earthquake Engineering & Structural Dynamics* 20 (1991) 787-801.

[19] K.F. Tee, C.G. Koh, S.T. Quek, Substructural first- and second-order model identification for structural damage assessment, *Earthquake Engineering & Structural*

Dynamics 34 (2005) 1755-1775.

[20] H.W. Huang, J.N. Yang, Damage identification of substructure for local health monitoring, *Smart Structures and Systems* 4 (2008) 795-807.

[21] N. Bakhary, H. Hao, A.J. Deeks, Structure damage detection using neural network with multi-stage substructuring, *Advances in Structural Engineering* 13 (2010) 95-110.

[22] Z.S. Wu, B. Xu, K. Yokoyama, Decentralized parametric damage detection based on neural networks, *Computer-Aided Civil and Infrastructure Engineering* 17 (2002) 175-184.

[23] B. Xu, Time domain substructural post-earthquake damage diagnosis methodology with neural networks, *Lecture Note in Computer Science* 3611 (Part II) (2005) 520-529.

[24] C.B. Yun, J.H. Yi, E.Y. Bahng, Joint damage assessment of framed structures using a neural networks technique, *Engineering Structures* 23 (2001) 425-435.

[25] E.J. Rothwell, K.M. Chen, D.P. Nyquist, An adaptive-window-width short-time Fourier transform for visualization of radar target substructure resonances, *IEEE Transactions on Antennas and Propagation* 46 (1998) 1393-1395.

[26] X.H. Ma, A.F. Vakakis, Karhunen-Loeve decomposition of the transient dynamics of a multibay truss, *AIAA Journal* 37 (1999) 939-946.

[27] P. Sjovall, T. Abrahamsson, Substructure system identification from coupled system test data, *Mechanical Systems and Signal Processing* 22 (2008) 15-33.

[28] K. Sholeh, A. Vafaie, A. Kaveh, Localized identification of shear building with embedded foundation in frequency, *Structural Design of Tall and Special Buildings* 17 (2008) 245-256.

[29] C. Gontier, M. Bensaibi, Time-domain identification of a substructure from in-situ

analysis of the whole structure, *Mechanical Systems and Signal Processing* 9 (1995) 379-396.

[30] H. Fang, T.J. Wang, A new method for nondestructive damage identification of lattice materials, *Science in China Series E-Technological Sciences* 52 (2009) 1293-1300.

[31] W.J. Kim, B.Y. Lee, Y.S. Park, Non-linear joint parameter identification using the frequency response function of the linear substructure, *Proceedings of the Institution of Mechanical Engineers Part C-Journal of Mechanical Engineering Science* 218 (2004) 947-955.

[32] P.L. Liu, C.C. Chian, Parametric identification of truss structures using static strains, *ASCE Journal of Structural Engineering* 123 (1997) 927-933.

[33] P.L. Liu, C.C. Chen, Parametric identification of frame structures using transient strains, *Chinese Journal of Mechanics-Series A* 16 (2000) 217-225.

[34] N.G. Park, Y.S. Park, Identification of damage on a substructure with measured frequency response functions, *Journal of Mechanical Science and Technology* 19 (2005) 1891-1901.

[35] W.J. Kim, Y.S. Park, Nonlinear joint parameter-identification by applying the force-state mapping technique in the frequency-domain, *Mechanical Systems and Signal Processing* 8 (1994) 519-529.

[36] D.H. Lee, W.S. Hwang, An identification method for joint structural parameters using an FRF-based substructuring method and an optimization technique, *Journal of Mechanical Science and Technology* 21 (2007) 2011-2022.

[37] T.C. Yang, S.H. Fan, C.S. Lin, Joint stiffness identification using FRF measurements, *Computers & Structures* 81 (2003) 2549-2556.

[38] S.S. Park, J. Chae, Joint identification of modular tools using a novel receptance coupling method, *International Journal of Advanced Manufacturing Technology* 35 (2008) 1251-1262.

[39] M. Taazount, C. Pluquin, J. Renard, A. Bouazzouni, Dynamic identification of junction forces by discrete time identification methods, *International Journal for Multiscale Computational Engineering* 6 (2008) 123-140.

[40] A. Ovanesova, L.E. Suarez, Applications of wavelet transforms to damage detection in frame structures, *Engineering Structures* 26 (2004) 39-49.

[41] M. Rucka, K. Wilde, Application of continuous wavelet transform in vibration based damage detection method for beams and plates, *Journal of Sound and Vibration* 297 (2006) 536-550.

[42] W.L. Bayissa, N. Haritos, S. Thelandersson, Vibration-based structural damage identification using wavelet transform, *Mechanical Systems and Signal Processing* 22 (2008) 1194-1215.

[43] G. Welch, G. Bishop, An Introduction to the Kalman Filter, *UNC-Chapel Hill TR 95-041*, University of North Carolina at Chapel Hill, Chapel Hill, NC, 1995.

[44] A.M. Yan, P. De Boe, J.C. Golinval, Structural damage diagnosis by Kalman model based on stochastic subspace identification, *Structural Health Monitoring* 3 (2004) 103-119.

[45] J.N. Yang, S. Lin, H. Huang, L. Zhou, An adaptive extended Kalman filter for structural damage identification, *Structural Control and Health Monitoring* 13 (2006) 849 – 867.

[46] M. Hoshiya, E. Saito, Structural identification by extended Kalman filter, *ASCE*

Journal of Engineering Mechanics 110 (1984) 1757-1770

[47] A.H. Jazwinski, *Stochastic Processes and Filtering Theory*, Academic Press, New York, 1970.

[48] Y. Geng, J. Wang, Adaptive estimation of multiple fading factors in Kalman filter for navigation applications, *GPS Solutions* 12 (2008) 273-279.

[49] P.S. Maybeck, Stochastic models, estimation, and control, 1979.

[50] S.L. Fagin, Recursive linear regression theory, optimal filter theory, and error analysis of optimal system, *IEEE International Convention Record* (1964) 216-240.

[51] Q. Xia, M. Rao, Y. Ying, X. Shen, Adaptive fading Kalman filter with an application, *Automatica* 30 (1994) 1333-1338.

[52] A.K. Chopra, *Dynamics of Structures: Theory and Applications to Earthquake Engineering*, second ed., Prentice Hall, Upper Saddle River, NJ, 2001.

[53] R.W. Clough, J. Penzien, *Dynamics of structures*, second revised ed., Computers and Structures, Inc., Berkeley, CA, 2003.

[54] N.M. Newmark, A method of computation for structural dynamics, *ASCE Journal of the Engineering Mechanics Division* 85 (1959) 67-94

[55] J. Chen, J. Li, Simultaneous identification of structural parameters and input time history from output-only measurements, *Computational Mechanics* 33 (2004) 365-374.

[56] Z.K. Peng, F.L. Chu, Application of the wavelet transform in machine condition monitoring and fault diagnostics: a review with bibliography, *Mechanical Systems and Signal Processing* 18 (2004) 199-221.

[57] K. Gurley, A. Kareem, Applications of wavelet transforms in earthquake, wind and ocean engineering, *Engineering Structures* 21 (1999) 149-167.

[58] S.-T. Quek, Q. Wang, L. Zhang, K.-K. Ang, Sensitivity analysis of crack detection in beams by wavelet technique, *International Journal of Mechanical Sciences* 43 (2001) 2899-2910.

[59] E. Douka, S. Loutridis, A. Trochidis, Crack identification in beams using wavelet analysis, *International Journal of Solids and Structures* 40 (2003) 3557-3569.

[60] M. Rucka, K. Wilde, Application of continuous wavelet transform in vibration based damage detection method for beams and plates, *Journal of Sound and Vibration* 297 (2006) 536-550.

[61] C.-C. Chang, L.-W. Chen, Damage detection of a rectangular plate by spatial wavelet based approach, *Appplied Acoustics* 65 (2004) 819-832.

[62] E. Douka, S. Loutridis, A. Trochidis, Crack identification in plates using wavelet analysis, *Journal of Sound and Vibration* 270 (2004) 279-295.

[63] A.V. Ovanesova, L.Z. Suarez, Applications of wavelet transforms to damage detection in frame structures, *Engineering Structures* 26 (2004) 39-49.

[64] Z. Hou, M. Noori, R.S. Amand, Wavelet-based approach for structural damage detection, *ASCE Journal of Engineering Mechanics* 126 (2000) 677-683.

[65] S.G. Mallat, *A Wavelet Tour of Signal Processing*, second ed., Academic Press, San Diego, 1999.

[66] C.C. Liu, Z. Qiu, A method based on Morlet wavelet for extracting vibration signal envelope, *Proceedings of the fifth International Conference on Signal Processing*, 2000, 337-340.

[67] J. Lin, L. Qu, Feature extraction based on morlet wavelet and its application for mechanical fault diagnosis, *Journal of Sound and Vibration* 234 (2000) 135-148.

[68] Y.-T. Sheen, C.-K. Hung, Constructing a wavelet-based envelope function for vibration signal analysis, *Mechanical Systems and Signal Processing* 18 (2004) 119-126.

[69] A. Teolis, *Computational Signal Processing with Wavelets*, first ed., Birkhäuser, Boston, 1998.

CHAPTER IV [1]

DELAMINATION DETECTION IN REINFORCED CONCRETE DECKS BY MODAL IDENTIFICATION FROM OUTPUT-ONLY VIBRATION DATA

ABSTRACT

To study the feasibility of delamination detection by using structural health monitoring system, this study addresses delamination detection of concrete slabs by analyzing the global dynamic responses measured by vibration sensors. Numerical as well as experimental studies are carried out. In the numerical examples, delaminations with different sizes and locations are introduced into a concrete slab, the effects of presence, sizes, and locations of delaminations on the modal frequencies and mode shapes of the concrete slab are studied. In the experimental portion of the study, four concrete deck specimens with different delamination sizes were constructed and experimental tests were conducted in the laboratory. Traditional peak-picking (PP), frequency domain decomposition (FDD), and stochastic subspace identification (SSI) methods were applied to the modal identification from real measurements of dynamic velocity responses. The modal parameters identified by these three methods correlated well. The changes in modal frequencies, damping ratios and mode shapes that were extracted from the dynamic measurements were investigated and correlated to the actual delaminations and can indicate presence and severity of delamination. Finite element (FE) models of reinforced concrete decks with different delamination sizes and locations were established. The modal parameters computed from the FE models were compared to those obtained from the laboratory specimens and the FE models were validated.

---

[1] Coauthored by Shutao Xing, Marvin W. Halling, and Paul J. Barr

1. Introduction

Delamination in concrete bridge decks decouples the concrete from its surrounding rebar, resulting in the loss of structural strength and facilitates a rapid deterioration of the deck [1]. The delamination impairs both the appearance and the serviceability of the structure, and repairs can be very costly. It is estimated that annual corrosion related maintenance and repair costs for concrete infrastructure approaches $100 billion worldwide [2-3]. Corrosion and delamination are of great concern for bridges and routine inspection is necessary. Many methods have been developed to detect concrete delamination. These methods include the conventional chain drag method, impact-echo, ultra-sonic tests, ground penetrating radar, imaging radar and infrared thermography [1, 4]. Efforts have been made to expand, improve, and combine currently available techniques. These inspection and detection methods require the deployment of professional people with devices to field sites and can be very costly. With the expansion of structural health monitoring systems, increasing numbers of real-time monitoring systems are being deployed on actual bridges and buildings. Taking advantage of permanently installed sensors could be useful in delamination detection. Vibration sensors can be flexibly deployed and located in-situ for long term monitoring applications that include delamination detection.

Various analytical, numerical, and experimental studies have addressed delamination detection in composite structures from the measurements by vibration sensors through vibration-based identification methods. Zhou et al. [5] provided a review of vibration based model-dependent delamination identification for composite structures. Valdes and Soutis [6] conducted experiments to study the effects of delamination in

laminated beams on the changes in modal frequencies. Ratcliffe and Bagaria [7] used curvature mode shapes to locate delaminations in a composite beam. Wei et al. [8] evaluated delamination of multilayer composite plates using model-based neural networks. When the delaminated-induced changes in modal characteristics are too small to be identified, the wavelets methods are considered, which have been used effectively [9-11] to detect small damages. Yan and Yam [12] employed energy distribution of dynamic responses decomposed by wavelet analysis to detect the delaminations in composite plates and reported that this method is capable of detecting localized damage. Among these studies, most are on simple composite structures such as beams, with very few, if any, studies performed on plates.

For civil engineering concrete structures, studies on delamination detection by using vibration sensors are very rare. Xing et al. [13] investigated delamination detection by using vibration measurements for civil engineering concrete plates through numerical studies. In this numerical study, finite element models of the concrete plates were modeled using ANSYS. The modal analyses and dynamic analyses were performed for examination of the delamination parameters on the modal characteristics of the models. The effectiveness of using changes in modal frequencies and mode shapes as damage indicators of the delamination were studied.

The current study presents an expansion of the previous numerical studies [14] with a more complete parameter study. Additionally, experimental studies of four reinforced concrete slabs with different delamination areas were tested dynamically to verify the numerical results. Delaminations were simulated by embedding plexiglass inside the concrete plates during casting. The dynamic tests were conducted

approximately four months after placement of the concrete. The experiments were original and significant since the models were relatively large scale concrete plates (bridge deck). Initial experimental results were discussed in [14] and a more comprehensive study is addressed in this paper. No similar experimental testing was encountered in the literature.

The primary purpose of this study is to investigate the applicability of delamination detection of concrete plates by modal identification using output-only measurements. The fundamental principle is that the delaminations decrease the stiffness and consequently the modal frequencies. Additionally, the damping is changed and mode shapes become irregular, the amplitude of the delamination area is changed. Taking advantage of the changes in modal characteristics can avoid dealing with the complicated delamination mechanism, such as the random development and irregular patterns.

After numerical studies of several finite element models, the experiments were conducted. The experimental testing consisted of dynamic tests using random, swept sine, and impact excitation sources. The dynamic response results due to these excitations are presented to provide reference for output only systems (ambient vibration). Modal frequencies, modal damping ratios, and mode shapes were extracted from the measured velocity responses. The differences in modal characteristics between the various delaminated models were compared and indicated presence and severity of delaminations. Finite element models of the concrete slabs were also established using ANSYS software. It must be pointed out that the modeling included the effects of non-ideal boundary conditions. The concrete, steel reinforcement, wood supports, delaminations and boundary conditions were included in the model. The modal characteristics computed

from the finite element models were compared with those from dynamic tests for validation. The finite element results could be used as reference for modal identification from dynamic response measurements.

2. Modal Identification Methods used in this Study

Three identification methods are used in this study. They are classical peak-picking, frequency domain decomposition and stochastic subspace identification methods. In the classical peak-picking method (PP), the simple signal processing technique computes the power spectra of time histories measurements by discrete Fourier transform and directly uses the peaks of the spectra to determine modal frequencies. Frequency Domain Decomposition (FDD) and Stochastic Subspace Identification (SSI) methods were also adopted to extract modal characteristics from measurements of the dynamic tests. These identification methods were compared with each other.

For the cases of lightly damped structures, Brincker et al. [15] derived a relationship between response spectral density and modal parameters, which provide a basis for FDD method. In application of FDD identification algorithm [15], first the power spectral density (PSD) of the output measurements $\hat{G}_{yy}(j\omega)$ are estimated and then decomposed at $\omega = \omega_i$ by taking the Singular Value Decomposition (SVD) of the PSD matrix.

$$\hat{G}_{yy}(j\omega_i) = U_i S_i U_i^H \tag{109}$$

where the unitary matrix $U_i = [u_{i1}, u_{i2}, ..., u_{im}]$ holds the singular vectors u_{ij} and the diagonal matrix S_i holds the singular values s_{ij}. If only a kth mode is dominating at the selected frequency ω_i, there will be only one singular value in Eq. (109) and therefore the

first singular vector u_{i1} would be an estimate of the kth mode shape, $\hat{\phi} = u_{i1}$. Damping can be obtained from the correlation function of the SDOF system [16].

Stochastic subspace identification (SSI) method is a time-domain identification method originally proposed in [17] and has been applied effectively in various types of civil and mechanical structures. This method can obtain linear models from column and row spaces of the matrices computed from the input-output data [18]. This study used Data-driven SSI that does not need the computation of output covariance. The key idea of data-driven SSI is to project the row space of future outputs into the row space of the past outputs. An extension of the SSI method, called reference-based SSI, was developed in [19].

The discrete-time stochastic state-space model is defined as the normal model without input terms [20],

$$x_{k+1} = Ax_k + w_k; \qquad y_k = Cx_k + v_k \tag{110}$$

where w and v are plant and observation noise vectors respectively, both of them are zero mean Gaussian white noise vectors. The SSI is used to identify A and C from the output-only measurements y_k. The identification steps in this study are concisely summarized in the following, for details refer to the literature [18-19].

(a) Construct Hankel matrix Y from the output measurements:

$$Y_{0|2i-1} = \left[\begin{array}{cccc} y_0 & y_1 & \cdots & y_{j-1} \\ y_1 & y_2 & \cdots & y_j \\ \cdots & \cdots & \cdots & \cdots \\ y_{i-1} & y_i & \cdots & y_{i+j-2} \\ \hline y_i & y_{i+1} & \cdots & y_{i+j-1} \\ y_{i+1} & y_{i+2} & \cdots & y_{i+j} \\ \cdots & \cdots & \cdots & \cdots \\ y_{2i-1} & y_{2i} & \cdots & y_{2i+j-2} \end{array}\right] = \left[\begin{array}{c} Y_{0|i} \\ \hline Y_{i|2i-1} \end{array}\right] = \left[\begin{array}{c} Y_P \\ \hline Y_f \end{array}\right] \tag{111}$$

The Hankel matrix is a matrix that has the same elements in every antidiagonal. It has 2i block rows and j columns and is divided into two parts, the past output Y_p and the future output Y_f, each part has i block rows, i must be greater than the system order n. The system order n is equal to the number of modes identified by the SSI method. Let ny denote the number of time samples of output y_k, to guarantee y_k populate Hankel matrix, use j = ny-2i+1. If the measurements used in the SSI method contain l degrees of freedom, then y_k has l rows.

(b) Orthogonally project the row space of future outputs Y_f on the row space of past outputs Y_p:

$$T_i = Y_f Y_p^T (Y_p Y_p^T)^\dagger Y_p \tag{112}$$

where $^{T, \dagger}$ denote transpose and pseudoinverse respectively.

(c) Then apply SVD to the orthogonal projection:

$$T_i = USV^T = \begin{pmatrix} U_1 & U_2 \end{pmatrix} \begin{pmatrix} S_1 & 0 \\ 0 & S_2 \end{pmatrix} \begin{pmatrix} V_1^T \\ V_2^T \end{pmatrix} \approx U_1 S_1 V_1^T \tag{113}$$

where U and V are orthonormal matrices, S is a diagonal matrix containing singular values in descending order, among which S_2 is a block containing small neglected values.

(d) Calculate the extended observability matrix from the reduced SVD from Eq. (113)

$$O_i = U_1 S_1^{1/2} \tag{114}$$

The definition of this observability matrix O_i is:

$$O_i = \begin{pmatrix} C & CA & \cdots & CA^{i-1} \end{pmatrix}^T \tag{115}$$

Then the discrete-time system matrices A and C can be calculated from Eq. (114) - (115).

(e) Post-processing to extract modal parameters.

Calculate the eigenvalues and eigenvectors of matrix A. $A = \psi \Lambda \psi^{-1}$, where

$\Lambda = diag(\lambda_q)$ is a diagonal matrix containing the discrete time complex eigenvalues and columns of ψ are the corresponding eigenvectors. For continuous time system, the state matrices $A_C = \psi_C \Lambda_C \psi_C^{-1}$, after some derivations, it gives,

$$A = e^{A_C \Delta t};\ \psi_C = \psi;\ \ \lambda_{C_q} = \frac{\ln(\lambda_q)}{\Delta t};\ \lambda_{C_q}, \lambda^*_{C_q} = -\xi_q \omega_q \pm j\omega_q \sqrt{1-\xi_q^2};\ \Phi = C\psi \qquad (116)$$

where Δt is time step, ω_q is modal frequency, ξ_q is modal damping ratio, the columns of Φ are mode shapes.

In processing the real measurements, it usually results in complex frequencies and mode shapes, for light damping, we use the amplitudes of complex mode shape with signs of the corresponding real parts to draw them as real mode shapes.

3. Numerical Studies

In this section, a finite element model of a reinforced concrete plate was created and then several delaminations of various sizes and locations were introduced into the model, separately. The modal and dynamic analyses were performed on the model and the effects of delamination on modal characteristics of the reinforced concrete finite element model were studied to provide useful reference for further numerical studies as well as for the future laboratory experiments to be presented in section 4.

3.1 Description of the numerical examples

The reinforced concrete plate of the numerical studies is illustrated in Figure 37. The width a = 4 m along the X direction, the length b = 6 m along the Z direction and thickness h =0.2 m along the Y direction, the origin is defined at the bottom corner node; the coordinate system is shown in Figure 37(a). The concrete's elastic modulus is E_c =

33,000 MPa, Poisson's ratio ν_c = 0.2, ultimate uniaxial compressive strength σ_c = 25.5 MPa, ultimate uniaxial tensile strength σ_t = 2.56 MPa, and density ρ_c = 2450 kg/m^3. The steel rebar's size is #6, nominal diameter d = 19 mm, elastic modulus E_s = 200 GPa, yield stress f_y = 410 MPa; Poisson's ratio ν_s = 0.3; and the density ρ_s = 7850 kg/m^3. Two layers of steel rebar are placed in the concrete plate at the horizontal planes of Y = 0.05 m and Y = 0.15 m and rebar are along both X and Z directions as exhibited in Figure 37 (b). The space between all adjacent rebar is 0.2 m on center. The concrete plate is simply supported at the two opposite edges X = 0 m and X = 4 m and free at the other two opposite edges Z = 0 m and Z = 6 m.

3.2 Finite element modeling

The finite element software package, ANSYS, was used to perform the finite element modeling. Solid65 and link8 elements were selected to represent concrete and steel rebar, respectively. Solid65 elements have eight nodes with three translational degrees of freedom at each node. The 3-D spar, Link8, element is a uniaxial tension-compression element with three translational degrees of freedom at each node [21]. In this paper, all analyses were restricted to linear elastic response and the elements were configured accordingly.

Delamination was modeled using a similar method to [22]. First, two separate decks that were located above and below the delamination plane were attached together. The nodes in the undelaminated area were declared as coupled nodes utilizing coupling/constraint equations and the nodes in delaminated area were uncoupled. The delamination locations and areas were adjusted for different damage degrees. All the delaminations were on the XZ plane at a vertical elevation of Y equal to 0.15 m, which

was purposely to simulate a bridge deck in which delamination often occurs in a horizontal plane at the top layer of steel reinforcement. In the following sections, the ratio of delamination area over total area A_{delam}/A_{tot} is used to denote severity of delamination.

3.3 Modal frequencies validation of the finite element models

The analytical solutions for the natural frequencies were computed to validate the modeling. For convenience of using the analytical formula from [23], the Poisson's ratio of the concrete was changed to $\nu_c = 0.3$. The other parameters have same meanings and take same values as those in section 3.2. In order to use the analytical solution, the equivalent elastic modulus and density was used, which were computed as follows

$$E(A_c + A_s) = E_c A_c + E_s A_s \tag{117}$$

$$\rho(V_c + V_s) = \rho_c V_c + \rho_s V_s \tag{118}$$

where E is the equivalent elastic modulus, ρ is the equivalent density, V_c is volume of concrete, V_s is volume of steel rebar.

Since minimum of (a, b)/h is equal to 1/20, it can be analyzed as thin plate and Kirchhoff assumptions are applicable. The analytical method follows [23]. The governing equation is,

$$D\nabla^4 w + \rho \frac{\partial^2 w}{\partial t^2} = 0 \tag{119}$$

where w is transverse deflection, ∇^4 is biharmonic differential operator in rectangular coordinates, $D = Eh^3/12(1-\nu^2)$ $D = Eh^3/12(1-\nu^2)$ is the flexural rigidity. The boundary conditions for the simply-supported and free edges are Eq. (120) and (121) accordingly

$$w = 0; \qquad \frac{\partial^2 w}{\partial x^2} + \nu \frac{\partial^2 w}{\partial z^2} = 0 \tag{120}$$

$$\frac{\partial^2 w}{\partial x^2} + \nu \frac{\partial^2 w}{\partial z^2} = 0; \qquad \frac{\partial^3 w}{\partial x^3} + (2 - \nu) \frac{\partial^3 w}{\partial x \partial z^2} = 0 \tag{121}$$

Combining Eq. (119)-(121), characteristic equations that can numerically solved by Newton's method to yield the frequency parameter can be written as

$$\lambda = \omega a^2 \sqrt{\rho / D} \tag{122}$$

Eq. (122) can be used to calculate the natural frequencies.

The comparison results are listed in Table 19. The percent differences are within 3.4% for the first five frequencies, the difference for the first frequency is only 0.18%, and the difference for the seventh and eighth frequencies are also very small. It is shown that most frequencies by analytical solution were a little larger than those by modeling. This is reasonable, because thin plate theory usually overestimates the natural frequencies [24], and Mindlin plate theory would be more accurate for a thick plate. Therefore, based on the results, it was concluded that the finite element model accurately produced the correct modal frequencies.

3.4 Modal analysis of the finite element models

The modal analysis was carried out to correlate the delamination with modal characteristics. The analysis was confined to the first six modes. Table 20 provides the sizes and locations for the delamination cases of this study, and they are illustrated in Figure 38.

Table 21 shows the comparisons of modal frequencies of the undamaged model and those of different delaminated models. Figure 39 graphically shows the comparisons

of the mode shapes of the undelaminated model with those of delaminated models, the amplitudes in all the figures have been scaled using the same factor. The modal order is the sub number in the figures plus one for this analysis. More plots of mode shape can be found in the Appendix.

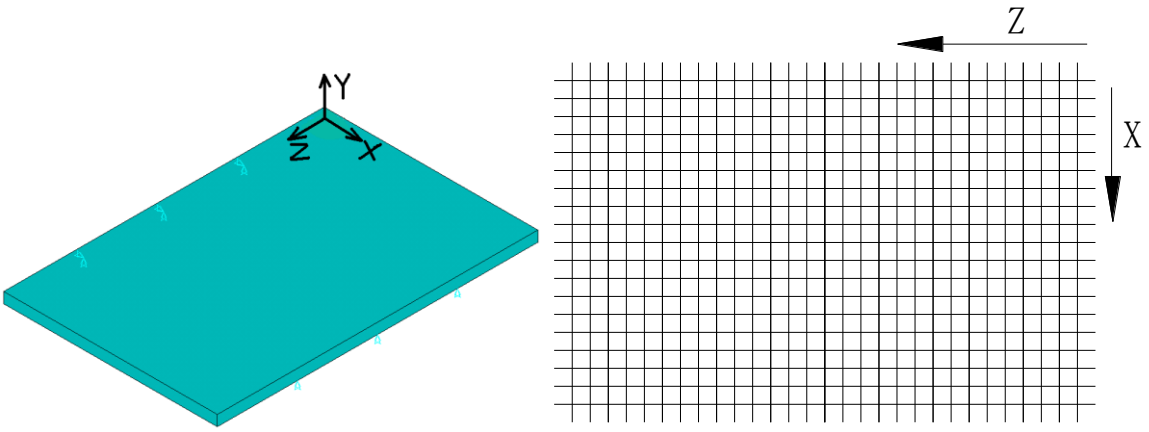

(a) (b)

Figure 37. The concrete slab model for the numerical examples: (a) isometric view the concrete model (b) plan view of the steel rebar in the concrete.

Table 19. Comparison of frequencies by analytical and finite element model for numerical example.

Mode	1	2	3	4	5	6	7	8
Analytical Solution	20.87	27.94	49.40	84.16	86.86	91.87	116.74	142.54
ANSYS Solution	20.91	27.06	50.22	81.31	85.55	86.16	116.69	139.50
Difference (%)	0.18	-3.14	1.65	-3.39	-1.50	-6.21	-0.04	-2.13

Table 20. The locations and sizes of the delaminated areas for numerical example.

Delamination	1/12	1/6	1/4	1/3 (unsymmetrical)	1/3 (symmetrical)	1/2
X range (m)	2.5~3.5	0~4	1.5~3.5	0~2	1~3	1~3
Z range (m)	1~3	1~2	1~4	1~5	1~5	0~6
Y coordinate (m)	0.15	0.15	0.15	0.15	0.15	0.15

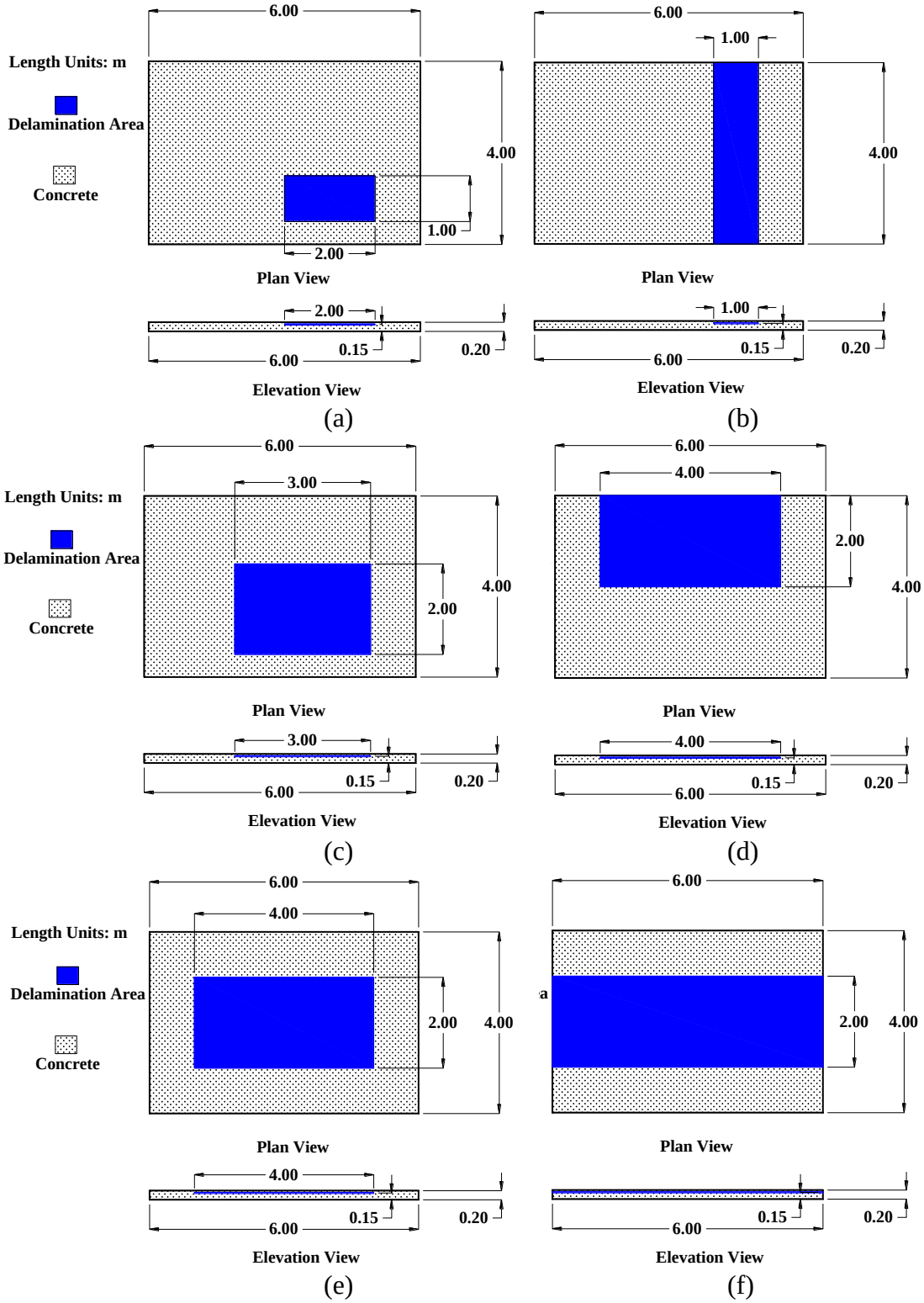

Figure 38. The locations of delamination areas for the numerical examples: (a) 1/12-delaminated; (b) 1/6-delaminated; (c) 1/4-delaminated; (d) 1/3-unsymmetrical-delaminated; (e) 1/3-unsymmetrical-delaminatedl; (f) 1/2-delaminated models.

Table 21. Comparison of natural frequencies of the un-delaminated and delaminated concrete decks for numerical example.

Mode	Un-delaminated	1/12 Delaminated		1/6 Delaminated		1/4 Delaminated	
	Freq (HZ)	Freq (HZ)	Difference (%)	Freq (HZ)	Difference (%)	Freq (HZ)	Difference (%)
1	20.60	20.53	-0.30	20.42	-0.86	20.34	-1.23
2	27.16	27.09	-0.25	26.80	-1.31	26.58	-2.11
3	50.12	49.75	-0.73	49.12	-2.00	44.33	-11.55
4	79.85	79.45	-0.49	76.87	-3.73	53.75	-32.68
5	84.55	83.50	-1.24	82.51	-2.41	70.45	-16.68
6	85.35	84.94	-0.48	83.36	-2.33	75.53	-11.50

The difference in this table is: $\frac{\text{delaminated frequency-undelaminated frequency}}{\text{undelaminated frequency}} \times 100\%$

Table 21. Cont'd

Mode	1/3 Delaminated unsymmetrical		1/3 Delaminated symmetrical		1/2 Delamination	
	Freq (HZ)	Difference (%)	Freq (HZ)	Difference (%)	Freq (HZ)	Difference (%)
1	14.78	-28.24	20.35	-1.18	20.04	-2.70
2	19.43	-28.43	26.22	-3.44	25.08	-7.65
3	25.92	-48.29	41.37	-17.46	38.31	-23.56
4	34.24	-57.11	53.55	-32.93	42.42	-46.87
5	44.53	-47.33	56.12	-33.63	44.40	-47.49
6	52.64	-38.32	67.94	-20.39	49.00	-42.58

Based on the frequency variation listed in Table 21, it is noted that the higher the modal order is, the larger the reduction of the modal frequency is. The changes in the 4^{th} modal frequency are more apparent than their neighboring modes, which indicate that specific modes are more sensitive to delamination than other modes. Table 21 shows that the bigger the delamination areas, the bigger percentage reduction of the corresponding

frequencies. It is also concluded that if $A_{delam}/A_{tot} > 1/6$, the first two natural frequencies can indicate the delamination quite well with frequency difference from 1.18% to 28.43% between undelaminated and the delaminated models. For $A_{delam}/A_{tot} = 1/6$, the 2% frequency difference of 3rd mode can indicate delamination. However, when $A_{delam}/A_{tot} = 1/12$, even higher frequencies are not sensitive to delamination, e.g., frequency variation of the 4th order is only 0.49%.

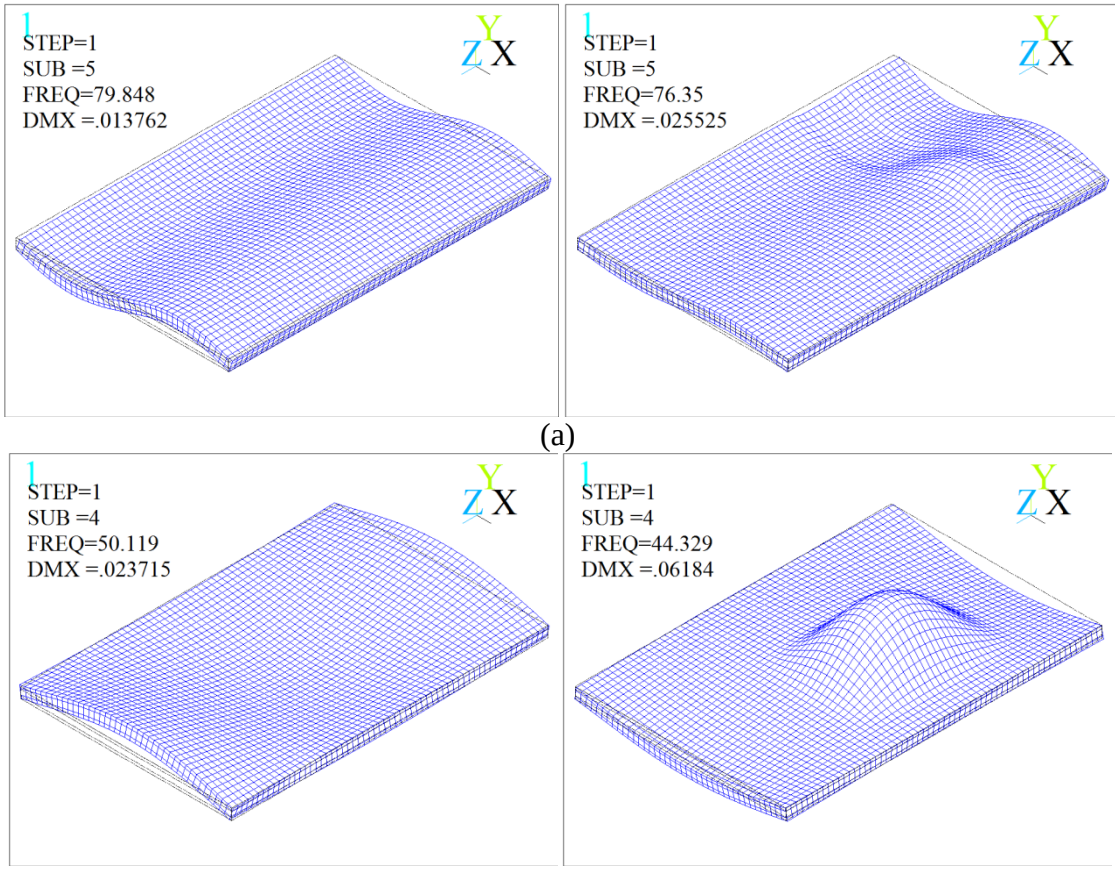

Figure 39. Typical comparisons of the mode shapes: (a) the 4th mode shapes for the un-delaminated (left) and 1/6 delaminated models (right); (b) The 3rd mode shapes for the un-delaminated (left) and 1/4 delaminated (right).

Similar trends were found to be present in the mode shapes shown in Figure 39 and Figure 40. While the mode shapes are more sensitive to the delamination and are able to show the location from the irregular curves of those delaminated mode shapes. Comparing the delamination locations in Table 20 with the mode shapes in Figure 39 and Figure 40, the irregular parts correspond almost exactly to the delamination.

In Table 21, the comparisons of frequencies of 1/3 delaminated models at unsymmetrical and symmetrical locations indicate that unsymmetrical delamination reduces the modal frequencies more significantly than the symmetrical delamination, e.g., the difference between the 1st frequencies of 1/3 symmetrical delaminated and un-delaminated models is only 1.18% and it increases to 28.24% between 1/3 unsymmetrical and un-delaminated models. This is also demonstrated by the mode shapes in Figure 40, in which the 1st mode shape of the 1/3 unsymmetrical delaminated model is more irregular and has larger magnitude than that of the 1/3 symmetrical delaminated model.

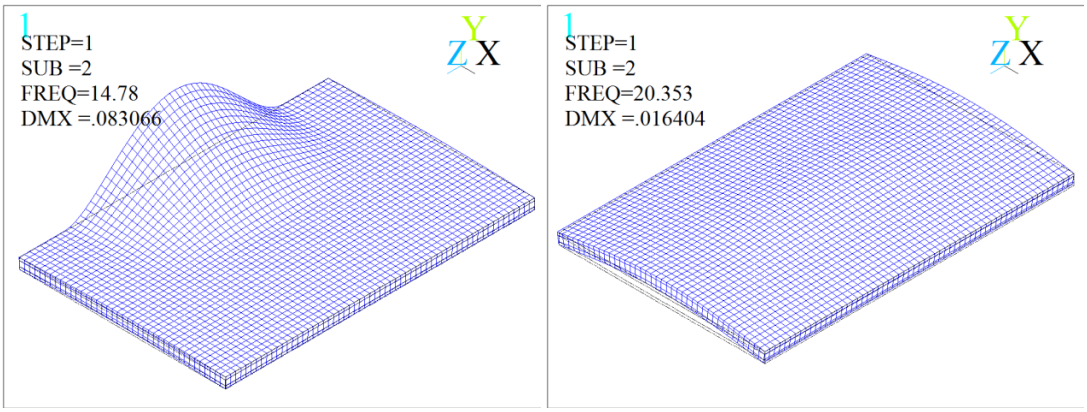

Figure 40. Comparison of the 1st mode shapes of the 1/3-delaminated models with unsymmetrical (left) and symmetrical (right) locations with respect to the total area.

3.5 Modal identification from dynamic responses (numerical study)

In the numerical study, the modal characteristics were extracted from the dynamic responses. To identify the delamination from the acceleration response, the modeled concrete slab was excited with three types of excitations. Swept sine excitation, impulse excitation and random excitation were applied to a point at the top surface of the reinforced concrete plate to generate dynamic responses. Modal frequencies were then identified from the ambient vibrations by using the peak-picking method. Figure 41 shows the time histories of acceleration responses and the corresponding single-Sided amplitude spectra computed by FFT for the undelaminated and 1/4 delaminated models respectively. The inputs are the same swept sine for both undelaminated and 1/4 delaminated model. A comparison of Figure 41 (a) and Figure 41 (b) shows that the amplitudes of the acceleration for the delaminated model is about 2 times that of the undelaminated one. The time histories of the acceleration response and the corresponding single-sided amplitude spectrum due to impulse and random excitation are also obtained and they provide useful information in identifying delamination, though they are not as accurate as those from swept sine excitation case. Table 22 provides a comparison of the undelaminated and delaminated models' frequencies identified from the responses due to the swept sine excitation. The identified frequencies are close to those from modal analysis based on properties within 1.5%. The difference in undelaminated and delaminated models' frequencies listed in this table demonstrates that the delamination can be detected using frequencies identified from the vibration data.

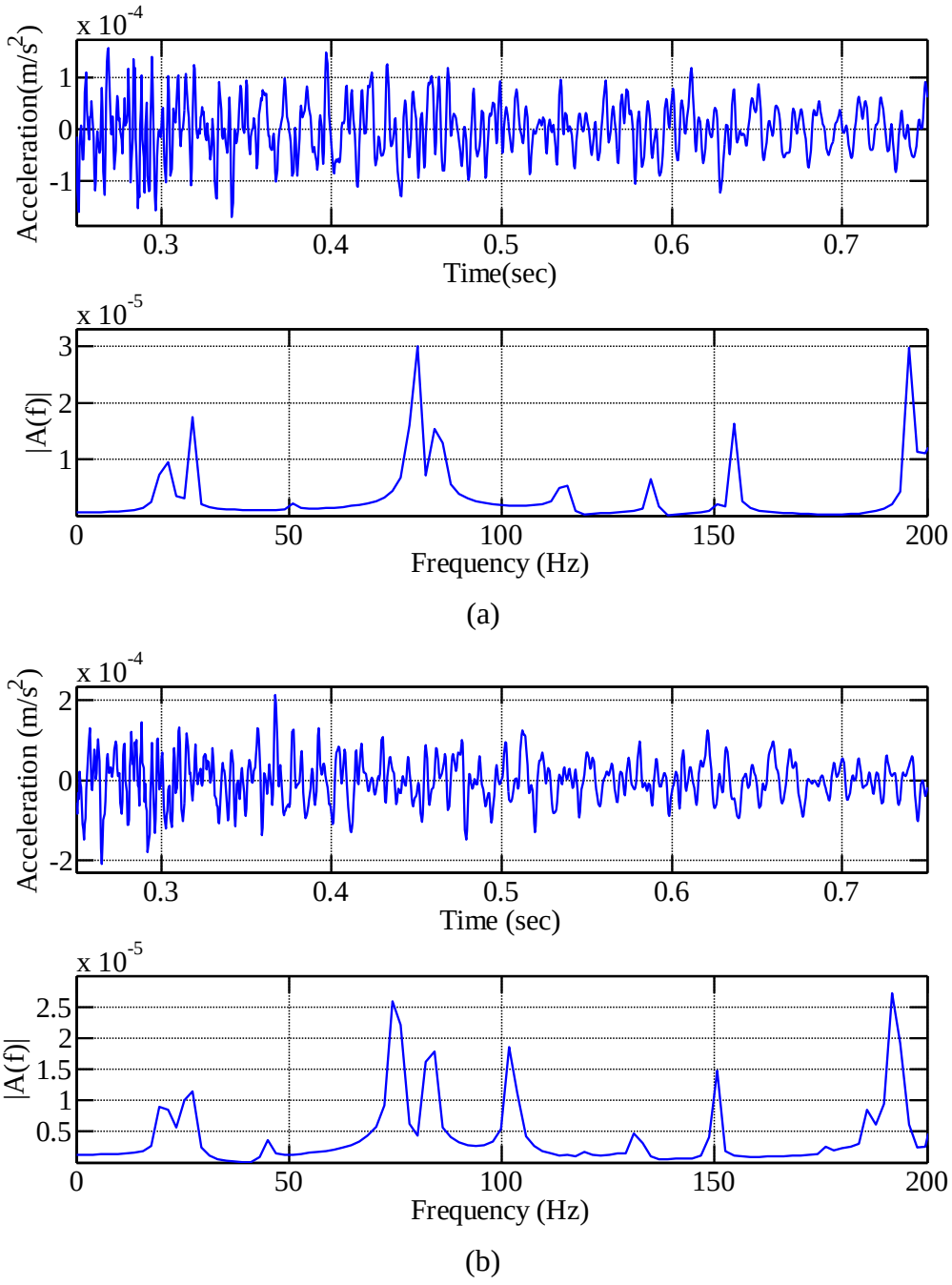

Figure 41. Acceleration and single-sided amplitude spectra of the models due to random excitation: (a) undelaminated model: upper row is the response history and lower row is the spectrum of the response; (b) 1/4 delaminated model: upper row is the response history and lower row is the spectrum of the response.

Table 22**.** Natural frequencies identified from the responses due to swept sine excitation for numerical example.

Mode	Undelaminatd (HZ)	1/4 Delaminated (HZ)	Difference (%)
1	20.56	19.57	-4.82
2	27.40	26.30	-4.01
3	50.88	45.01	-11.54

4. Experimental Studies

The objective of the experimental studies is to investigate the feasibility of delamination detection of concrete structures from real vibration measurements. The general conclusions from this section can be used to verify the previous numerical studies. In the experimental studies, four reinforced concrete plates with simulated delaminations were constructed in the Systems, Materials, and Structural Health (SMASH) lab at Utah State University (USU). Modal characteristics were extracted from the dynamic test data using three modal identification methods. The changes in modal characteristics were used for delamination detection. The finite element models, in this section, were developed for the experimental concrete slabs and the modal analyses based on the structural properties were carried out. Some useful conclusions were drawn from the studies.

4.1 Experimental setup and dynamic tests

Four reinforced concrete plates were constructed in the SMASH lab. Each concrete plate has the same size 1.83 m × 2.74 m × 0.14 m and same layout of #6 steel rebar as illustrated in Figure 42. All the concrete was placed from the same ready mix concrete batch in order to achieve similar concrete strength between test specimens. The only differences between the models were the different delamination scenarios that were introduced into the concrete plates.

In the delamination detection studies of composites [6-7], to generate the effects of delamination, Teflon films were inserted into the composite beams/plates to prevent layers from bonding together. In this study, plexiglass sheets (1.57 mm thick) were used to simulate the effect of a delamination. Plexiglass is unaffected by moisture and offers a high strength-to-weight ratio. One layer of plexiglass was placed into the horizontal plane of each delaminated concrete plate that was 0.09 m (5 1/2 inches) from the bottom of the plate during the concrete pouring. The horizontal areas of the delaminations were adjusted in each specimen. The first specimen had no delamination and is referred to as un-delaminated. The other three specimens had delamination sizes of 0.91 m × 1.22 m (22.2% delamination), 1.22 m × 2.13 m (51.9% delamination) and 1.52 m × 2.44 m (74.1% delamination) respectively. Figure 43 shows the plan and elevation views of the undelaminated and all delaminated specimens. Figure 44 shows the concrete pouring for the 22.2% and 74.1% delaminated specimens. Four months after concrete placing, the dynamic tests were performed. During the tests, two opposite longer edges of each concrete plate were placed on two timber supports and the other two opposite edges were free. All of the concrete slabs were tested with the same boundary conditions.

Based on the 28-day concrete compression and tensile tests as shown in Figure 45, the concrete's elastic modulus is E_c = 24,000 MPa (3481.0 ksi), ultimate uniaxial compressive strength σ_c = 27.5 MPa (4.0 ksi), ultimate uniaxial tensile strength σ_t = 14.69 MPa (2.1 ksi). The concrete density ρ_c = 2300 kg/m^3. Poisson's ratio of concrete ν_c = 0.15. The steel rebar's size is #6, its nominal diameter d = 19 mm, elastic modulus is E_s = 200 GPa, yield stress f_y = 410 MPa, Poisson's ratio ν_s = 0.3, and the density ρ_s = 7850 kg/m^3. It needs to be noted that Poisson's ratios of wood are difficult to be measured accurately

for they vary within and between species and are affected by moisture content and specific gravity [21]. According to the literature [21, 25-27] and finite element model updating in section 4, the ply wood anisotropic properties are as follows. The wood's density is 430 kg/m^3. The elastic moduli along the longitudinal, radial, and tangential axes of wood are denoted by E_L, E_R, and E_T, they are E_L = 8 GPa, E_R =0.068 × E_L and E_T = 0.05 × E_L. The values of ν_{LR} = 0.496, ν_{TL} = 0.274 and ν_{RT} = 0.56 were used in this study.

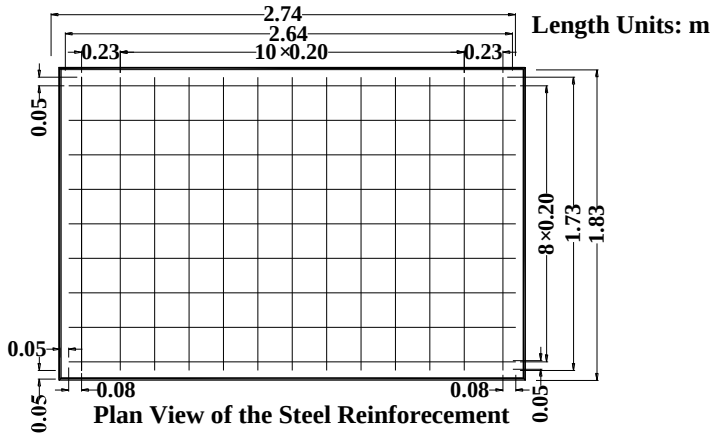

(a) Drawing of the plan view of steel reinforcement

(b) Formwork

Figure 42**.** Plan view of steel reinforcement.

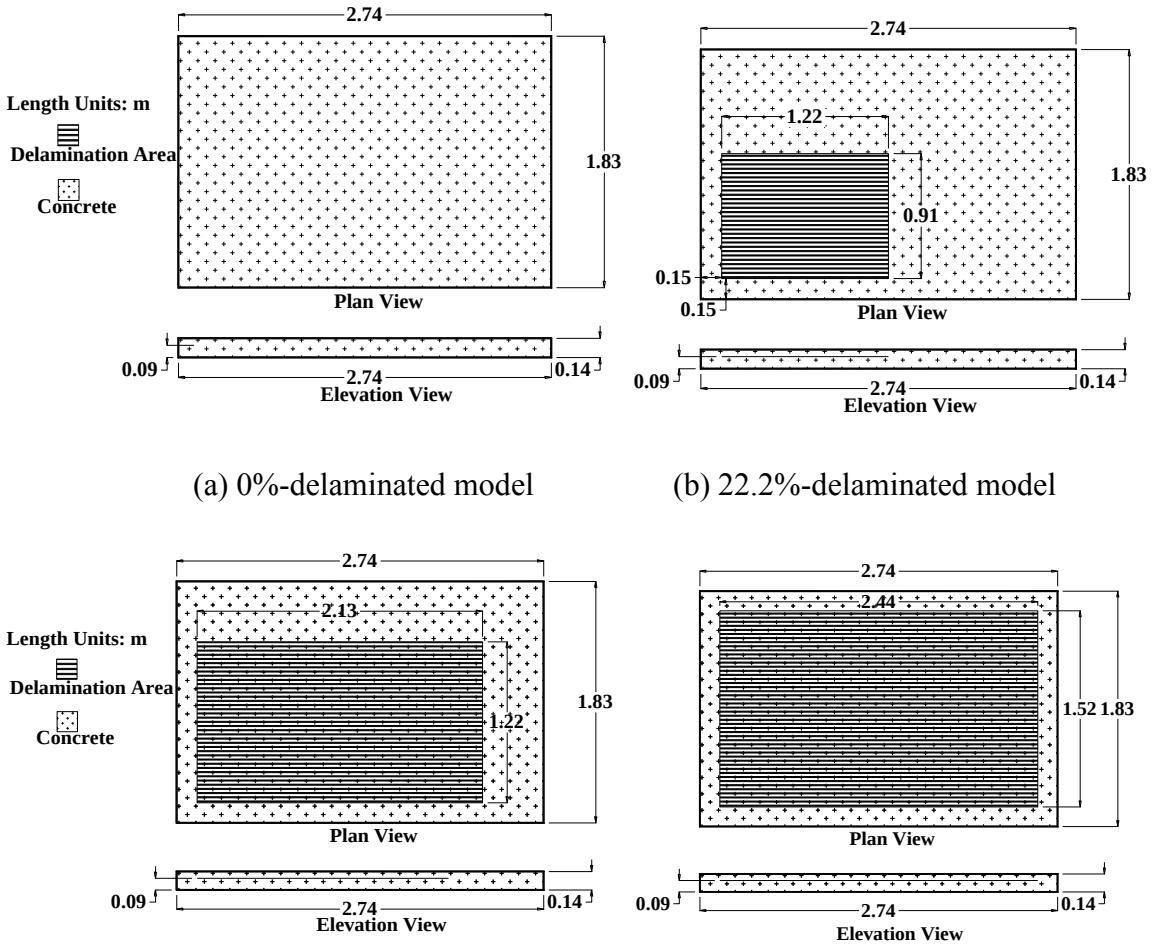

(a) 0%-delaminated model (b) 22.2%-delaminated model

(c) 51.9%-delaminated model (d) 74.1%-delaminated model

Figure 43. The locations of delamination areas (plexiglass) for the experimental concrete plates.

The same dynamics tests were performed on the four specimens for convenience of comparisons. Figure 46 illustrates the layout of excitation sources and sensors. An electromagnetic shaker and an instrumented hammer were employed to generate excitations. Six vertical velocity transducers (V1~V6) were used to measure the vertical velocity responses and one horizontal velocity transducer (V7) was used to measure the horizontal responses. An accelerometer was attached to the shaker to measure the real excitation inputs and the input acceleration of the instrumented hammer was also

measured. These measurements were recorded by a data physics vibration controller/signal analyzer. For the dynamic tests, the APS shaker generated swept sine, random, and impulse excitations on the specimens in sequence. Then the instrumented hammer applied impact excitations a few times on two locations. The typical random and swept sine acceleration inputs are shown in Figure 47 for the 74.1%-delaminated specimen, the inputs for the other specimens are similar. The velocity responses and the acceleration inputs were recorded for subsequent analyses. The recorded duration for each input by the shaker and hammer was 32 seconds. The sampling frequency was 1024 Hz, theoretically modal frequencies as high as 512 Hz could be identified; in reality the lower frequencies are critical.

(a) 22.2%-delaminated model (b) 74.1%-delaminated model

Figure 44. Pouring concrete on the plexiglass.

Figure 45 Cylinder compression tests.

4.2 Modal identification of the dynamic measurements

Classical peak-picking, frequency domain decomposition and stochastic subspace identification methods were used to obtain the modal parameters from the velocity responses. Typical time signals and amplitude spectra of them for the PP method are shown in Figure 48 for the vertical responses due to impact, swept sine, and random excitations, respectively. Figure 49 shows a similar plot for a horizontal response due to random excitation. Typical singular value plots by FDD for the undelaminated model are shown in Figure 50. Applying the SSI method in this study, the system order was n = 60 and the number of block rows was i = 400; however, when taking n = 30 and i = 150 there was an insignificant change in the results. The issue on how to select the system order is not studied deeply in this chapter; the stabilization diagram introduced in Chapter II is a good approach. The modal frequencies extracted by using PP, FDD and SSI methods are shown in Table 23 and the damping ratios identified by the SSI method are listed in Table 24. Figure 53 includes comparisons of the mode shapes of a specified mode for all the concrete slabs obtained by the FDD and SSI methods. For the purpose of

convenient comparison, the so-called mode shapes in Figure 53 are plotted with respect to the velocity transducer numbers V1~V6 instead of the real locations of the V1~V6 in three dimensions.

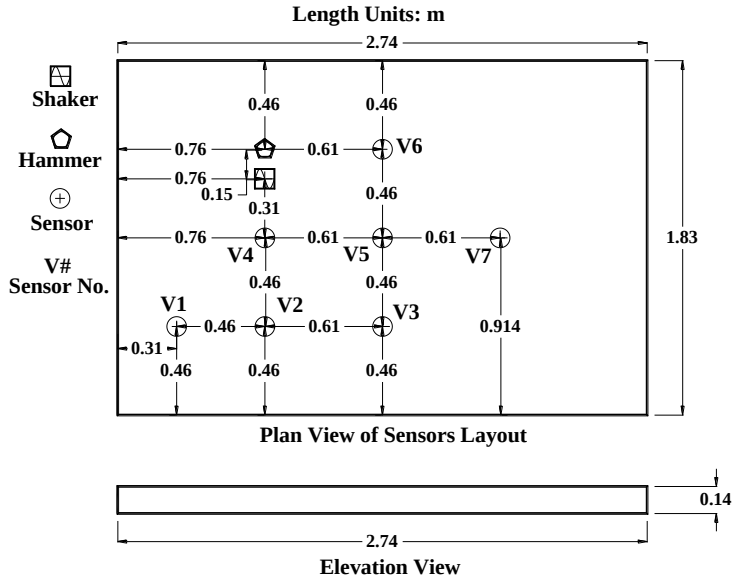

(a) Layout of excitation sources and sensors (length unit: m)

(b) One model for dynamic test

Figure 46. Layout of excitation sources and sensors for dynamic tests.

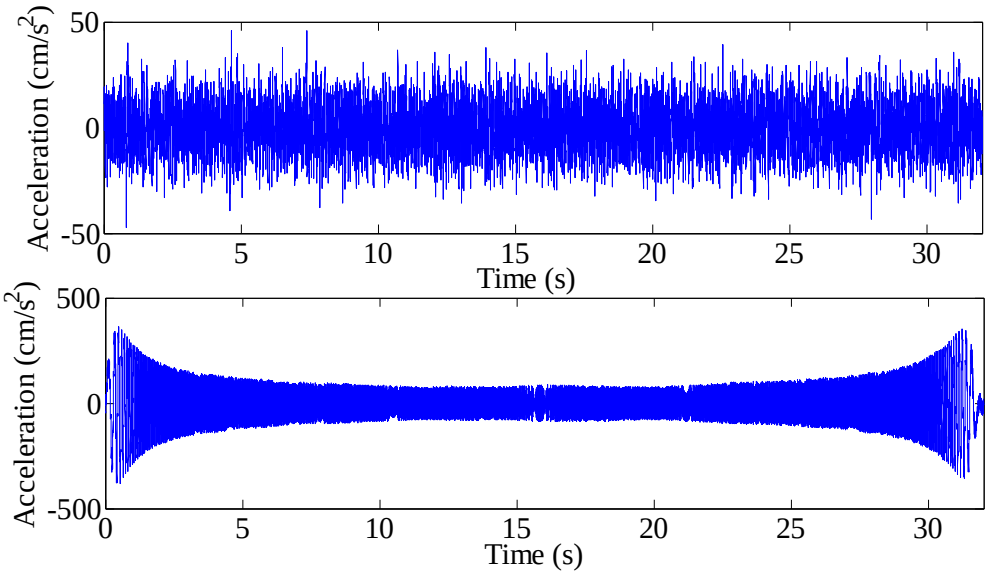

Figure 47. The random (upper) and swept sine (lower) excitations applied on the 74.1%-delaminated model.

Table 23. Modal frequencies identified by PP, FDD and SSI (i = 400, n = 60) methods from experimental specimens under random excitation.

0%-Delaminated	PP (HZ)	15.94	20.69	31.60	68.88	84.66	165.95
	FDD (HZ)	15.76	20.76	31.52	68.03	83.04	166.08
	SSI (HZ)	15.84	20.67	31.61	67.62(impact loc2)	82.60	166.37
22.2%-Delaminated	PP (HZ)	14.72	-	26.69	51.00	-	-
	FDD (HZ)	14.76	-	27.01	50.77	-	-
	SSI (HZ)	14.57	-	26.83	50.67	-	-
51.9%-Delaminated	PP (HZ)	14.66	-	27.60	-	-	-
	FDD (HZ)	14.01	17.51	27.51	49.47	-	-
	SSI (HZ)	13.99	-	27.56	-	-	-
74.1%-Delaminated	PP (HZ)	9.09	-	24.41	44.69	-	84.38
	FDD (HZ)	9.00	-	24.01	44.77	-	84.54
	SSI (HZ)	8.93	-	24.31	44.37	-	84.63

Table 24. The damping ratios identified by using SSI method from experimental specimens under random excitation.

-		Un-delaminated	22.2%-delaminated	51.9%-delaminated	74.1%-delaminated
From random responses	Frequency (HZ)	31.61	26.83	27.56	24.31
	ξ (%)	1.05	1.34	1.68	1.71
From impact responses	Frequency (HZ)	31.62`	26.87	27.44	9.15
	ξ (%)	1.25	1.46	1.32	1.43

The modal frequencies extracted from transducers V1-V6 vary by a maximum of only 2% for the presented results, only the results from V4 and V7 are shown in the figures for illustration. The frequencies listed in the Tables are also identified from these selected sensors. In Table 23, the frequencies identified by the three methods agree very well for most modes, the differences between the 1st frequencies by these methods for all the specimens are less than 4.8%. From the comparisons in Figure 53, it is evident that the mode shapes extracted by the FDD and SSI methods yield identical or at least consistent results. While this paper mainly demonstrates analyses on the responses due to random excitations, the modal characteristics obtained from response measurements due to impact and swept sine excitations agree very well with those obtained from the random excitation cases, e.g., for all the specimens, the differences between the corresponding 1st frequencies by the SSI method due to random and impact excitations are within 2.5%. In other word, excellent agreements are obtained for modal frequencies and mode shapes regardless of the different identification methods and different excitation inputs, and this validates the extracted modal characteristics are correct for the dynamic test data. For the results due to impact and swept sine excitation, refer to Appendix A.

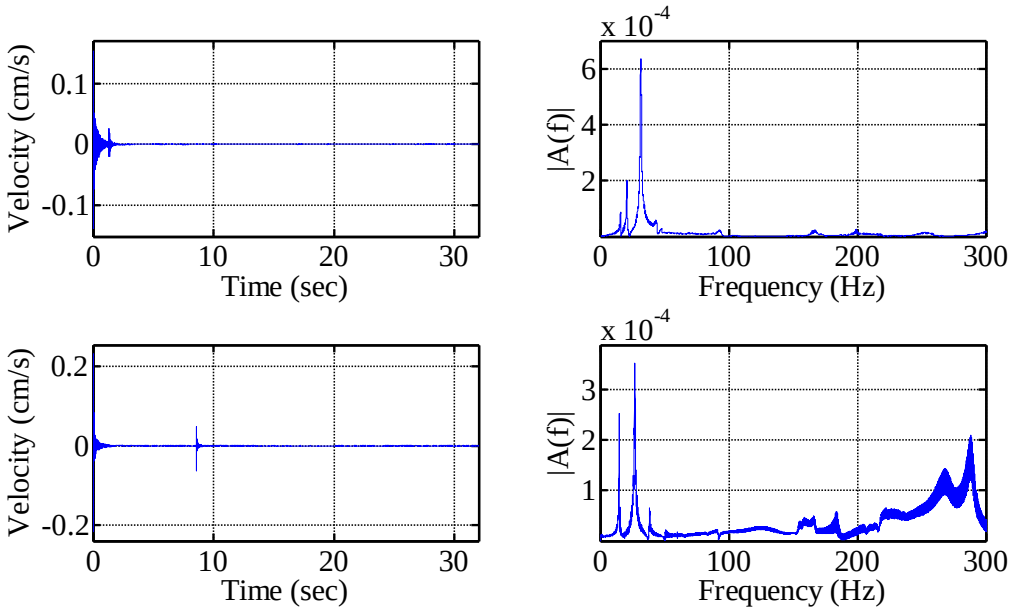

(a) Due to impact excitations.

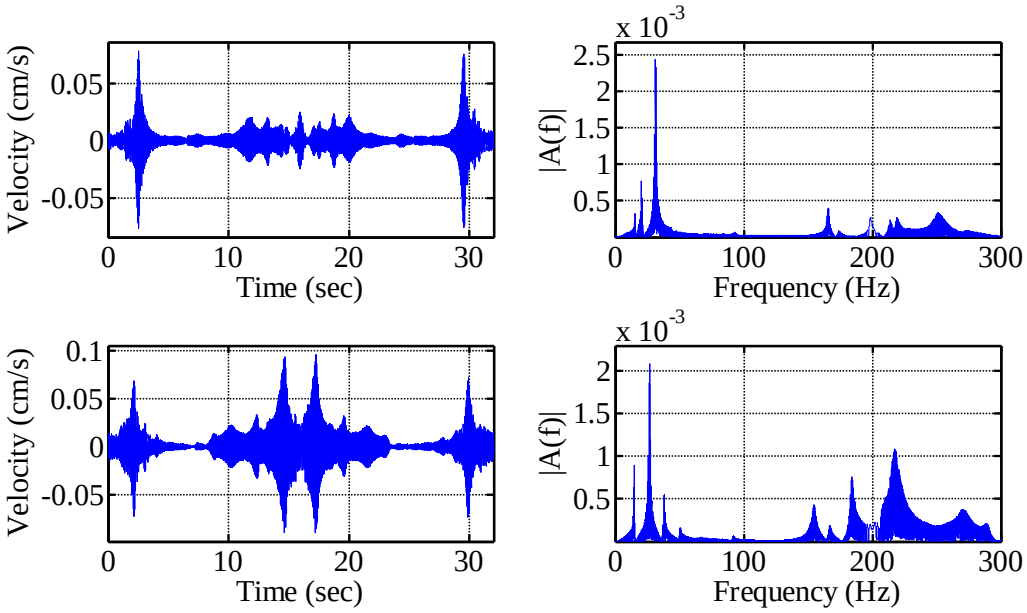

(b) Due to swept sine excitations.

Figure 48. Typical time signals of vertical sensor V4 and single-sided amplitude spectra of them (left column is time signal, right column is spectrum; upper row is for undelaminated model, lower row is for 22.2%-delaminated model) (cont.).

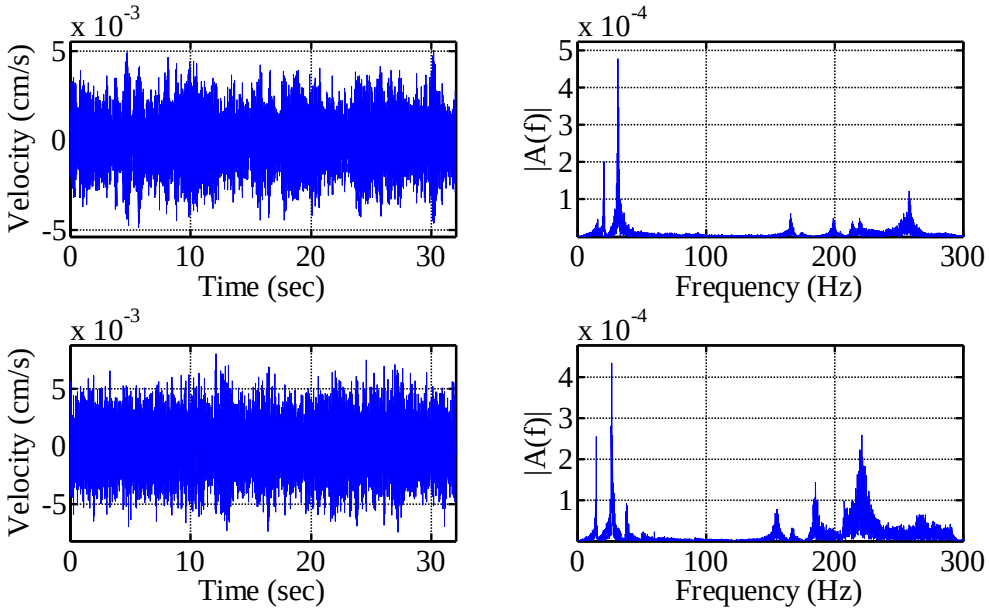

(c) Due to random excitations

Figure 48. Cont'd

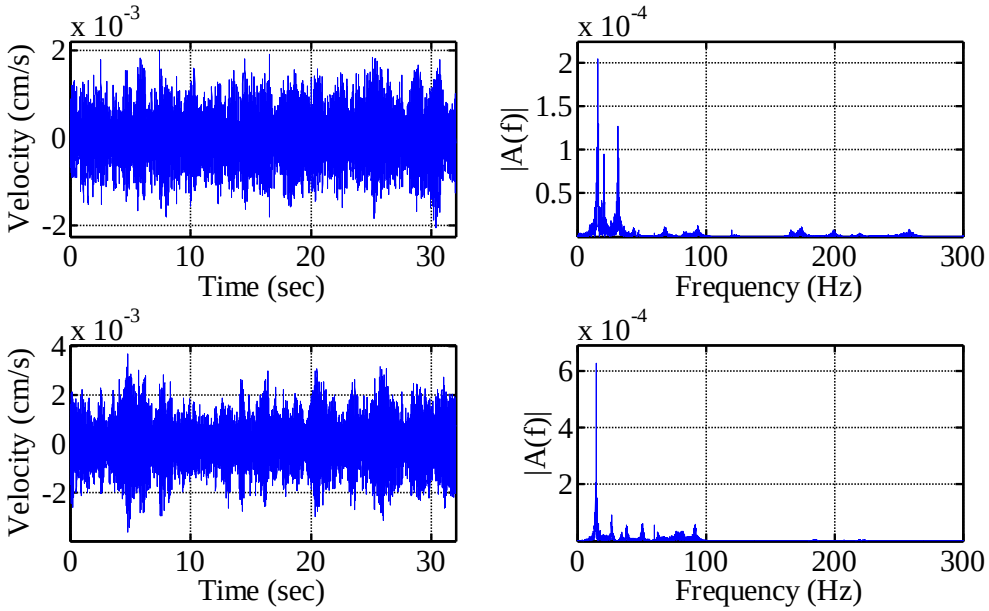

Figure 49. Typical time signals of horizontal sensor V7 and single-sided amplitude spectra of them for two models due to random excitations (left column is time signal, right column is spectrum, upper row is for undelaminated model, lower row is for 22.2%-delaminated model).

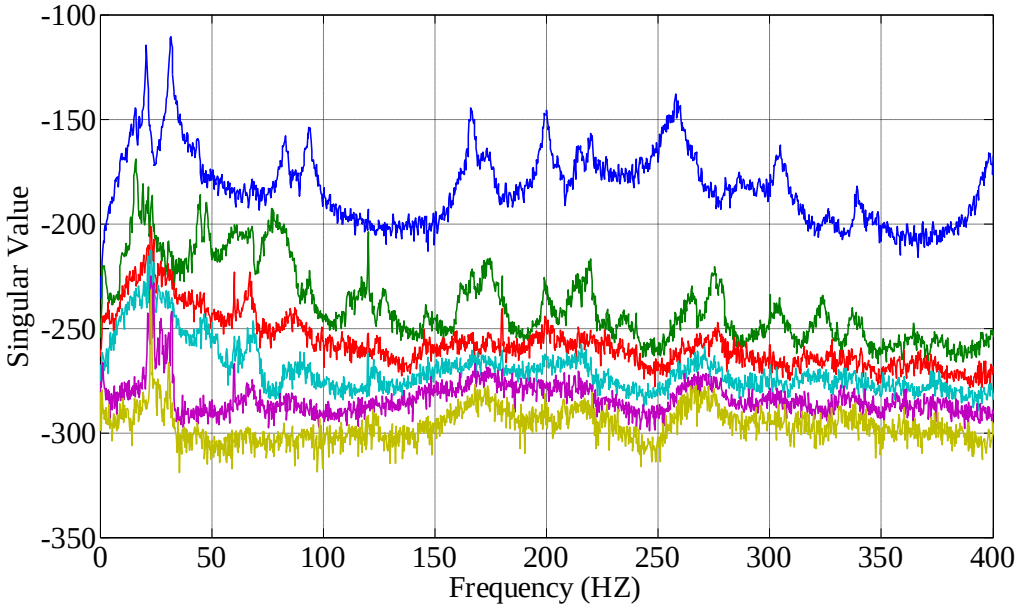

(a) undelaminated model

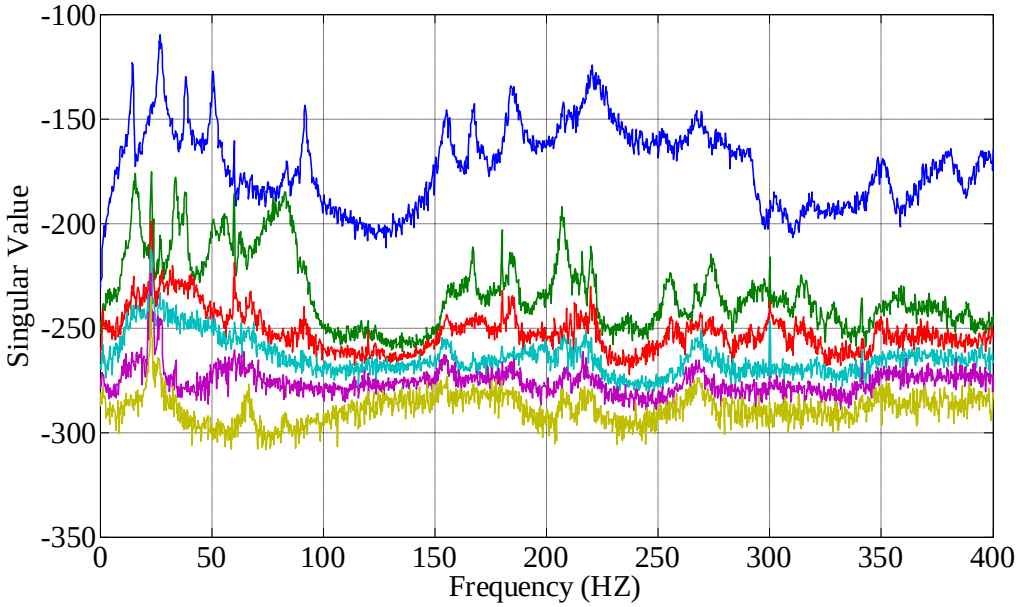

(b) 22.2%-delaminated model

Figure 50. Singular values of PSD of the responses (V1~V6) due to random excitation for the tested models.

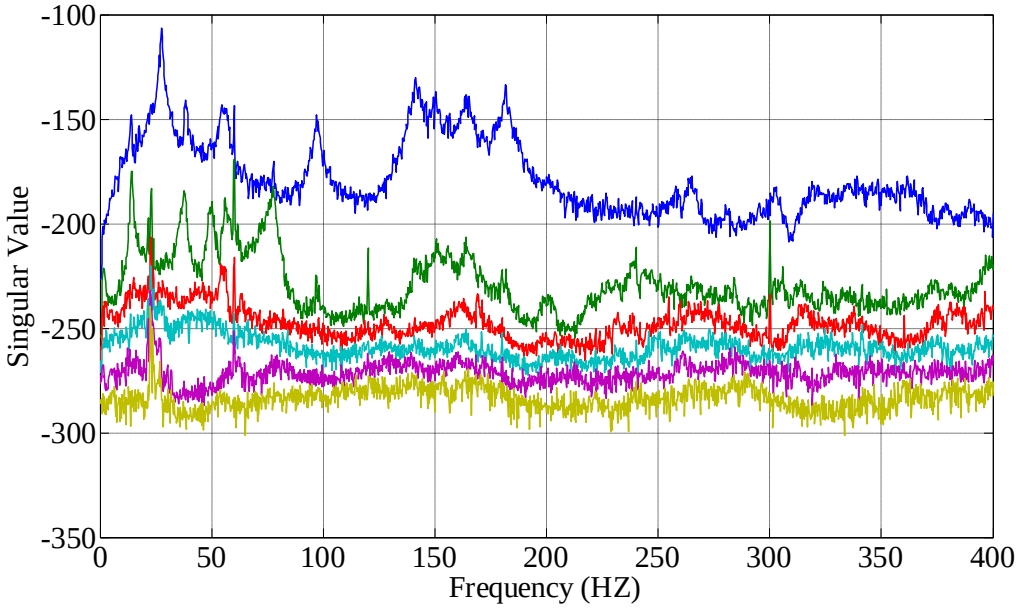

(c) 51.9%-delaminated model

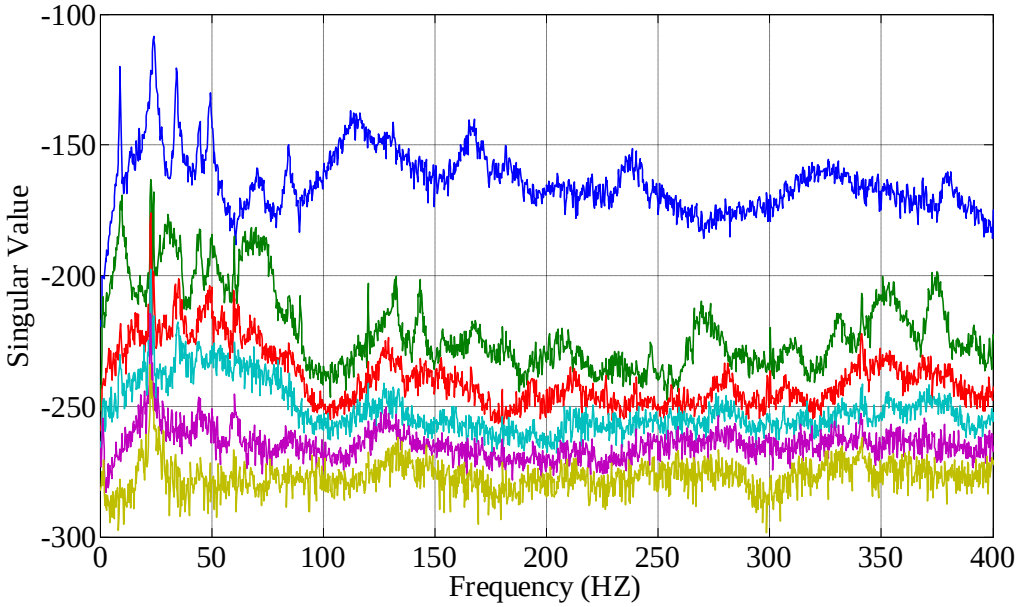

(d) 74.1%-delaminated model

Figure 50. Cont'd

The effectiveness of using changes in modal frequencies and mode shapes as damage indicators of delaminations is examined in Figure 48-Figure 50 and Figure 53 and Table 23-Table 24. Figure 48 shows that the fundamental frequencies of the delaminated specimens are decreased compared with that of the un-delaminated specimen. It can also be observed that vibration energy of the response of the un-delaminated specimen is concentrated in the first few modes; however, the delaminated specimens exhibit a relatively higher level of response in the higher modes. The same conclusions can be drawn from the results for the 51.9% and 74.1% delaminated specimens. Figure 49 shows the time signal and single-sided amplitude spectrum of the horizontal sensor. This figure is used to help evaluate the modal characteristics, e.g., the 1st modal frequency in Table 23 can be determined as a horizontal mode by referring to Figure 49 and the finite element models in section 4.3. From Table 23, It can be seen that the corresponding frequencies decrease with the increase of delamination size, among which the 1st frequency decreases from 15.76 HZ to 9.00 HZ. The 22.2%-delaminated model was supposed to have higher frequencies than the corresponding ones of 51.9%-delaminated, while they are slightly lower than expected. From Table 24, it is observed that generally the listed damping ratios of the corresponding mode show a trend of increase with the increase of delamination size from 1.05% (1.25%) to 1.71% (1.43%). The damping ratios can assist in identifying delamination, but it is not recommended to rely on damping alone due to the complexity of damping mechanism and difficulty in obtaining accurate damping values in experimental studies. Figure 53 displays the changes in corresponding mode shapes for different delaminated models. It demonstrates that when the delaminated areas become larger and develop to a previous undelaminated

area, the responses of this area will then become relatively higher than its former state. Because of the use of very few sensors in this study, detailed results are not accurate regarding the use of mode shapes for the detection of delaminations. Figure 53 shows some of the scarce modal shape data. It is highly recommended that additional work be performed with a much denser array of sensors in order to obtain more conclusive results regarding mode shapes.

4.3 Finite element modeling of the experimental models

The finite element models of the reinforced concrete specimen were created using ANSYS software. The origin of the coordinate system is at the left bottom corner as shown in Figure 37 and Figure 51 exhibits an isometric view and a front view of the entities. The longitudinal steel rebar were placed in the model at the plane of Y=0.05 m. The transversal rebar were placed immediately above the longitudinal rebar. The two opposite edges with X = 0 m and X = 1.83 m of concrete plates are supported on two ply woods, the other two edges Z = 0 m and Z = 2.74 m are free. Solid65, link8 and solid45 elements were selected to represent concrete, steel rebar, and wood, respectively. The laboratory floor was modeled using solid65 elements with infinite strength. Dynamic characteristics are sensitive to the boundary conditions, so the wood supports were modeled delicately instead of as ideal simple supports. Contact and target elements were used to model the contact between the concrete and wood, and between the wood and the floor of the lab. The properties of the contact elements were updated during the modal analysis to match the results from real measurements. The delaminations were modeled by reducing the elastic modulus of the corresponding areas to very small numbers.

Modal analyses of all of the four reinforced concrete slab specimens were performed. The computed modal frequencies and mode shapes were compared with those from experimental tests. Comparisons of frequencies are listed in Table 25 and one mode shape of the undelaminated and delaminated models are shown in Figure 52. Table 25 demonstrates that the lowest and even relatively high order modal frequencies calculated by ANSYS model match those from dynamic testing well, the difference between the ANSYS model and FDD method from test data for the first three frequencies are maximally 7%. Figure 52 shows that the frequencies of the delaminated models decrease and the mode shapes have abrupt changes at the delaminated areas. Figure 53 compares the mode shapes for the same mode by the FDD, SSI methods, and ANSYS modeling. It is observed that the mode shapes of the ANSYS models are not same as those identified from test measurements, but they are consistent with those obtained from the measurements to a certain degree; this could validate the ANSYS models to be approximate models instead of exact ones. It is hard to establish finite element models with same modal characteristics as those of test specimens due to the complex boundary conditions for these tests. However, the finite element modeling is still very useful for initial investigations.

It is concluded that the finite element modeling can approximately simulate the undelaminated and delaminated concrete slabs for these experimental studies modal analysis. The results computed by the finite element analysis can be used as supplements for modal identification of the dynamic test data to determine the modal characteristics. The finite element modeling can provide initial investigation for further experimental tests and can also be used effectively for parameter studies.

Table 25. Comparison of modal frequencies (unit: Hz) by ANSYS modeling and FDD of the responses of experimental specimens under random excitation

	-	Horizontal	Horizontal	Vertical Y+ bending along Z	Bending along X	Torsion in XY	Bending along X
0%-Delaminated	ANSYS	15.52	20.90	31.46	69.13	81.68	165.80
	FDD	15.76	20.76	31.77	68.03	83.04	166.08
22.2%-Delaminated	ANSYS	14.70	-	27.38	51.99	-	-
	FDD	14.76	-	27.01	50.77	-	-
51.9%-Delaminated	ANSYS	14.73	16.26	26.98	50.81	-	-
	FDD	14.01	17.51	27.51	49.47	-	-
74.1%-Delaminated	ANSYS	9.41	-	24.91	42.78	-	81.39
	FDD	9.00	-	24.01	44.77	-	84.54

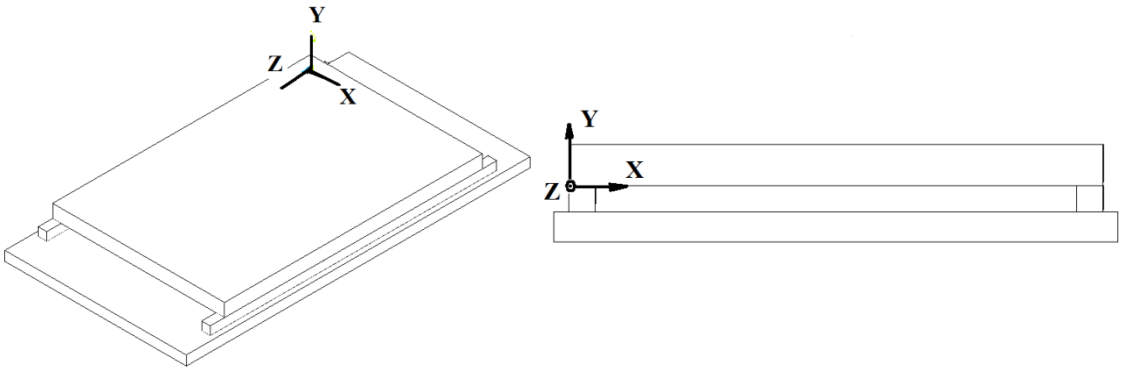

Figure 51. The coordinate system of the finite element model (left is isometric view, right is front view)

5. Conclusions

This paper presents a study on delamination detection of concrete plates by modal identification of output only data measured by vibration sensors. The feasibility is examined through numerical as well as experimental studies.

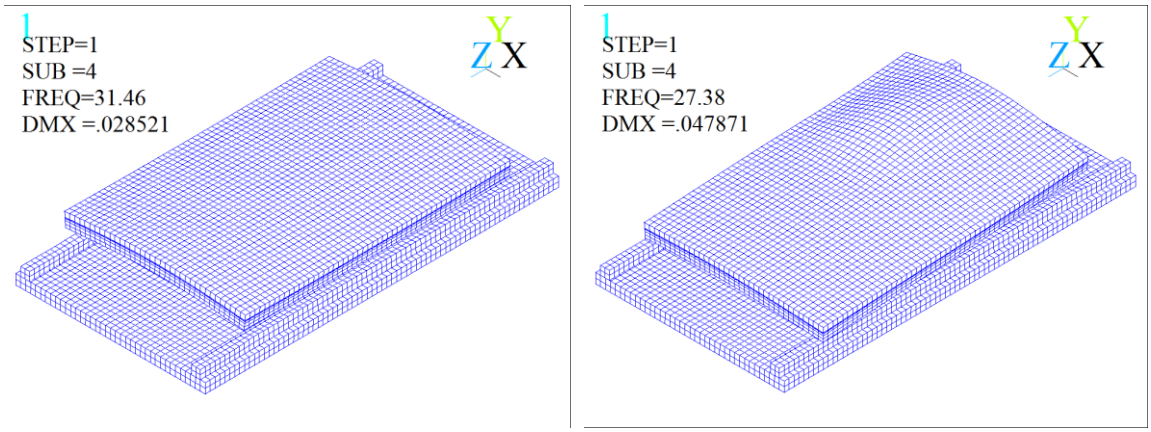

(a) (b)

Figure 52. The mode shapes for the undelaminated model and the 22.2%-delaminated model: (a) undelaminated model, frequency is 31.46 HZ; (b) 22.2%-delaminated model, frequency is 27.38 HZ.

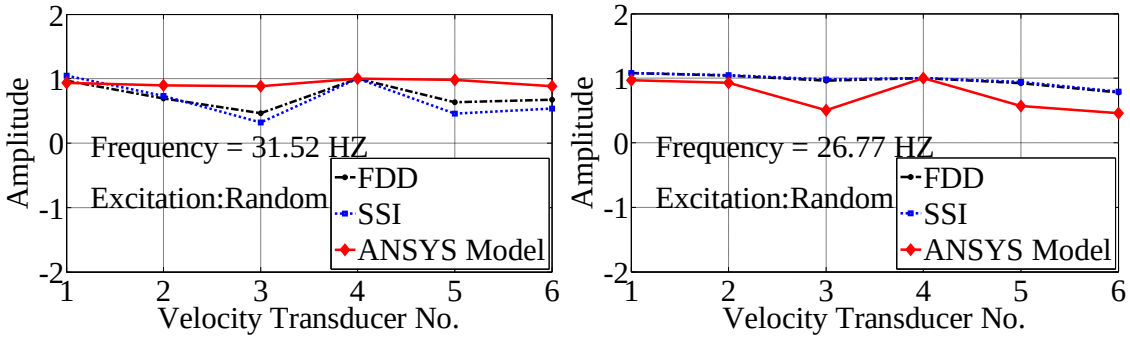

(a) undelaminated model (b) 22.2%-delaminated model

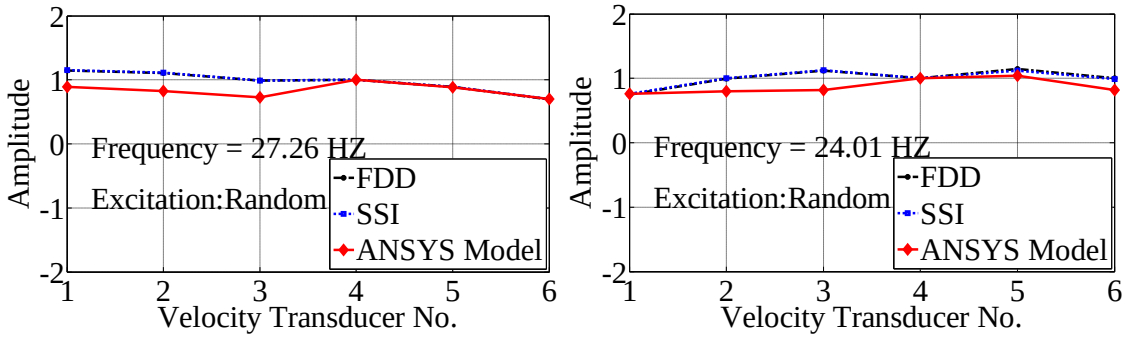

(c) 51.9%-delaminated model (d) 74.1%-delaminated model

Figure 53. Comparison of mode shapes by FDD, SSI from the response measurements due to random excitation and ANSYS model.

Parameter studies on the effects of delamination on modal characteristics were performed through finite element modeling. The delaminations with different sizes and locations were introduced into the concrete plates separately, which were simply supported on two opposite edges and free on the others.

1) For the concrete slabs, modal characteristics are dependent on the size of the delamination. The changes in mode shapes were sensitive to delaminations and can indicate and locate the development of delamination. For the symmetrically located delaminations, it can be summarized as follows. When $1/12 \leq A_{delam}/A_{tot} < 1/6$, the changes in the 3rd or 4th mode shape may indicate the presence of delamination. When $1/6 \leq A_{delam}/A_{tot} \leq 1/3$, the reductions in the 3rd frequency range from 2% to 17.5%, they can be used to indicate the presence of delamination and the corresponding mode shapes can be used to locate the delaminations. When $A_{delam}/A_{tot} > 1/3$, the reduction in the 1st frequency was greater than 3%, so the changes in the 1st frequency and mode shape can indicate delamination.

2) From the results of the 1/3-delaminated models at unsymmetrical and symmetrical locations, it is observed that the location of the delamination can have significant effect on modal parameters. The more unsymmetrical the delamination area was with respect to the total area, the bigger the changes in the frequencies and mode shapes. For example, the changes in the 1st frequencies are 28.24% and 1.18% for the unsymmetrical and symmetrical delaminated 1/3 models, respectively.

3) Some specific modes were more sensitive to delamination than their adjacent modes and are shown to be excellent indicators of delamination. For example, the changes in the 4th modal frequencies of the A_{delam}/A_{tot} =1/6, 1/4, 1/3 delaminated models,

are bigger than their neighboring modes.

4) The dynamic analyses illustrated that the acceleration amplitudes of the delaminated model were obviously larger than those of the un-delaminated model. The modal frequencies extracted from the acceleration responses were effective for detecting delamination for the1/4 model with 4.8% change in the 1st frequency. Both the dynamic response itself and the modal parameters identified from the response can be used for delamination identification.

Experimental studies were conducted on reinforced concrete plates with different delamination sizes. The modal characteristics were extracted from the dynamic responses and analyzed. Finite element models of concrete slabs were developed using ANSYS. Conclusions are drawn as follows.

1) Changes in frequencies and mode shapes can indicate the occurrence and extent of delamination. The frequencies decrease with the increase of delamination sizes. The 1st modal frequency decreased 43% for the 74.1%-delaminated specimen when compared to the undamaged specimen. The changes in higher modal frequencies are larger. The experimental results show that the damping ratios increase with the increase of delamination sizes. Damping can assist in the delamination identification, but it alone is not suitable as a delamination indicator. It is demonstrated that the mode shapes have abrupt changes in the delamination areas of the specimens.

2) It is beneficial to use multiple identification methods to ensure correct identification results. The frequencies identified by the PP, FDD and SSI methods agree well, the maximum difference between the 1st frequencies by these methods is less than 4.8%. The mode shapes extracted by FDD and SSI are shown to be identical.

3) In the finite element modeling, it was determined that the wood supports must be modeled properly instead of using idealized simply supported conditions in order to achieve accurate results. The frequencies for lower order modes calculated by the FE models agreed well with those identified from test data, among which the differences between the first three modal frequencies by ANSYS model and FDD method from test data are within 7%. The mode shapes obtained by ANSYS model are only approximately similar to those identified from tests due to the complex boundary conditions for the test specimens, but they are consistent to a certain degree. Therefore finite element models can approximately model delaminated concrete slabs for modal analysis, while they are not exact for these experiments.

This study provides useful information for practical delamination detection of bridge decks by vibration-based health monitoring systems. For the future work, experimental modal testing with more stable and practical boundary conditions are needed. Stabilization diagrams are suggested to be used for obtaining more accurate modal characteristics. Further work is necessary for developing more sensitive delamination indicators and more accurate finite element models. Additionally, field tests utilizing actual delaminations are highly recommended.

REFERENCES

[1] J. Warhus, J. Mast, S. Nelson, Imaging radar for bridge deck inspection, *Nondestructive Evaluation of Aging Bridges and Highways*, Oakland, CA, 1995.

[2] J.P. Broomfield, Corrosion of steel in concrete, understanding, investigating, and repair, second ed., E & FN Spon, London, 1997.

[3] C.Q. Li, J.J. Zheng, W. Lawanwisut, R.E. Melchers, Concrete delamination caused by

steel reinforcement corrosion, *Journal of Materials in Civil Engineering* 19 (2007) 591-600.

[4] N. Gucunski, Z. Wang, T. Fang, A. Maher, Rapid Bridge Deck Condition Assessment Using Three-Dimensional Visualization of Impact Echo Data, *Proceedings of Non-Destructive Testing in Civil Engineering*, Nantes, France, 2009.

[5] Y. Zhou, L. Tong, G.P. Steven, Vibration-based model-dependent damage (delamination) identification and health monitoring for composite structures-a review, *Journal of Sound and Vibration* 230 (2000) 357-378.

[6] S.H.D. Valdes, C. Soutis, Delamination detection in composite laminates from variations of their modal characteristics, *Journal of Sound and Vibration* 228 (1999) 1-9.

[7] C.P. Ratcliffe, W.J. Bagaria, Vibration technique for locating delamination in a composite beam, *AIAA Journal* 36 (1998) 1074-1077.

[8] Z. Wei, L.H. Yam, L. Cheng, Delamination assessment of multilayer composite plates using model-based neural networks, *Journal of Vibration and Control* 11 (2005) 607-625.

[9] Z. Zhou, M. Noori, R.S. Amand, Wavelet-based approach for structural damage detection, *ASCE Journal of Engineering Mechanics* 126 (2000) 677-683.

[10] Q. Wang, X. Deng, Damage detection with spatial wavelets, *International Journal of Solids and Structures* 36 (1999) 3443-3468.

[11] E. Douka, S. Loutridis, A. Trochidis, Crack identification in plates using wavelet analysis, *Journal of Sound and Vibration* 270 (2004) 279-295.

[12] Y.J. Yan, L.H. Yam, Detection of delamination damage in composite plates using energy spectrum of structural dynamic responses decomposed by wavelet analysis, *Computers & Structures* 82 (2004) 347-358.

[13] S. Xing, M.W. Halling, P.J. Barr, Delamination detection and location in concrete deck by modal identificationl, *Proceedings of Structures Congress 2010*, Orlando, FL, USA, 2010, 741-751.

[14] S. Xing, M.W. Halling, P.J. Barr, Delamination detection in concrete plates using output-only vibration measurements, *Proceedings of the 29th International Modal Analysis Conference*, Jacksonville, FL, 2011.

[15] R. Brincker, L. Zhang, P. Andersen, Modal identification from ambient responses using frequency domain decomposition, *Proceedings of the 18th International Modal Analysis Conference*, San Antonio, TX, 2000, 625-630.

[16] R. Brincker, C.E. Ventura, P. Anderson, Damping estimation by frequency domain decomposition, *Proceedings of the 19th International Modal Analysis Conference*, Kissimmee, FL, 2001, 698–703.

[17] P. Van Overschee, B. De Moor, Subspace algorithms for the stochastic identification problem, *Automatica* 29 (1993) 649-660.

[18] P. Van Overschee, B. De Moor, *Subspace Identification for Linear Systems: Theory, Implementation, Applications*, Kluwer Academic Publishers, Dordrecht, 1996.

[19] B. Peeters, G. De Roeck, Reference-based stochastic subspace identification for output-only modal analysis, *Mechanical Systems and Signal Processing* 13 (1999) 855-878.

[20] T. Katayama, *Subspace Methods for System Identification*, 1st ed., Springer, Englewood Cliffs, NJ, 2005.

[21] Ansys, Release 10.0 ANSYS theory reference, 2005.

[22] S. Rajendran, D.Q. Song, Finite element modeling of delamination buckling of

composite panel using Ansys, *Proceedings of 2nd Asian ANSYS User Conference*, Singapore, 1998.

[23] A.W. Leissa, The free vibration of rectangular plates, *Journal of Sound and Vibration* 31 (1973) 257-293.

[24] K.M. Liew, Y. Xiang, S. Kitipornchai, C.M. Wang, *Vibration of Mindlin plates: programming the p-version Ritz Method*, Elsevier Science, Oxford, 1998.

[25] Forest Products Laboratory, Wood handbook: wood as an engineering material, *General Technical Report FPL-GTR-190*, U.S. Department of Agriculture, Forest Service, Forest Products Laboratory, Madison, WI, 2010.

[26] R.S. McBURNEY, J.T. DROW, The elastic properties of wood Young's moduli and poisson's ratios of douglas-fir and their relations to moisture content, Forest Products Laboratory, Forest Product Service, U. S. Department of Agriculture, 1962.

[27] A. Sliker, Measuring Poisson's ratios in wood, *Experimental Mechanics* 12 (1972) 239-242.

CHAPTER V

STRUCTURAL POUNDING IDENTIFICATION BY USING WAVELET SCALOGRAM

ABSTRACT

Structural pounding can cause considerable damage and even lead to collapse of structures. Most pounding research focuses on modeling, parameter investigation and mitigation approaches. With the development of structural heath monitoring, the on-line detection of pounding and parameter determination is possible. The detection of pounding can provide useful early information about the potential damage of structures. This paper proposed using wavelet scalograms of dynamic response to identify pounding and examined the feasibility of this method. Numerical investigations were performed on a pounding system that consists of a damped single-degree-of-freedom (SDOF) elastic structure and a rigid barrier. The Hertz contact model was employed to simulate nonlinear pounding behavior. The responses and pounding forces of the pounding system under harmonic and earthquake excitations separately were numerically solved. The wavelet scalograms of the acceleration responses were then used to identify the poundings. It was found that the scalograms can recognize the presence of the poundings and indicate the time of their occurrence very well The approximate severity of the poundings were also demonstrated. Experimental studies were carried out as well, in which the shake table tests were conducted on a steel bridge model that underwent pounding between its different components during ground motion excitation. The wavelet scalograms of the bridge responses were analyzed, and they were able to indicate pounding occurrence quite well. Hence the conclusions from the numerical studies were verified

experimentally.

1. Introduction

The different phase vibrations of neighboring buildings or adjacent parts of the same building or bridge can result in pounding under earthquake excitation if the separation distance between them is not sufficient. The pounding can cause considerable damage and even lead to collapse of structures, especially bridges with columns of unequal heights [1-2]. Damage of buildings and bridges due to pounding have been documented in the reports of many earthquakes by researchers. The pounding research mostly focused on modeling of pounding systems, parameter investigations and mitigation approaches.

Most mathematical pounding modeling methods fall into two categories: a) stereomechanical impact approach, which is primarily based on impulse-momentum law and b) contact element approach, a force-based approach. The first approach was used in [3] and other literature. Hertz contact model, a contact element approach, has been extensively used to model impact [4-7]. The numerical study portion of this paper also uses this model.

With the development of structural health monitoring systems in bridges and other civil structures, the on-line detection of the presence of pounding and parameter determination of the pounding system becomes possible. Valuable information about pounding can be extracted from the analyzed on-line data to provide early warning about damage to the structures. There is very little research on this useful topic based on the author's knowledge. Wavelets allow for powerful and flexible methods for dealing with fundamental engineering problems and have been used within a broader scope [8]. This

paper proposes to use wavelet scalograms to detect the occurrence of pounding.

Wavelet scalogram is the square of the modulus of the wavelet transform. It can uncover previously concealed information about the nature of non-stationary processes. It has been widely used in vibration signal analysis, which includes denoising, fault diagnostics, structural performance testing, ground motion analysis, bridge response due to vortex shedding and many other forms of analysis [9-10].

The primary objective of this paper is to investigate the applicability of wavelet scalograms in seismic pounding identification. Numerical and experimental studies were conducted to achieve this aim. In the numerical study, the Hertz contact model was introduced into the pounding modeling and the properties of a large-scale bridge segment were used for a SDOF concrete structure while the appropriate value of an impact stiffness parameter was calculated. The responses of the pounding system between the SDOF structure subjected to harmonic and earthquake excitations and a stationary rigid structure were computed and processed to obtain wavelet scalograms. In the experimental studies, the dynamic measurements from shake table tests on pounding of different units of a steel bridge were used to obtain wavelet scalograms. These results were analyzed to evaluate the effectiveness of scalogram in identifying seismic pounding.

2. Investigation of the Pounding Model

2.1 Pounding model

In the numerical study, pounding is simulated by an impact oscillator, which was proposed by Davis [5] and later adopted in the literature [4, 6-7]. An SDOF damped oscillator subjected to ground motion as illustrated in Figure 54, was studied. The pounding occurred between the oscillator and a neighboring stationary rigid structure.

The neighboring structure can also be flexible structures; however, for the sake of simplicity, this paper investigates the rigid case only.

The equation of motion for the nonlinear pounding model of the SDOF system subjected to ground motion $\ddot{x}_g(t)$ in Figure 54 is

$$m\ddot{x}(t)+c\dot{x}(t)+R(x,t)+F(t)=-m\ddot{x}_g(t) \tag{123}$$

where m and c denote the system mass and damping coefficient, and $\ddot{x}$, $\dot{x}$, x symbolize the relative acceleration, velocity and displacement relative to the ground while the superimposed dot denotes differentiation with respect to time, and R(x, t) is the restoring force.

This study was focused on an elastic structure. For this case, the damping coefficient and restoring force can be expressed as

$$c=2\xi\sqrt{km}; \qquad R(x,t)=k_e x(t) \tag{124}$$

where ξ and k_e denote the damping ratio and initial stiffness respectively.

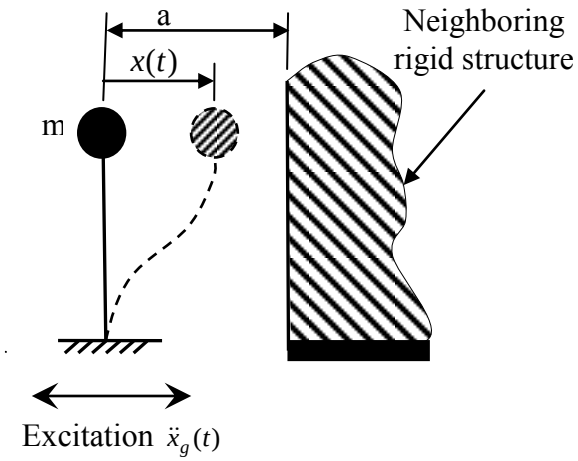

Figure 54. The impact oscillator for one-sided pounding.

F(t) in Eq. (123) is the impact force between the colliding structures. Using the Hertz contact model, the impact force is represented by a non-linear spring of stiffness β and can be expresses as

$$F(t)=\begin{cases}\beta[x(t)-a]^{3/2} & for \quad x(t)>a \\ 0 & for \quad x(t)\le a\end{cases} \tag{125}$$

where a is the separation distance between the colliding structures. The Hertz exponent 3/2 is a typical value to render the Eq. (123) as nonlinear, while pounding in the real world may have different values, but alternative values will have little effect on the system's response [5-6]. β is the impact stiffness parameter, which is dependent on the material properties and geometric surfaces of the contact bodies [11]. The calculation of values β for some special cases can be found in [12]. For the pounding between concrete bodies, the values of β typically range from 2 ~ 80 kN/mm$^{3/2}$ as demonstrated in [11]. However, these values are based on small scale experiments, and are not suitable for large-scale situations [7].

In the numerical examples used in this paper, the impact between a sphere of radius R_1 and massive plane surface of $R_2 = \infty$ was considered. The appropriate impact stiffness parameter is calculated as

$$\beta=\frac{4}{3\pi}\sqrt{R_1}\,\frac{1}{\delta_1+\delta_2} \tag{126}$$

where $\delta_1=\frac{1-\nu_1^2}{E_1}$; $\delta_2=\frac{1-\nu_2^2}{E_2}$, R_1 is the radius of the flexible structure in Figure 54, E_1, E_2, ν_1, and ν_2 are the elastic modulus and Poisson's ratios of the contact structures respectively. For the neighboring rigid barrier, assume $E_2 \to \infty$, then $\delta_2 \to 0$, Eq. (126) becomes

$$\beta=\frac{4}{3\pi}\sqrt{R_1}\frac{E_1}{1-\nu_1^2} \tag{127}$$

Eq. (127) is used in Section 4 to calculate β.

2.2 Solution of the equation of motion

The equation of motion (123) was solved by using the Dormand-Prince 4th-order-runge-kutta method with adaptive size as well as the Dormand-Prince 8th-order-runge-kutta method. When the results of these two methods were compared, it was found that the 8th order method was no better than the earlier method. Therefore, the 4th-order method is recommended and only these results are presented in this paper.

The solution method for the pounding system was verified by using a numerical model from [4]. The SDOF elastic system with mass m = 350 Mg, elastic stiffness k_e = 10.5 MN/m, damping ratio ξ =0.02, separation gap a = 0.025 m and impact stiffness parameter β = 80 kN/mm$^{3/2}$ was used as a verification example. Two cases of sine excitations with 2 HZ and 0.67 HZ sharing a common magnitude of 0.1 g were each applied separately. The displacement and acceleration responses, and pounding force results calculated in this paper are same as those found in [4]. The results in this literature are not shown in this paper due to limited space.

3. Wavelet Transform and Scalogram

The wavelets $\psi_{a,b}(t)$ generated by dilation and translation from the analyzing wavelet $\psi(t)$ are defined below

$$\psi_{a,b}(t)=|a|^{-1/2}\psi\left(\frac{t-b}{a}\right) \tag{128}$$

where a is a scale parameter and b is a translation parameter.

$\psi(t)$ and $\psi_{a,b}(t)$ are usually called mother and son wavelets, respectively. It is supposed that $\psi(t) \in L^2(\mathbb{R})$ and the analyzing wavelet also satisfy the admissibility condition,

$$C_\psi = \int |\omega|^{-1} |\hat{\psi}(\omega)|^2 \, d\omega < \infty \tag{129}$$

where $\hat{\psi}(\omega) = \int \psi(t) e^{-i\omega t} dt$ is the Fourier transform. It can be derived from the above conditions that,

$$\int \psi(t) dt = 0 \tag{130}$$

Various wavelets have been developed, which include Haar, Morlet, Mexican Hat, Hermitian, and Daubechies wavelets. To select a proper mother wavelet is an important step. The Morlet wavelet is a complex function that can be considered as modulated Gaussian function by sinusoidal wave; it is a cosine signal decaying exponentially on both sides. It has the advantage of allowing trade between time and frequency resolution. It was proved to be an effective tool for feature extraction for mechanical vibration signals diagnosis [13-14]. It has also been applied in seismic signal detection [15]. Morlet wavelet is very similar to impulse component, which is symptom of damage in many dynamic signals. Because of these properties, the complex Morlet wavelet was chosen for this research, which is defined as

$$\psi(x) = \frac{1}{\sqrt{\pi f_b}} e^{2i\pi f_c x} e^{-\frac{x^2}{f_b}} \tag{131}$$

where f_b is a bandwidth parameter and f_c is a wavelet center frequency [16]. f_b = 1.5, f_c = 1 are used for the wavelet scalograms in sections 4 and 5 of this paper.

The wavelet transform is a linear transform that correlates a finite-energy function

x(t) with a series of oscillating functions $\psi_{a,b}(t)$, it is defined as

$$Wx(a,b) = |a|^{-1/2} \int x(t)\psi^*_{a,b}(t)dt > 0 \tag{132}$$

where the asterisk denotes a complex conjugate. The modulus is defined as

$$\|Wx(a,b)\| = (\mathrm{Re}^2[Wx(a,b)] + \mathrm{Im}^2[Wx(a,b)])^{1/2} \tag{133}$$

The phase is defined as

$$\varphi(a,b) = \arctan \frac{\mathrm{Im}[Wx(a,b)]}{\mathrm{Re}[Wx(a,b)]} \tag{134}$$

The modulus and phase were used in [17] to investigate nonlinear and chaotic behavior of structural systems.

The wavelet scalogram is defined as the square of the modulus of the wavelet transform and represents energy density that measures the energy of x(t) in the Heisenberg box of each wavelet $\psi_{a,b}$ centered in [18]:

$$P_W x(a,\xi) = \|Wx(a,b)\|^2 = \left\|Wx(a,\frac{\eta}{\xi})\right\|^2 \tag{135}$$

It is used for analysis of non-stationary signals and can be understood as a spectrum with a constant relative bandwidth. The scalogram is employed in this study to determine the occurrence of pounding for both numerical and experimental data.

4. Numerical Investigations

The results of pounding of an impact oscillator on its neighboring rigid barrier, as illustrated in Figure 54 , were investigated. The properties of the shorter concrete bridge segment in [3] were used for the SDOF structure: mass m = 1.2 $\times 10^6$ kg, elastic stiffness k_e = 107 MN/m, damping ratio ξ =0.05, and a natural period T = 0.67 seconds. Also used

were R_1 = 4.92 m from [7], Poisson ratio ν_1 = 0.15, compressive strength $f_c^{'} = 4000$ psi (27.58 MPa), and consequently concrete strength $E_1 = 57000\sqrt{4000}$ = 3.605 × 10^6 psi = 24.856 GPa. Substitute the above values into Eq. (127) to calculate the impact stiffness parameter, and it was found that β = 757 kN/$mm^{3/2}$. The separation distance a = 12.5 mm was used. The structure was excited by two single frequency sinusoidal ground motions with frequencies f_1 = 4 Hz and f_2 = 0.8 Hz, respectively: $\ddot{x}_g$ = - 0.1g × sin ($2\pi f_1 t$); $\ddot{x}_g$ = - 0.1g × sin ($2\pi f_2 t$). El Centro 1940 North-South component scaled to peak ground motion (PGA) of 0.1g and 0.05g, respectively, were also employed as ground excitations. All the sessions have durations of 31.14 seconds.

The responses of the pounding system were computed by the procedures discussed in section 2. The wavelet scalograms of the acceleration responses were calculated by the method expanded upon in section 3. The frequency axes of the scalograms are in log scale. The objective was to find a method to identify the presence of pounding from the time history signals, i.e., the displacement/velocity/acceleration. Both the amplitude spectra and scalogram were calculated from acceleration responses. The pounding forces computed numerically address the actual condition but were treated as unknown throughout the identification process.

The results of responses due to stationary sinusoidal excitation will be discussed first. Figure 55 shows the responses, single-sided amplitude spectra and scalogram for the case f_1 = 4 Hz, at which pounding forces were all computed to zero during this session, thus indicating no pounding presence. The displacement and acceleration were able to maintain the approximately sinusoidal shapes after the first few seconds of oscillation. The single-sided amplitude spectrum showed the predominant frequency is

approximately same to the excitation frequency of 4 Hz. The scalogram was able to register a clear picture of energy distribution with respect to time and frequency.

Figure 56 shows the responses, pounding forces, single-sided amplitude spectra and scalogram for the case f_1 = 0.8 Hz, which is closer to the natural frequency of the SDOF structure, and consequently generates larger displacement and acceleration responses. From Figure 56(a-b), the displacement and acceleration became periodical signals after about 5 seconds. Although the responses were not normal, as expected from the non-pounding responses, there were no acceleration spikes found and it was uncertain whether pounding had occurred at that time. The pounding forces as shown in Figure 56 (c) indicate the exact time and duration of the poundings. The spectrum in Figure 56 (d) shows many prominent frequencies instead of only the excitation frequency, and in addition the predominant frequency is 1.6 Hz instead of the excitation frequency 0.8 Hz, which indicates that pounding might have occurred at this time. But this judgment needs a priori knowledge of the structure and the excitation, and even in this case, it is not convincing and clear. Compared with the non-pounding scalogram shown in Figure 55 (d), the scalogram in Figure 56 (e) has many abrupt changes of energy with respect to the frequency. When Figure 56 (e) and Figure 56(c) are compared, it is obvious that these changes occur at the time of pounding. Further, the changes of frequency contents indicate the magnitude of the pounding force. Therefore, the scalogram is able to indicate the presence of pounding, the time and relative magnitude of the pounding occurrence from the acceleration response without a priori information.

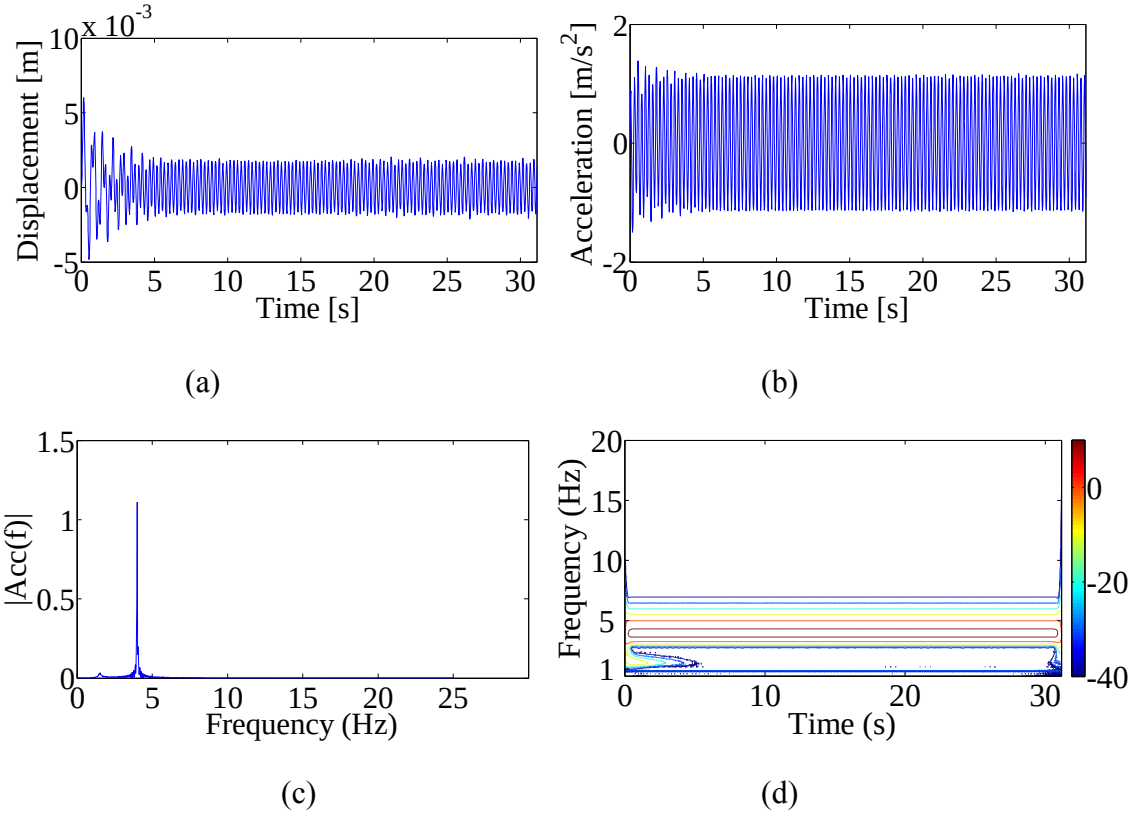

Figure 55. The responses of the SDOF structure during sinusoidal excitation f_1 = 4 Hz, no pounding occurred: (a) Displacement; (b) Acceleration; (c) Single-sided amplitude spectrum of acceleration. (d)) Wavelet scalogram of acceleration response.

The results of responses due to non-stationary earthquake excitation were also analyzed. Figure 57 and Figure 58 show the results due to earthquake excitation with different PGAs. The earthquake record of 1940 El Centro north-south component scaled to PGA of 0.1g is illustrated in Figure 57 (a), which contains its most energy approximately in the frequency range of 0.2~10 Hz. It was observed that there are spikes in the acceleration histories shown in Figure 57 (c), which indicates that the pounding may have occurred. The pounding forces shown in Figure 57 (d) illustrate the pounding present for this excitation. Unfortunately, the pounding cannot be identified by amplitude spectra very well. The wavelet scalogram for PGA = 0.1g is illustrated in Figure 57 (f) and the scalogram for PGA =0.05g that does not generate pounding is shown in Figure 58

(f). When Figure 58 (a) and Figure 57(d) are compared, it is clear the higher frequencies determined by the scalogram are associated with the times of most intense pounding. The scalogram in Figure 58 (b) used in the non-pounding portion of the experiment does not show these types of changes, which additionally proves that the scalogram is capable of detecting pounding. It can be concluded that acceleration spikes and wavelet scalogram can in fact identify pounding effectively.

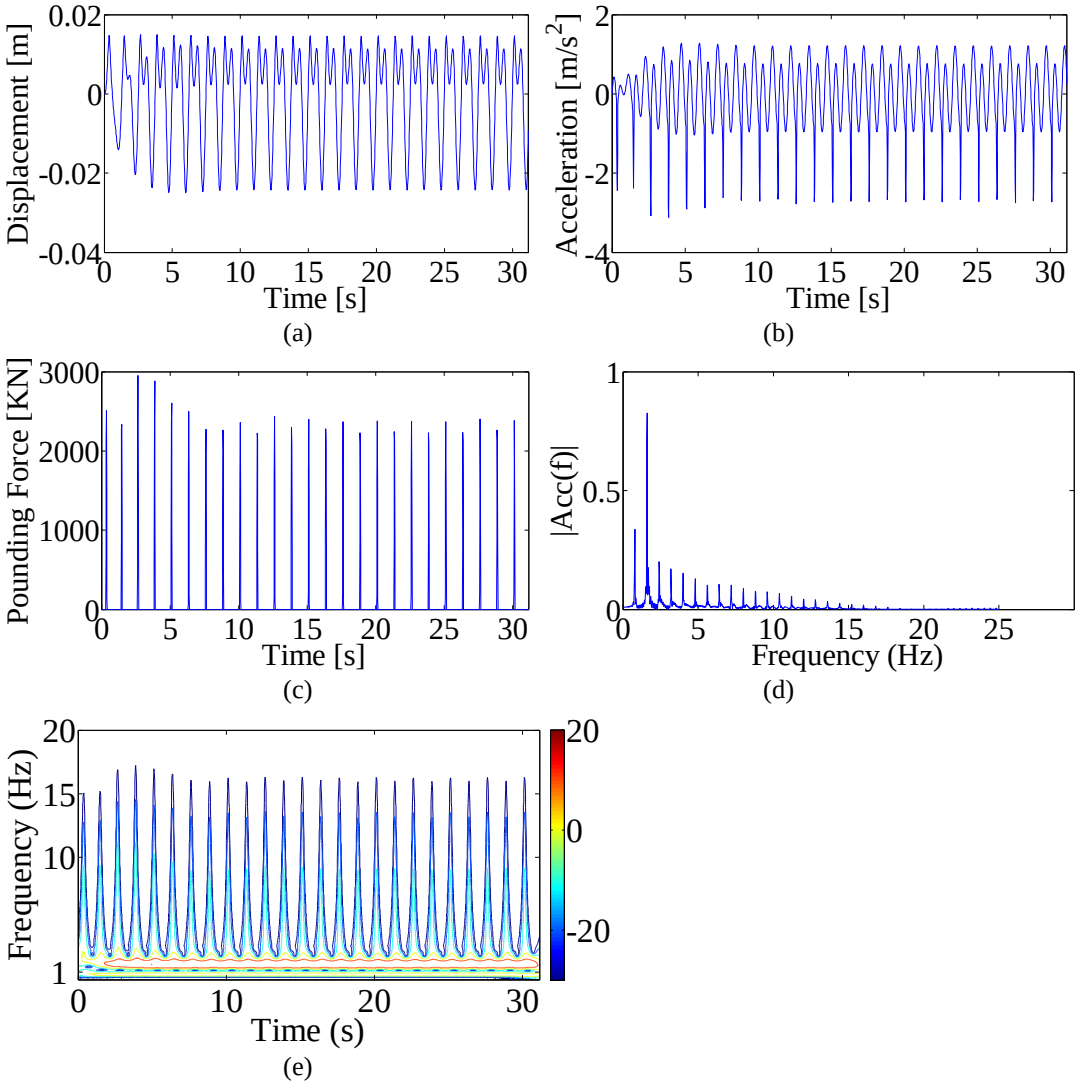

Figure 56. The responses of the SDOF structure during sinusoidal excitation f_2 = 0.8 Hz: (a) Displacement; (b) Acceleration; (c)Pounding force; (d) single-sided amplitude spectrum of acceleration; (e) Wavelet scalogram of acceleration.

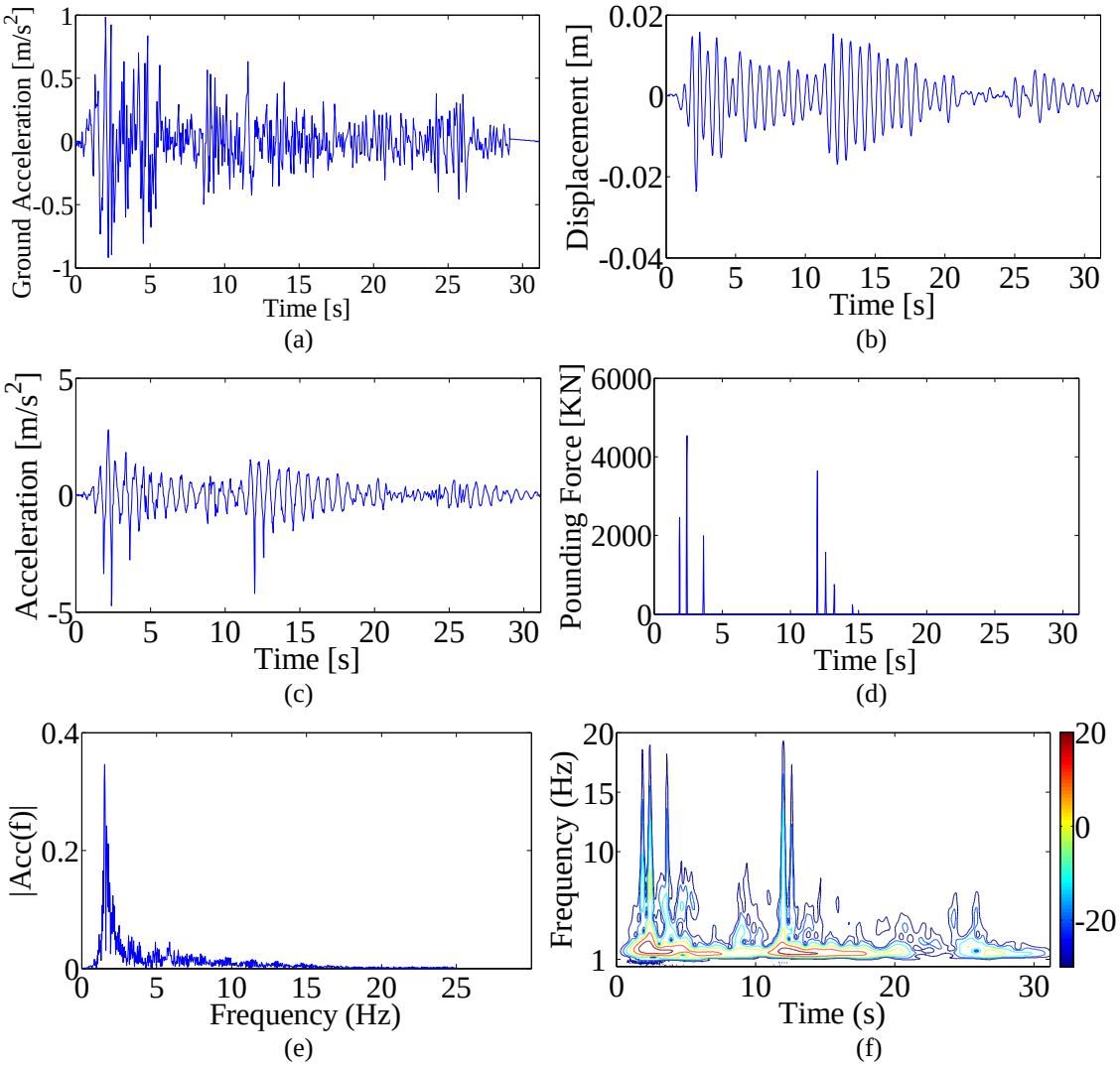

Figure 57. The El Centro earthquake excitation and responses of the SDOF structure: (a) Ground acceleration, PGA = 0.1g (b) Displacement response; (c) Acceleration response; (d)Pounding force; (e) single-sided amplitude spectrum of the acceleration; (f) Wavelet scalogram of acceleration.

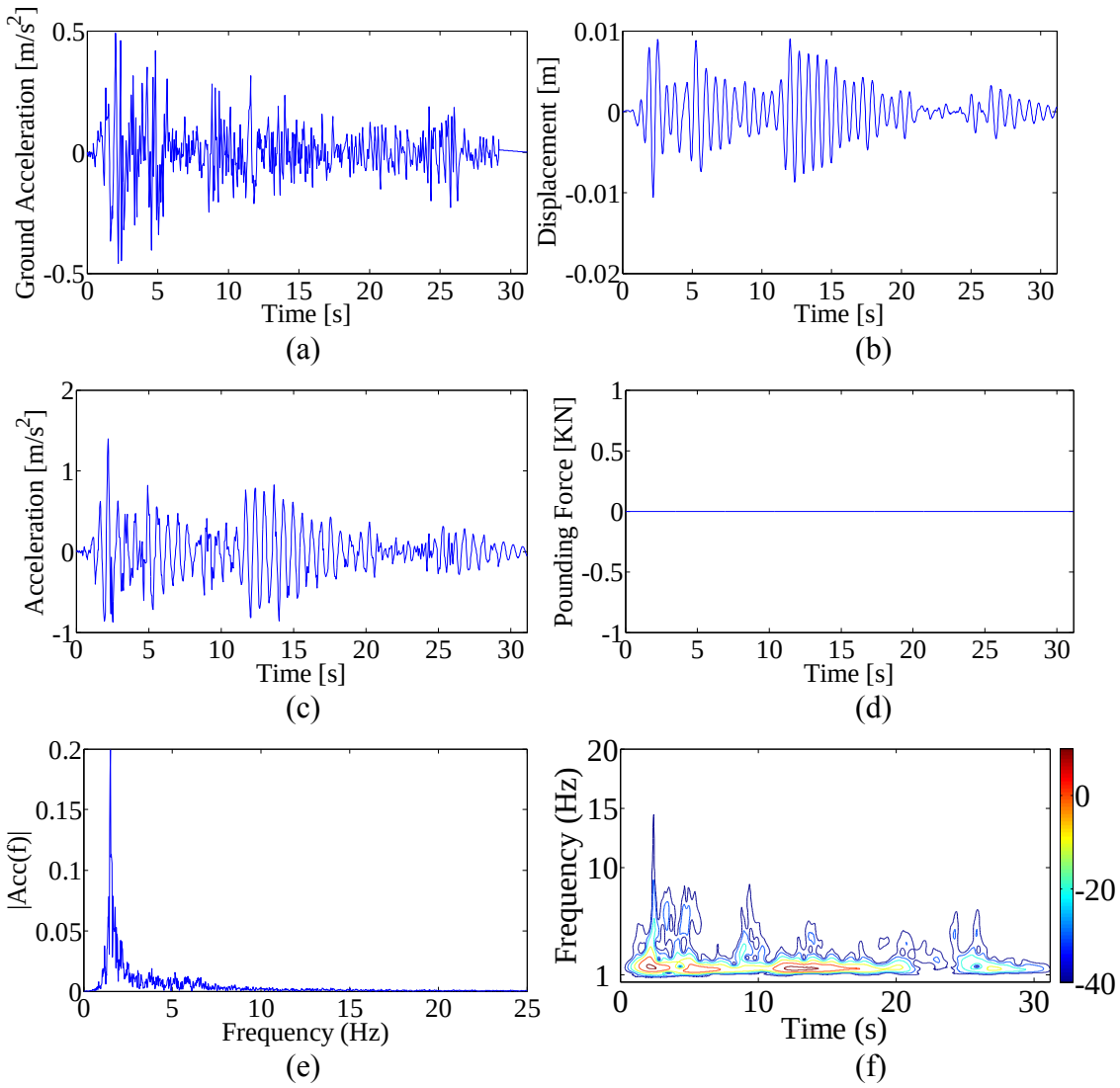

Figure 58. The El Centro earthquake excitation and responses of the SDOF structure: (a) Ground acceleration, PGA = 0.05g (b) Displacement response; (c) Acceleration response; (d)Pounding force; (e) single-sided amplitude spectrum of the acceleration; (f) Wavelet scalogram of acceleration.

5. Experimental Data Analysis

A series of shaking table tests were conducted on seismic pounding of high-pier bridge by Meng et al. [19] at Institute of Engineering Mechanics, China Earthquake Administration in 2009. The measured accelerations were analyzed in this paper by using a wavelet scalogram to verify the ability of scalograms to identify pounding.

5.1 Shake table tests on seismic pounding of high-pier bridge models

A high-pier bridge model with one main span and two approach spans was constructed as illustrated in Figure 59, the prototype of it is a high-pier bridge in Yunan, China. The superstructures and the 1.50 m tall piers were built with steel plates and pipes respectively. The main span and approach spans have different sizes and different ballast masses were added to satisfy the similitude laws. Consequently they have different natural frequencies. The gaps betwwen the main span and the approach spans are 0.01m.

The bridge model was placed on the 5m × 5m three-dimensional shake table. Seven accelerometers, 11 displacement sensors, and 20 strain gauges were attached to the bridge model. Two sets of dynamic tests were conducted on this model. The first tests were performed on the above described bridge model, and the second tests were implemented on the above model installed with shape memory alloy metal rubber dampers (SMAMRD). The SMAMRD reduced the pounding effects significantly. The applied ground motions simulated the El Centro, Taft earthquake and artificial ground motions for both test sets with same PGAs. In this study, the accelerations a4 from the El Centro ground motion tests were analyzed. The PGA of the El Centro table motion was 0.22g for both the test sets with and without SMAMRD. A typical table acceleration is shown in Figure 60.

5.2 Pounding identification by wavelet scalogram

The responses of accelerations recorded by accelerometer a4 for both the test sets with and without SMAMRD were analyzed by wavelet scalograms. The results of the two tests are shown in Figure 61 and Figure 62 respectively. The analysis methods were

the same as those used in numrical investigations.

From the acceleration response, single-sided amplitude spectra and the scalogram in Figure 61 for the test set with SMAMRD, it was observed that in the ranges near 3 and around 18 seconds, the peak acceleration was doubled, and the scalogram frequencies were 3 times as high as other ranges. The changes in the scalogram together with the acceleration spikes indicated clearly that the pounding occurs at the time ranges around 3 and 18 seconds. However, no clear pounding information can be drawn from the spectra.

From the response results shown in Figure 62 for the test set without SMAMRD, it was observed that in the time ranges between 3.5~9.2, 15.0, 18.5~22, and 24.0 seconds, the peak values of acceleration became about 3 times as those of other time ranges and the scalograms extended to higher frequencies about 5 times those of other time ranges. Therefore, it can be concluded that the pounding occurs at the above time ranges by analyzing the acceleration spikes and wavelet scalograms. However, the pounding information from the spectrum was inconclusive.

Both test sets in Figure 61 and Figure 62 refer to the same El Centro ground motion with the same PGA, Comparing the times of pounding and the scalogram that represented the energy density in Figure 61 (c) and Figure 62 (c), the times of pounding occurrence and the scalogram magnitudes in Figure 62 (c) are more frequent and larger than those of Figure 61 (c). The scalogram in Figure 62 is extended to much higher frequencies of 100 Hz compared to about 37 Hz in Figure 61. These results are consistent with the conclusion in [19] that the SMAMRD can decrease pounding effects substantially.

Figure 59. The pounding models of high-pier Bridge under shaking table tests.

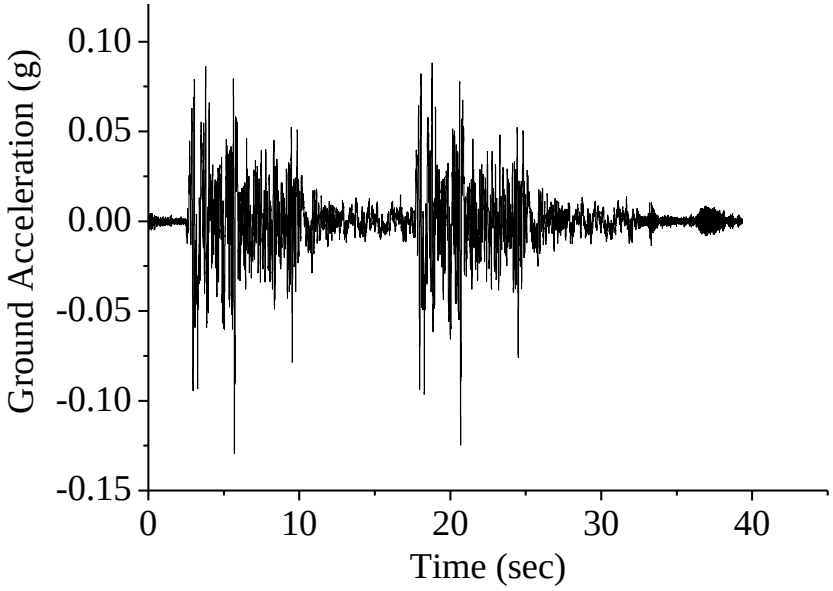

Figure 60. A typical table acceleration for the shake table tests.

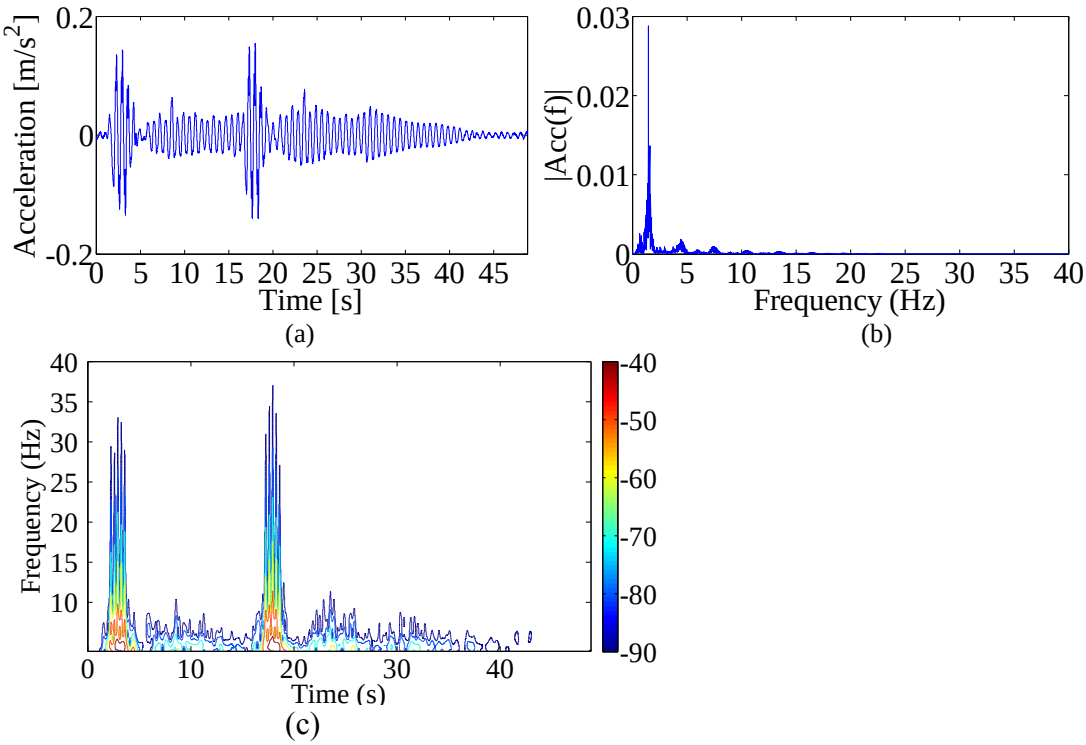

Figure 61. The response of the main bridge at Accelerometer a4 with SMAMRD: (a) Acceleration response a4; (b) single-sided amplitude spectrum of the acceleration a4; (c) Wavelet scalogram of a4.

6. Conclusions

In this paper, the pounding identification by wavelet scalogram was examined by numerical studies as well as experimental studies.

In the numerical studies, the Hertz contact model was carefully integrated into the one-sided pounding system between an elastic SDOF concrete structure and a rigid barrier. The pounding forces, displacement, and acceleration of the pounding system were solved from the numerical models for both stationary sinusoidal and non-stationary earthquake excitations. Acceleration spikes were present in the earthquake excitation case, but not in the harmonic one. The wavelet scalogram proved its ability to identify pounding occurrences in both cases. It can also be used to indicate the time of pounding occurrence and the approximate severity of each pounding session.

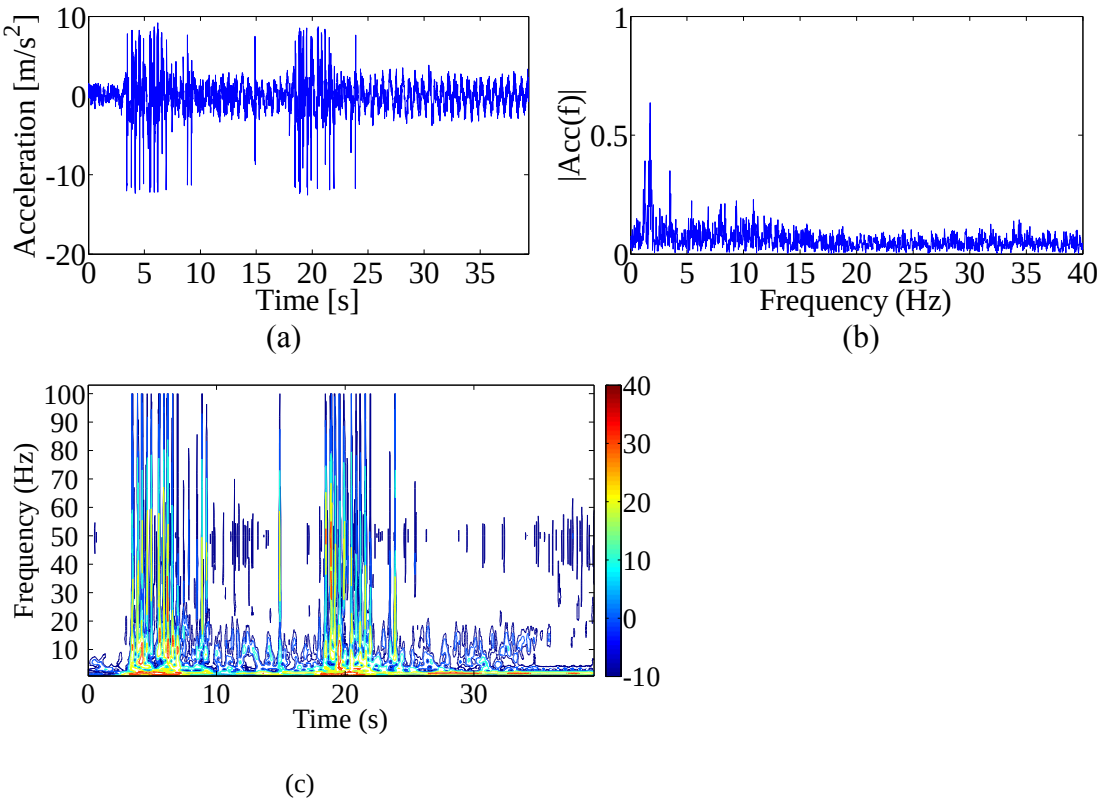

Figure 62. The response of the main bridge at Accelerometer a4 without SMAMRD: (a) Acceleration response a4; (b) single-sided amplitude spectrum of the acceleration a4; (c) Wavelet scalogram of a4.

In the experimental studies, the acceleration data from two sets of shake table tests on a steel bridge model with and without SMAMRD were analyzed. These tests included pounding sessions between the different components of the bridge for both sets of tests. The wavelet scalogram of the accelerations identified the pounding very effectively, which verified the conclusions from the numerical studies. The acceleration spikes were also able to indicate the pounding in this case.

We can come to the conclusion that the wavelet scalogram is capable of indicating the presence of structural pounding quite well. The acceleration spikes can be used together with the wavelet scalogram for pounding identification. Further analytical and experimental studies on more practical cases are underway.

REFERENCES

[1] R. Jankowski, K. Wilde, Y. Fujino, Pounding of superstructure segments in isolated elevated bridge during earthquakes, *Earthquake Engineering & Structural Dynamics* 27 (1998) 487-502.

[2] M.J.N. Priestley, F. Seible, G.M. Calvi, *Seismic Design and Retrofit of Bridges*, John Wiley and Sons, Inc, 1996.

[3] P.K. Malhotra, Dynamics of seismic pounding at expansion joints of concrete bridges, *ASCE Journal of Engineering Mechanics* 124 (1998) 794-802.

[4] C.P. Pantelides, X. Ma, Linear and nonlinear pounding of structural systems, *Computers & Structures* 66 (1998) 79-92.

[5] R.O. Davis, Pounding of buildings modeled by an impact oscillator, *Earthquake Engineering & Structural Dynamics* 21 (1992) 253-274.

[6] K.T. Chau, X.X. Wei, Pounding of structures modelled as non-linear impacts of two oscillators, *Earthquake Engineering & Structural Dynamics* 30 (2001) 633-651.

[7] S. Muthukumar, R. DesRoches, A Hertz contact model with non-linear damping for pounding simulation, *Earthquake Engineering & Structural Dynamics* 35 (2006) 811-828.

[8] J.S. Walker, *A Primer on Wavelets and Their Scientific Applications*, Chapman & Hall/CRC, Boca Raton, 1999.

[9] Z.K. Peng, F.L. Chu, Application of the wavelet transform in machine condition monitoring and fault diagnostics: a review with bibliography, *Mechanical Systems and Signal Processing* 18 (2004) 199-221.

[10] K. Gurley, A. Kareem, Applications of wavelet transforms in earthquake, wind and ocean engineering, *Engineering Structures* 21 (1999) 149-167.

[11] J.G.M. Van Mier, A.F. Pruijssers, H.W. Reinhardt, T. Monnier, Load-time response of colliding concrete bodies, *Journal of Structural Engineering* 117 (1991) 354-374.

[12] W. Goldsmith, *Impact: The Theory and Physical Behaviour of Colliding Solids*, Annotated ed., Dover Publications, Mineola, 2001.

[13] J. Lin, L. Qu, Feature extraction based on morlet wavelet and its application for mechanical fault diagnosis, *Journal of Sound and Vibration* 234 (2000) 135-148.

[14] Y.-T. Sheen, C.-K. Hung, Constructing a wavelet-based envelope function for vibration signal analysis, *Mechanical Systems and Signal Processing* 18 (2004) 119-126.

[15] C.C. Liu, Z. Qiu, A method based on Morlet wavelet for extracting vibration signal envelope, *Proceedings of the fifth International Conference on Signal Processing*, 2000, 337-340.

[16] A. Teolis, *Computational Signal Processing with Wavelets*, first ed., Birkhäuser, Boston, 1998.

[17] L.A. Wong, J.C. Chen, Nonlinear and chaotic behavior of structural system investigated by wavelet transform techniques, *International Journal of Non-Linear Mechanics* 36 (2001) 221-235.

[18] S.G. Mallat, *A Wavelet Tour of Signal Processing*, second ed., Academic Press, San Diego, 1999.

[19] Q. Meng, M. Zhang, G. Zhou, The study on SMA pseudo-rubber metal damper's control efficiency on aseismic pounding in high-pier bridge in shaking table testing, *Advanced Materials Research* 163-167 (2010) 4429-4441.

CHAPTER VI

CONCLUSION AND FUTURE STUDY

1. Conclusion

This thesis studied the structural identification and damage detection for civil engineering structures. Various structural identification and damage detection methods were explored. Experimental as well as numerical studies have been carried out to solve several practical engineering problems, e.g., the delamination of a concrete bridge deck. The research work throughout this thesis can be highlighted as follows:

(a) Various state-of- the-art identification methods were explored, which included classical peak-picking, frequency domain decomposition, stochastic subspace identification, extended Kalman filter, and wavelet transform. These methods were investigated at length and compared in Chapters II - V.

(b) Finite element models of concrete slabs with delamination damage were constructed by ANSYS software to simulate real ones. The modeling was justified by comparing the modal characteristics with those identified from the experimental models (see Chapter IV). Finite element models for shear building, truss, and frame structures were established by programming and the dynamic responses were computed using numerical methods (see Chapter II and III). Numerical studies were also conducted to integrate the Hertz Impact Model in the modeling of pounding systems (see Chapter V).

(c) The experimental studies were carried out specifically for the research while actual acceleration measurements were obtained from a real-time monitoring system on a highway bridge and used in this study (see Chapter II). Experimental modal testing was conducted upon four concrete models with delamination damage in the laboratory (see

Chapter IV). The real measurements from shake table tests on a steel bridge were used (see Chapter V).

The main conclusions of the thematic research for this thesis are summarized below:

(1) Data-driven stochastic subspace algorithms were used for modal identification of a numerical truss bridge with abrupt damage and a real girder highway bridge without damage by using acceleration responses of these bridges. The algorithm was combined with stabilization diagrams to determine the physical modes and exclude the spurious modes (see Chapter II).

It was observed from the stabilization diagrams of frequencies and damping ratios for the truss that the uncertainties are very low and the identified frequencies correspond well with the exact values with only 0.16% error for the 1st frequency, and most errors of other frequencies are less than 4%. For damping ratios, 5 values were identified with percent errors less than 2.5%, but another 5 were lost. The mode shapes were also obtained and shown to be correct and able to indicate the damage.

In the application to the real bridge, observed from the stabilization diagrams, there are many spurious modes. The identified frequencies corresponded with the exact values; the errors for the first 18 frequencies were less than 5%.

Generally, the SSI combined with stabilization diagrams is quite effective in identifying the frequencies, damping coefficients, and mode shapes. The algorithm is also effective in identifying closely-spaced modes.

A subspace identification algorithm, N4SID, was also examined through its application to the modal identification of the highway bridge using output only data. It

extracted frequencies well with a percent error of less than 8%. Since it is not computational efficient, N4SID is not recommended for identification of large systems.

(2) The performance of the adaptive Kalman filter in substructure identification was investigated by performing numerical studies on a shear building, a plane frame building, and a plane truss bridge (see Chapter III). These structures endured abrupt damages during the external excitation. The masses and the simulated acceleration responses were known and used to identify the unknown parameters, such as, stiffness and damping. The results revealed that, if given a close initial estimate, the stiffness can be identified quite accurately and the abrupt changes of stiffness can be tracked very well; the damping can also be identified but with a larger error. When output noise was added, the method was still effective for identifying the stiffness and damping, though with lower accuracy.

Wavelet transform was proposed as a method for identifying substructural damage. The results showed that the wavelet scalograms of accelerations can detect the changes of structural parameters and also approximately locate the damage.

(3) This thesis researched the delamination detection of concrete structures by modal identification from output-only vibration measurements (see Chapter IV). The feasibility of this was investigated through numerical as well as experimental studies.

The delaminations with different sizes and locations were introduced into the concrete slab, and the parameter studies on the effects of delamination on modal characteristics were performed through finite element modeling. It can be concluded from the results that the delamination sizes and locations can have significant influence on modal characteristics; consequently changes in the modal characteristics can indicate and

locate the development of delamination well.

Experimental modal testing on reinforced concrete slabs with different delaminations was conducted. The modal characteristics were extracted from the dynamic responses by peak-picking, frequency domain decomposition, and stochastic subspace identification methods. From the analyses of the results, it was found that the experiments verified the findings of the numerical studies. Finite element models for the experimental models were developed using ANSYS. These modeling were validated to be able to approximately simulate the real models, while the exact models are not obtained due to the complex and unpredictable boundary conditions of the experimental tests.

The research provided an efficient way for delamination detection of bridge decks using vibration-based real-time health monitoring systems.

(4) A statistical analysis was done to study the influence of temperatures on frequencies based on one-year ambient vibration data from a concrete bridge. The frequencies and temperatures were correlated by nonlinear as well as linear curve fitting. The multiline regression models exhibited a specific trend for each mode, which is useful for separating changes in frequencies that are normal due to temperature changes from those due to damage to the structure.

(5) A pounding system was modeled using the Hertz contact model. Shake table tests of a steel bridge with pounding was conducted by a collaborator and the test data was investigated (Chapter V). The wavelet scalogram was applied to the simulated response from the numerical model and the experimental data from the shake table tests. The results showed that wavelet scalogram can indicate the occurrence of structural pounding well.

2. Future Study

Further research is necessary in order to improve damage detection methods and more experimental tests are needed. Some suggestions for future study are discussed below.

(i) It was found that the subspace identification algorithm needs a larger model order number than the theoretical value (2N for an N-DOF system). While the increase of system order can improve the identification ability, the computation time also would increase significantly, which may become an issue for a large system. In this study, only the 1st mode shapes of the truss bridge before and after damage were investigated and found to be reasonable, the other mode shapes have yet to be surveyed. To obtain better results, a denser layout of sensors is necessary.

(ii) For substructure identification, the experiments in the laboratory and field tests are necessary. The accuracy and robustness of the methods need to be improved. For example, the results should not depend so much on the initial hypothesis, and the convergence times should be reduced. As for the substructural damage identification using wavelet analysis, further study is necessary for obtaining quantitative results and clearer interpretations with physical meanings.

(iii) For the study on delamination detection by modal identification, further study is needed to develop more sensitive damage indicators. More controllable and ideal boundary conditions should be enforced for the experimental models. And bridge decks with actual delaminations would be ideal for tests. For finite element modeling, more accurate simulations of delamination need to be developed.

(iv) Along with frequencies, the variations of damping ratios and mode shapes

due to the changes in temperature should be investigated. Installations of temperature sensors on bridges are highly recommended to measure exact temperatures.

(v) Further analysis on pounding modeling is needed to develop more practical and complex pounding systems, which can be used for real world scenarios.

APPENDIX

Appendix A. Supplemental Results for the Modal Analysis of the Numerical Delaminated Concrete Models and the Experimental Delaminated Concrete Specimens

This section shows additional results of modal analysis of the delamination models to Chapter IV.

A.1 Numerical Study

The 1st - 6th mode shapes for the undelaminated concrete models and those with 1/12, 1/6, 1/4, 1/3 symmetrical, 1/3 unsymmetrical and 1/2 delaminations are illustrated in Figure 69. The following results provide more in depth results of modal analysis of numerical studies to verify the conclusions presented in Chapter IV. The modal order number is the sub number minus 1.

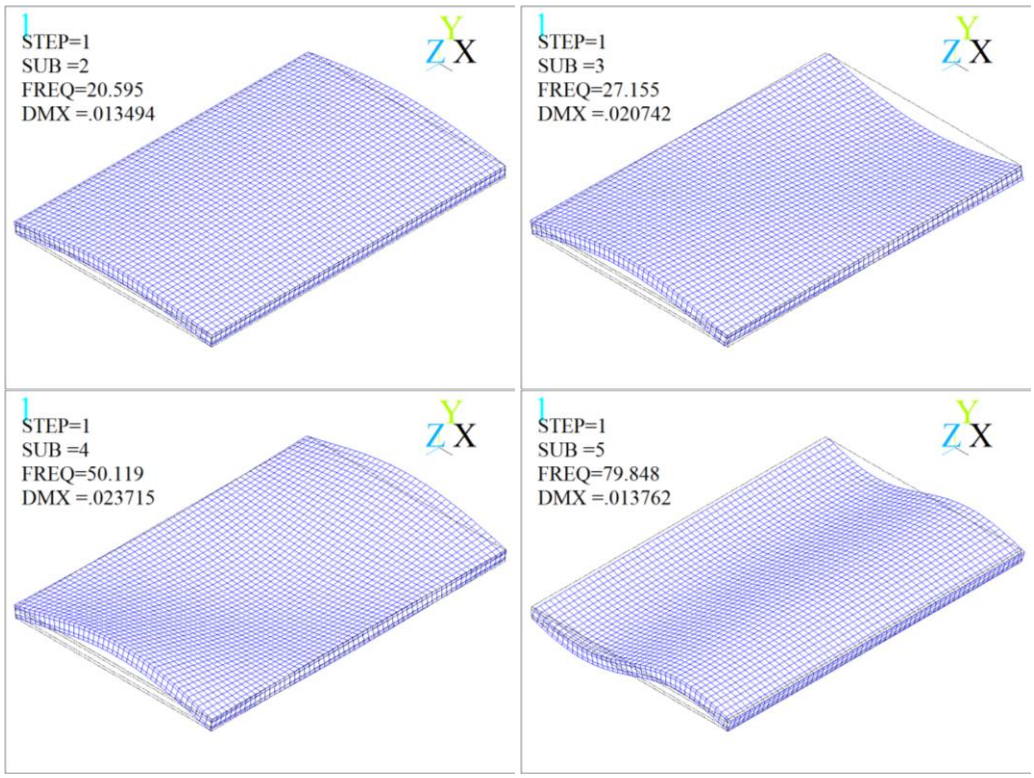

Figure 63. The 1st - 6th mode shapes for the non-delaminated model.

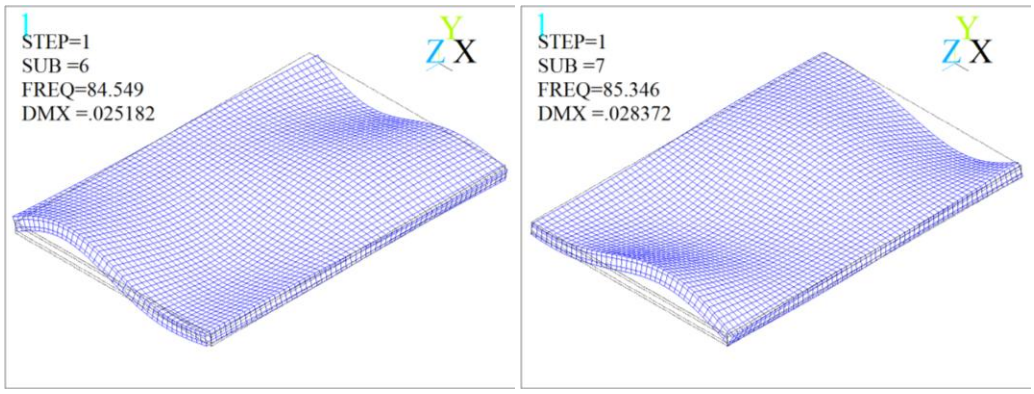

Figure 63. Cont'd

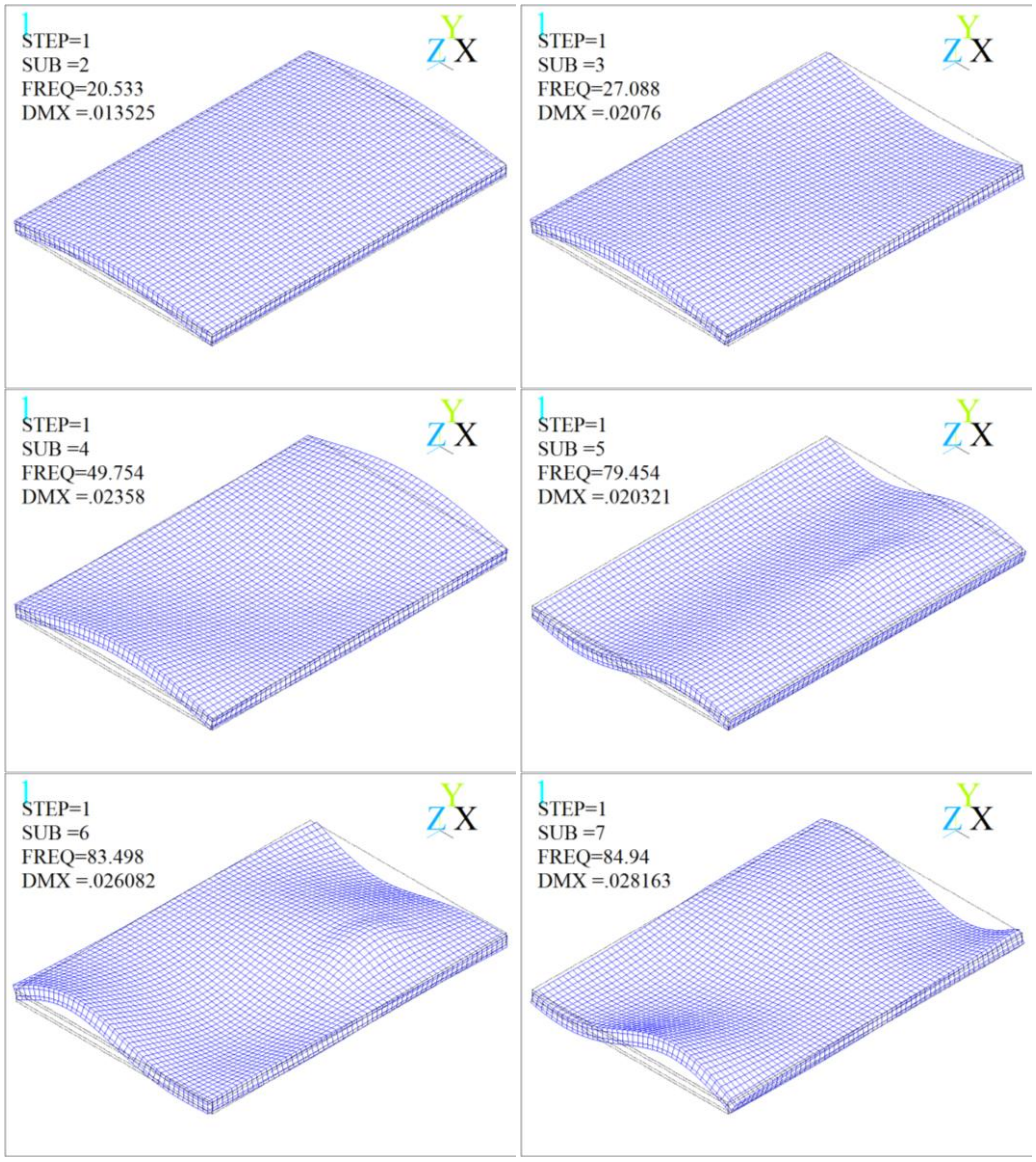

Figure 64. The 1st - 6th mode shapes for the 1/12 delaminated model.

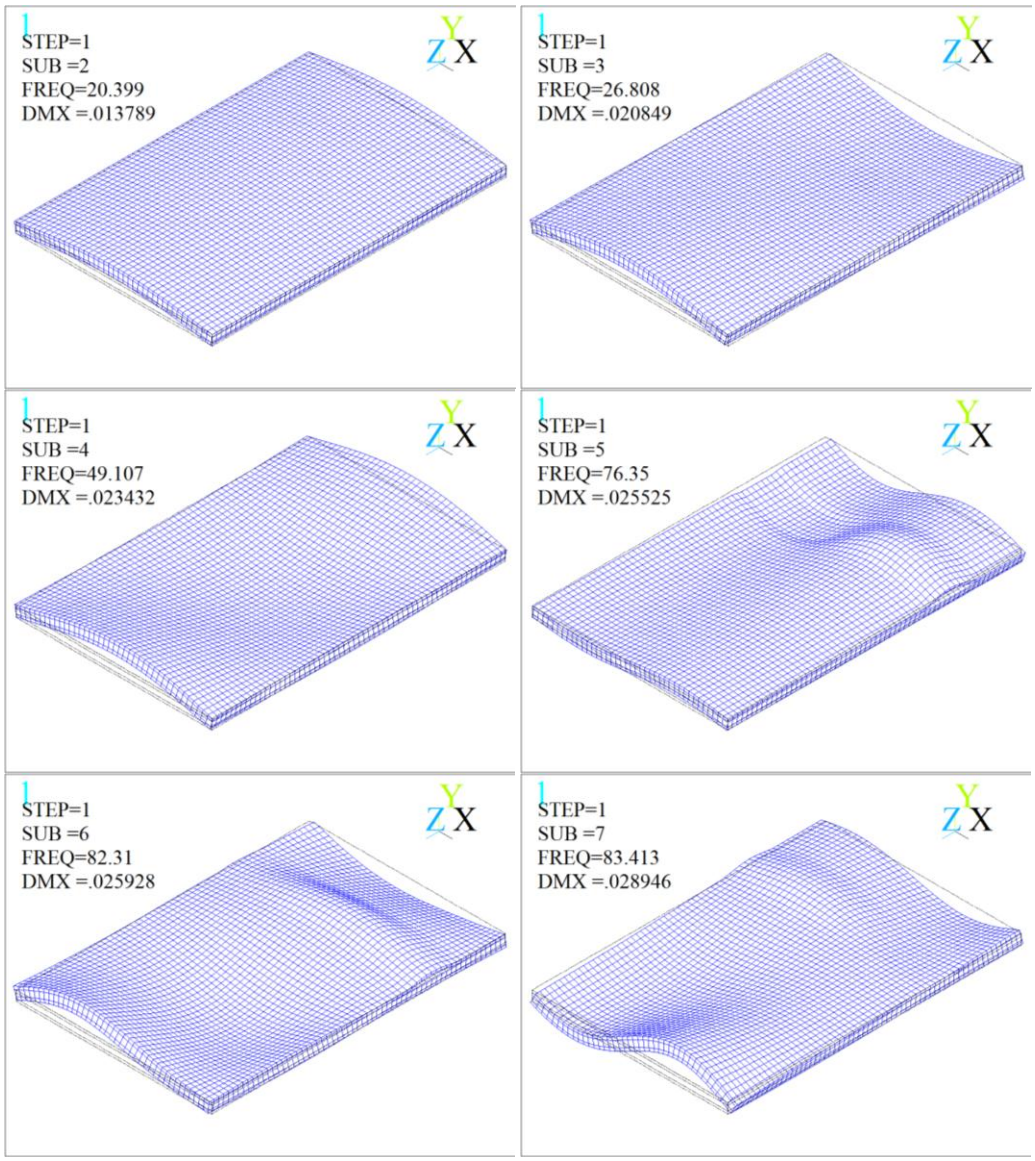

Figure 65. The 1st to 6th mode shapes for the 1/6 delaminated model.

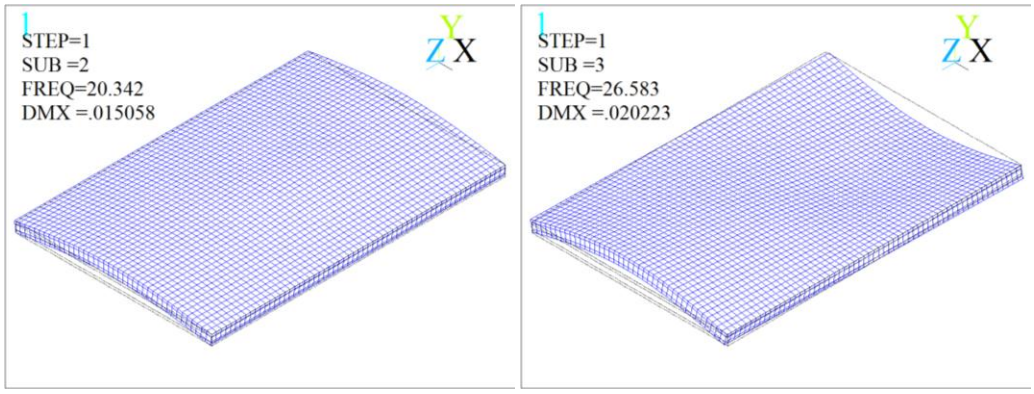

Figure 66. The 1st - 6th mode shapes for the 1/4 delaminated model.

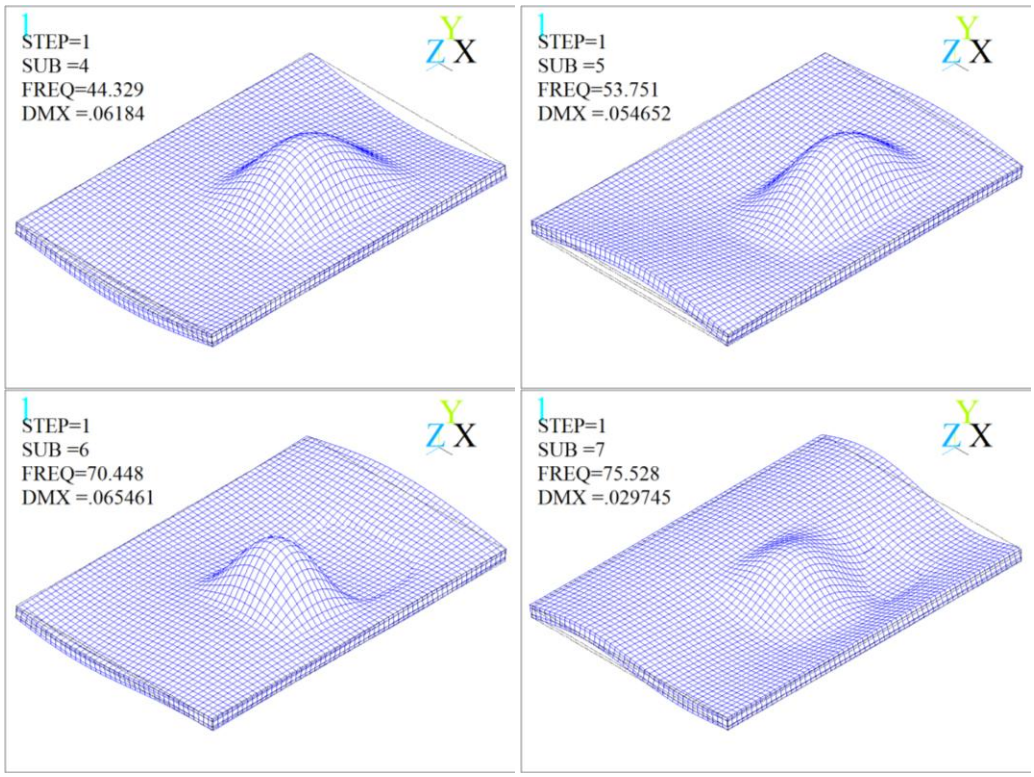

Figure 66. Cont'd.

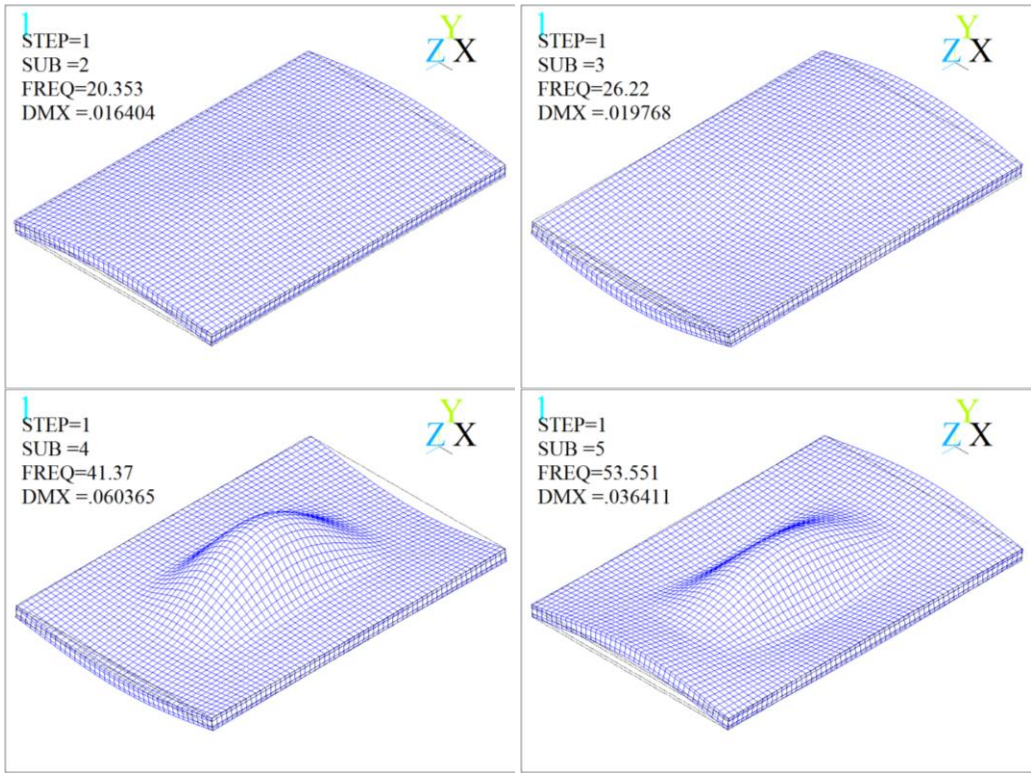

Figure 67. The 1st - 6th mode shapes for the 1/3 symmetrical delaminated model.

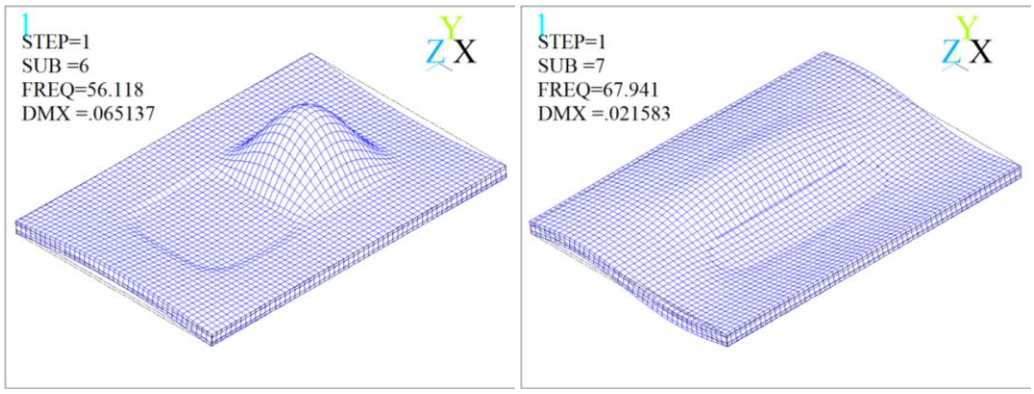

Figure 67. Cont'd.

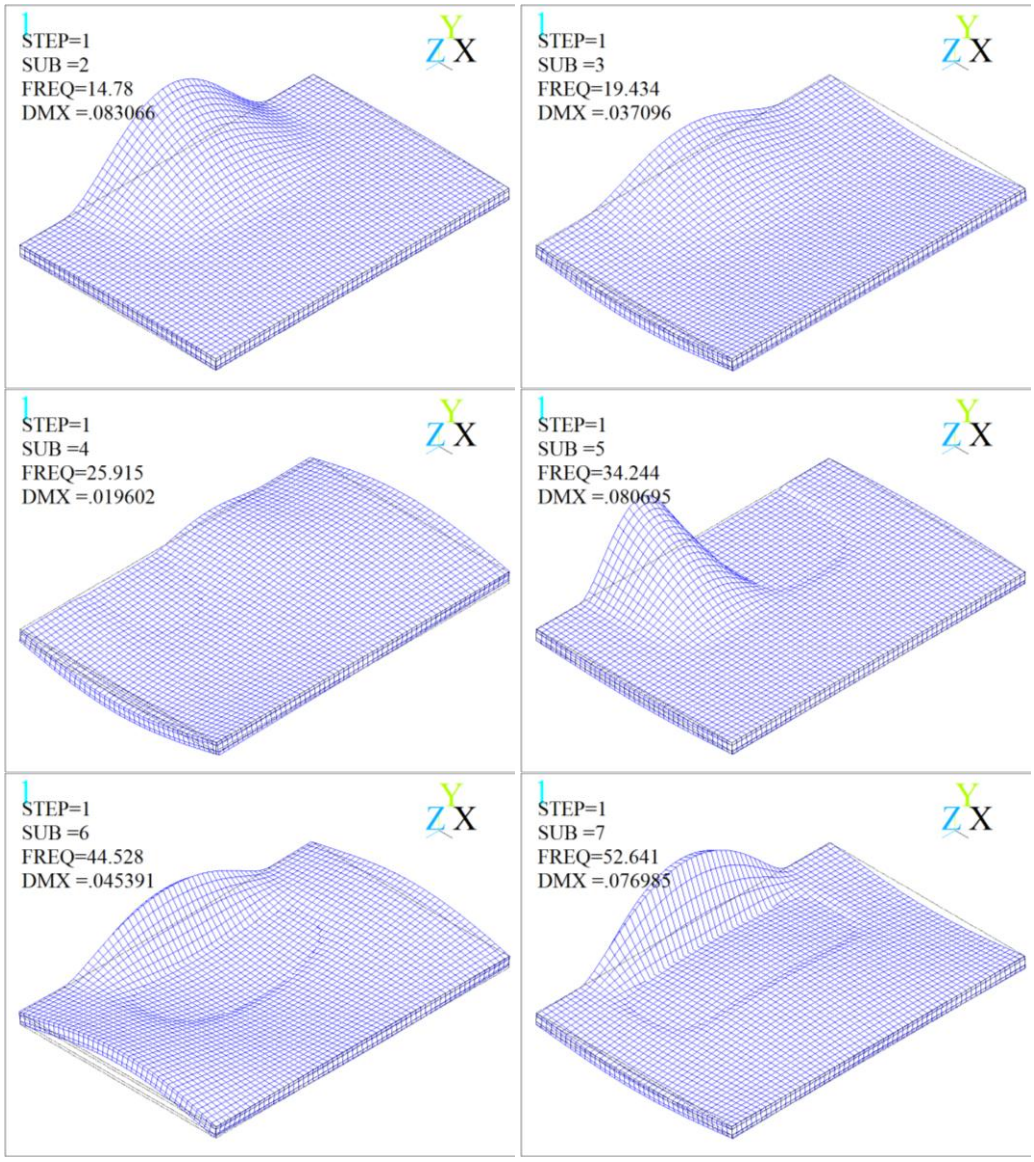

Figure 68. The 1st - 6th mode shapes for the 1/3 unsymmetrical delaminated model.

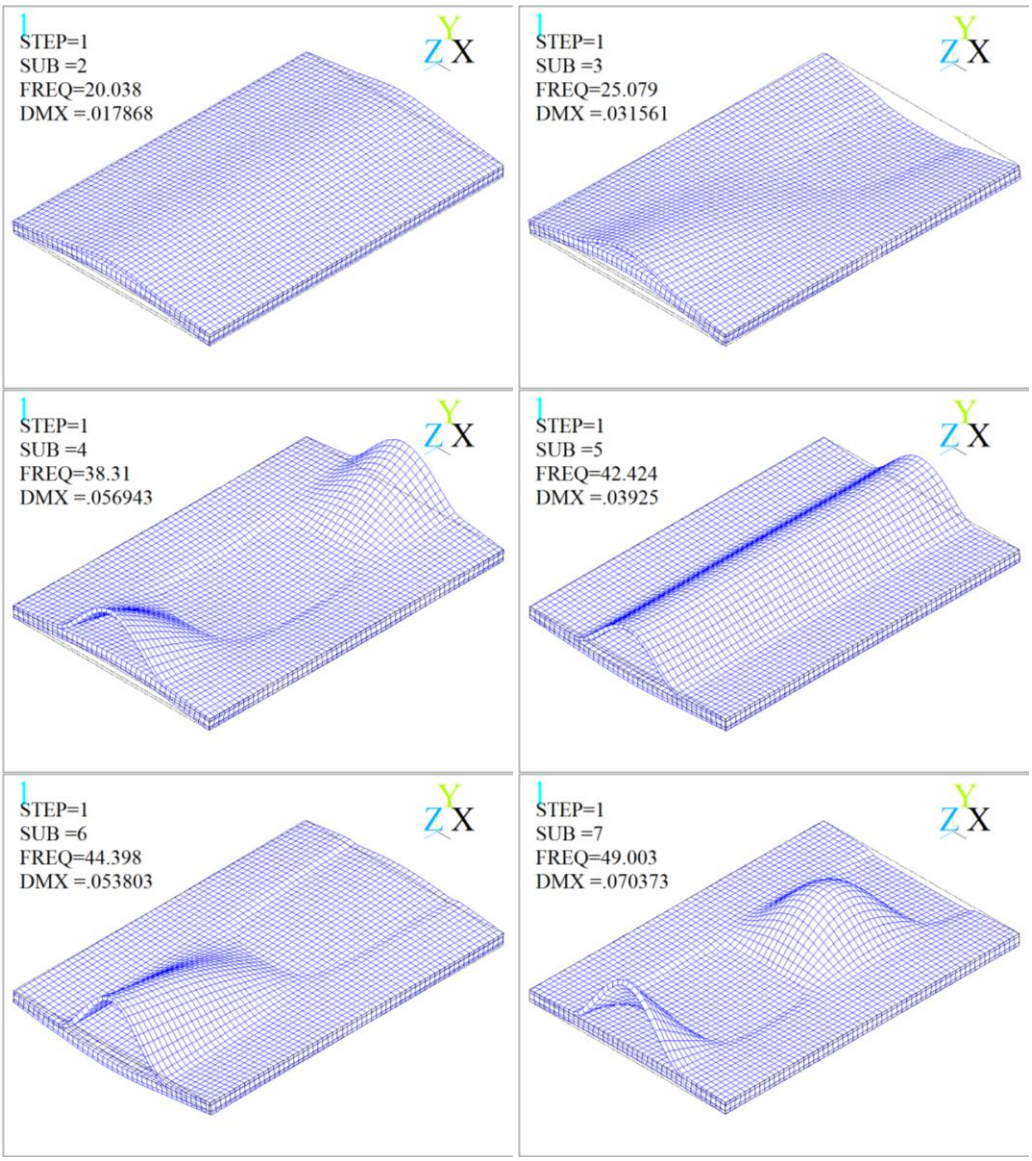

Figure 69. The 1st - 6th mode shapes for the 1/2 delaminated model.

A.2 Experimental Study

This section presents additional results of the dynamic tests of undelaminated and delaminated concrete slabs due to impact and swept sine excitations. The modal frequencies identified by the three identification methods from dynamic tests due to impact and swept sine excitations are listed in Table 26 and Table 27 respectively. Figure 70 and Figure 71 show the comparisons of mode shapes by FDD and SSI identification

methods from the response measurements due to impact excitation and swept sine excitation by instrumented hammer respectively.

The results extracted from the response measurements due to impact and swept sine excitations are consistent with those from random excitation shown in Chapter IV. Thus the conclusions in Chapter IV are further verified.

Table 26. Modal frequencies identified by PP, FDD and SSI (i = 400, n = 60) methods from experimental specimens under impact excitation.

0%-Delaminated	PP (HZ)	15.75	20.75	31.47	68.47	83.63	165.73
	FDD (HZ)	15.76	20.76	31.52	67.53	82.54	165.08
	SSI (HZ)	15.78	20.70	31.62	67.62	82.71	165.78
22.2%-Delaminated	PP (HZ)	14.75	-	26.91	50.97	-	-
	FDD (HZ)	14.76	-	27.01	50.77	-	-
	SSI (HZ)	14.66	-	26.87	50.58	-	-
51.9%-Delaminated	PP (HZ)	14.09	-	27.35	-	-	-
	FDD (HZ)	14.01	-	27.26	-	-	-
	SSI (HZ)	14.05	-	27.44	-	-	-
74.1%-Delaminated	PP (HZ)	9.16	-	24.16	45.22	-	86.97
	FDD (HZ)	9.25	-	24.26	44.52	-	84.54
	SSI (HZ)	9.15	-	24.15	44.56	-	84.69

Table 27. Modal frequencies identified by PP, FDD and SSI (i = 400, n = 60) methods from experimental specimens under swept sine excitation (0~400 Hz).

0%-Delaminated	PP (HZ)	15.53	20.41	31.31	68.22	84.32	165.73
	FDD (HZ)	15.51	20.51	31.02	68.78	82.54	165.83
	SSI (HZ)	15.45	20.35	31.20	-	82.52	165.76
22.2%-Delaminated	PP (HZ)	14.66	-	26.78	50.69	-	-
	FDD (HZ)	14.51	-	26.51	50.52	-	-
	SSI (HZ)	14.52	-	27.03	50.40	-	-
51.9%-Delaminated	PP (HZ)	13.81	-	27.00	-	-	-
	FDD (HZ)	13.76	-	26.76	-	-	-
	SSI (HZ)	14.05	-	27.44	-	-	-
74.1%-Delaminated	PP (HZ)	8.97	-	24.06	43.94	-	85.35
	FDD (HZ)	9.00	-	24.01	44.02	-	84.54
	SSI (HZ)	8.98	-	24.40	44.56	-	84.37

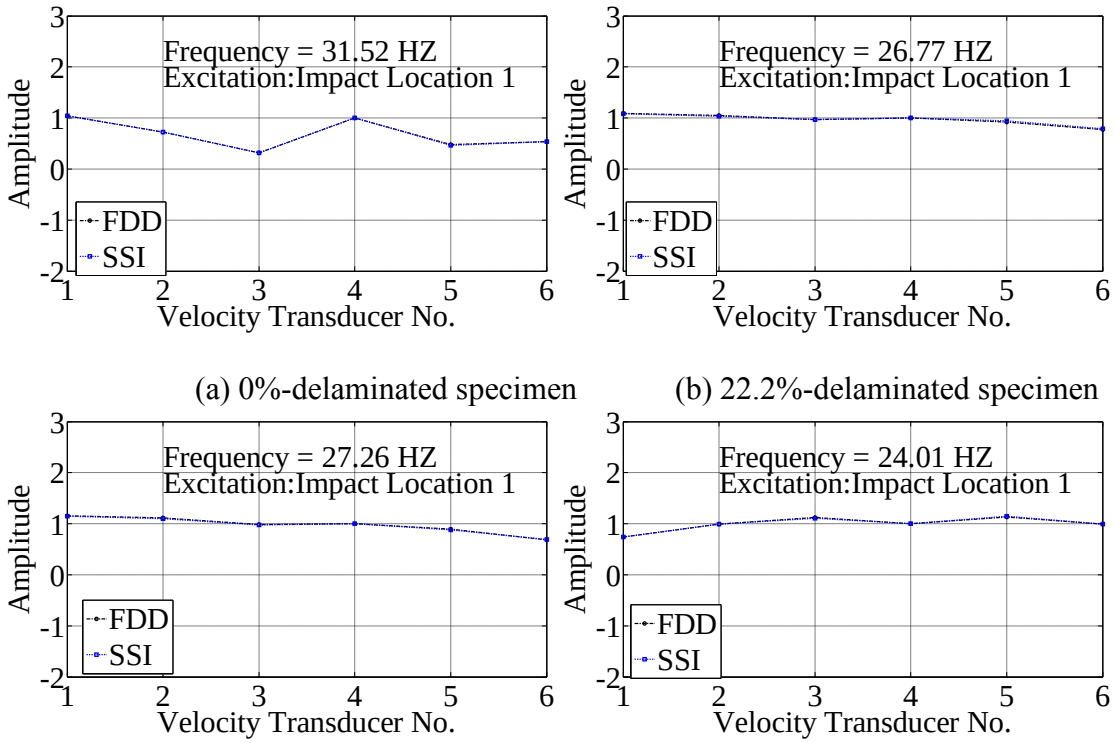

(a) 0%-delaminated specimen (b) 22.2%-delaminated specimen

(c) 51.9%-delaminated specimen (b) 74.1%-delaminated specimen

Figure 70. Comparison of mode shapes by FDD and SSI identification methods from the response measurements due to impact excitation.

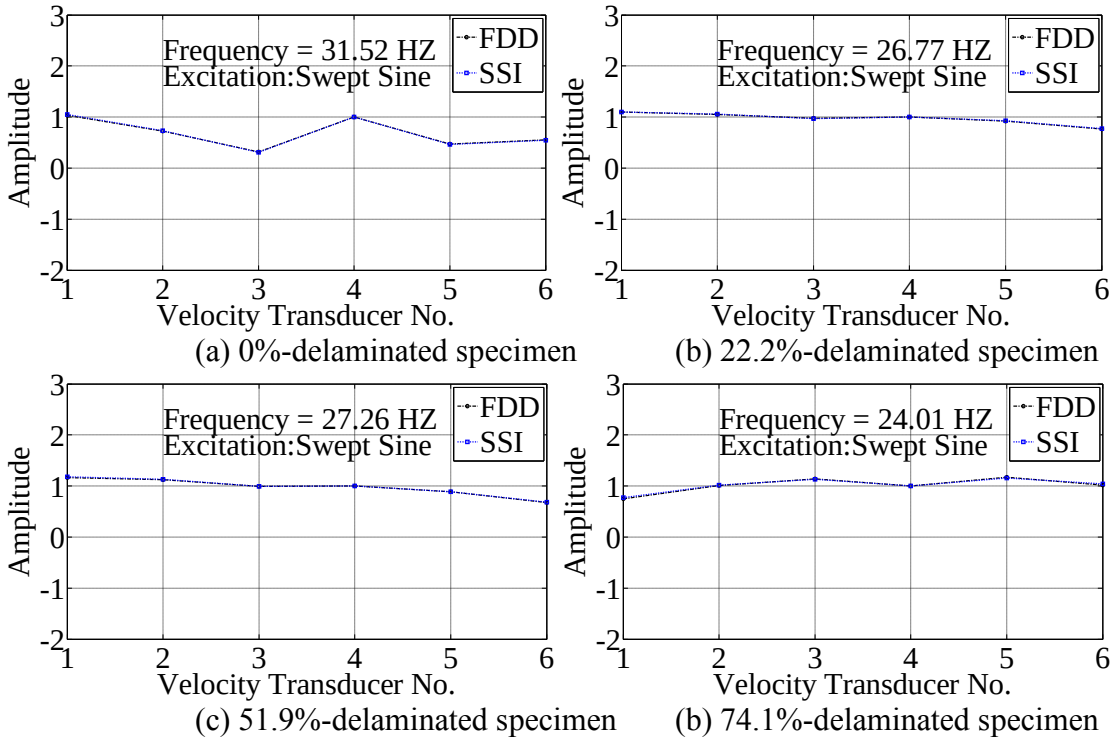

Figure 71. Comparison of mode shapes by FDD and SSI identification methods from the response measurements due to swept sine excitation.

CURRICULUM VITAE

Shutao Xing

Summary

Experience in structural engineering and extensive knowledge of civil engineering. Solid background in structural analysis, numerical modeling, finite element analysis, and in-depth knowledge of solid mechanics and mathematics. Research experience in structural dynamics and earthquake engineering, damage detection of structures, and structural health monitoring. Solid knowledge base in concrete and steel structures, bridge design, structural safety evaluation, vibration control, and seismic design and retrofit. Highly self-motivated and ability to work independently as well as part of a team.

Specialties

Structural analysis and design; Vibration control, damage detection and structural health monitoring; Structural dynamics and earthquake engineering; Seismic design and retrofit.

Experience

- Engineering Intern, Parsons, May ~ August, 2008
- Research Assistant, Utah State University, 2006-2011
- Research Assistant, UC Irvine, 2005
- Research assistant and engineer, Institute of Engineering Mechanics, China Earthquake Administration, 2000-2004

Education

- PhD in Civil Engineering, Utah State University, Logan, Utah, USA, 2011
- MS in Civil Engineering, University of California, Irvine, Irvine, California, USA, 2006
- BS in Civil Engineering, Southwest Jiaotong University, Chengdu, China, 2000

Certificate

- EIT

Skills

- Mathematics and Data Analysis: MATHEMATICA, ORIGIN, MathCAD
- Programming: MATLAB, FORTRAN
- 3D Modeling: Auto CAD, MicroStation
- Finite Element: ANSYS, LARSA, DESCUS, SAP2000, OpenSees, ConSpan, ABAQUS.
- Office Applications and Database: Microsoft Office Suite, Adobe Acrobat, EndNote, MySQL database.
- Instrumentation and Tests: Kinematrics and DataPhysics Data Loggers, Lantronix Device Servers, Sensors, Survey Instruments, Material Test Machines, Dynamic tests, GPS.

Selected Projects

- Modeling and Identification of Structural Pounding, 2011-
- Delamination Detection of Reinforced Concrete Decks, 2009~2010

- Bridge Health Monitoring of C846 (I15/SR201, Utah), 2006-2009
- Study on Resisting Unequal Settlement of Buildings by Base-Isolation Approach, 2004
- Damage Assessment and Retrofit of Many Buildings in Fushun City, China, 2003-2004
- Locating True South-North Direction for the Instrument Service Center of Daqing City, China, 2003
- Passive Vibration Control of Structures using a New Type of Mild Steel Damper, 2001-2003

Publications

- Xing, S., Halling, M.W., Barr, P.J, “Delamination detection in reinforced concrete decks using modal identification", submitted to ASCE journal, under revision.
- Shutao Xing, et al, "Structural pounding identification by using wavelet Scalogram", In Proc. of the 8th International Conference on Structural Dynamics EURODYN 2011, Leuven, Belgium, 4 to 6 June 2011.
- XING, S., GUO X., (2003). "Study on mechanical behavior and effectiveness of a new type of mild steel damper", Earthquake Engineering and Engineering Vibration, 23(6). (in Chinese, Cited by 36)
- Xing, S., Halling, M.J., Barr, P.W.: Delamination detection in concrete plates using output-only vibration measurements. In: Proc. of IMAC 29, the International Modal Analysis Conference, Jacksonville, Florida, 2011
- Xing, S., Halling, M.W., Barr, P.J.: Delamination detection and location in concrete deck by modal identification. In: Proc. of Structures Congress 2010, Orlando, FL, USA, May 2010, pp. 741-751
- Xing, S., Halling, M.W., Barr, P.J., Meng, Q.: Ambient vibration analysis of a highway bridge with N4SID and frequency domain decomposition method. In: Proc. of 14th world conference on Earthquake Engineering, Beijing, China 2008
- Xing, S., Halling, M.W., Barr, P.J., Damage identification of substructures by using adaptive filter and wavelet transform, Poster presentation, Structural Congress 2011, Las Vegas, Nevada
- Halling, M.W., Xing, S., Barr, P.J.: Structural monitoring for bridge behavior and damage detection. in: 6th National Seismic Conference on Bridges and Highways, Charleston, SC, July 27-30 2008
- Porter, SD, Julander, JL, Halling, MW; Barr, PJ, Boyle, H, Xing, S, (2010), "Flexural testing of precast bridge deck panel connections", ASCE Journal of Bridge Engineering.

Awards

- Graduate Travel Awards, Utah State University, 10/2008, 05/2010, 01/2011.
- Graduate Fellowship, UC Irvine, June-September, 2005
- Academic Excellence Scholarships, Southwest Jiaotong University, 1997, 1998, 1999

Affiliations and Service

- M.ASCE (Member of ASCE) Since 2010
- Student member of AISC Since 2010
- Member of SEM (Society of Experimental Mechanics), Since 2011
- Member of European Association for Structural Dynamics, 2011
- Member of Organizing Committee, International Conference on Advances and New Challenges in Earthquake Engineering Research, 2002
- Reviewer for the 10th International Conference on Recent Advances in Structural Dynamics, UK, 2010
- Session Moderator, 2010 Intermountain Graduate Research Symposium, March 2010